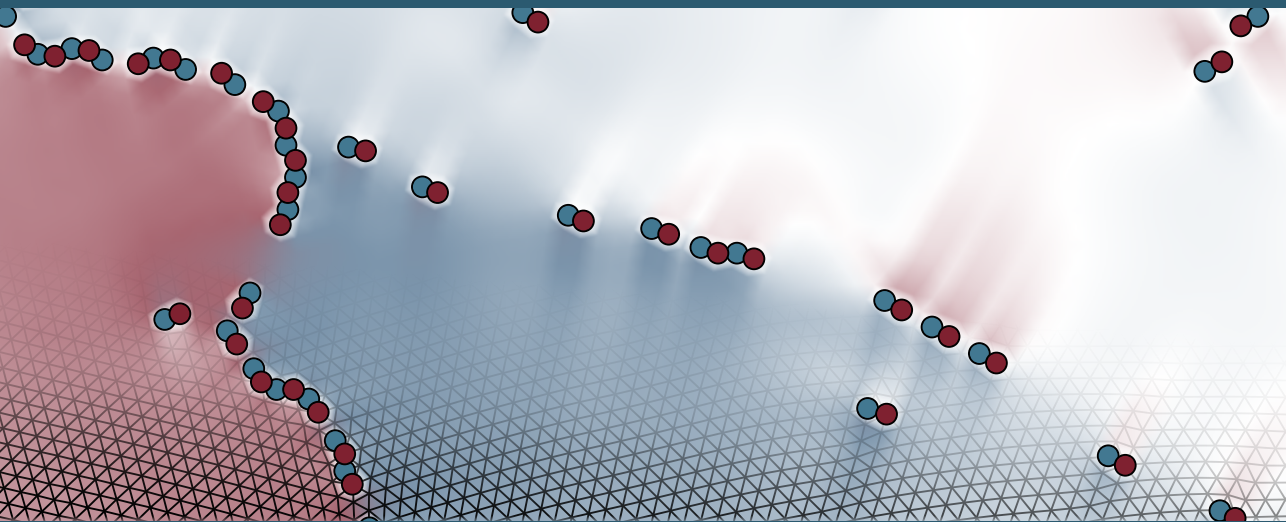


Chiral Magnets in and out of Equilibrium



Dissertation
Lukas Heinen

CHIRAL MAGNETS IN AND OUT OF EQUILIBRIUM

Inaugural-Dissertation
zur
Erlangung des Doktorgrades
der Mathematisch-Naturwissenschaftlichen Fakultät
der Universität zu Köln
vorgelegt von
Lukas Georg Johannes Heinen
aus Frechen

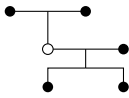


Köln 2021

Berichterstatter:
(Gutachter)

Prof. Dr. Achim Rosch
Prof. Dr. Simon Trebst

Tag der mündlichen Prüfung: 21.10.2020



CONTENTS

LIST OF FIGURES	VII
SYMBOLS	IX
ABSTRACT	XI
KURZZUSAMMENFASSUNG	XII
1 CHIRAL MAGNETS AND SKYRMIONS	1
1.1 General Introduction	1
1.2 Models of Chiral Magnets	5
1.3 Dipolar Interaction	9
2 CUBIC ANISOTROPY AND THE PHASE DIAGRAM	15
2.1 Magnetic Anisotropy	15
2.2 Mapping the Phase Diagram	17
2.3 Signatures of the New Phases	32
3 DEFECTS IN SKYRMION LATTICES	39
3.1 Lattice Defects	39
3.2 Rotating a Skyrmion Lattice	41
3.3 Melting a Skyrmion Lattice	48
4 DRIVING THE CONICAL STATE BEYOND THE LINEAR REGIME	53
4.1 Linear Response	53
4.2 Beyond Linear Response	55
CONCLUSION	61
BIBLIOGRAPHY	63
INDEX	71
DANKSAGUNG	72
ERKLÄRUNG	73

LIST OF FIGURES

1.1	Crystal structures of MnSi and Cu ₂ OSeO ₃	2
1.2	Typical magnetic phase diagram of a chiral magnet and schematic views of the phases of interest	3
1.3	Precession of spins with and without damping	6
1.4	Illustration of a phase transition from the Ginzburg–Landau model	9
1.5	Macrogeometry approach to PBCs	11
2.1	Energy surfaces for cubic crystal anisotropy	16
2.2	Magnetic phase diagram of Cu ₂ OSeO ₃ for different magnetic field directions .	17
2.3	Reciprocal lattices of the four modulated states considered	20
2.4	Parameter paths used to generate phase diagrams	21
2.5	Magnetic phase diagrams as a function of magnetic field and anisotropy parameters and exemplary energy functions	23
2.6	Phase diagram of Cu ₂ OSeO ₃ showing the new skyrmion lattice and tilted conical phases with additional data on the new skyrmion lattice	26
2.7	Phase diagram as a function of r_0 and B_z	27
2.8	Phase diagram as a function of K_1 and B_z with and without dipolar interaction	29
2.9	Phase diagram as a function of sample shape and magnetic field	30
2.10	Optimal conical direction as a function of anisotropy and magnetic field . . .	33
2.11	Real-space structure of exemplary conical states with $\mathbf{q} \parallel \mathbf{B}$	34
2.12	Energy surfaces for conical states with different anisotropy and magnetic field	35
2.13	Anisotropy energy surface for the direction of the magnetization with the magnetization of three conical states	36
2.14	Energy density as a function of the cutoff parameter n	37
3.1	Construction of a 5-disclination-defect	39
3.2	Construction of a 7-disclination-defect	40
3.3	A 5-7-dislocation-defect and its Burgers vector	40
3.4	Magnon–skyrmion skew scattering	42
3.5	Skyrmion lattice rotated by an incoming electron beam	42
3.6	Skyrmion-skyrmion interaction potential in 2D	43
3.7	Energy density of a skyrmion lattice in 2D as a function of the lattice constant	43
3.8	Lattice deformation and breaking as a function of heat current	44
3.9	Snapshot of a particle simulation of a skyrmion lattice subject to a temperature gradient	45
3.10	Time series showing three of the processes governing the dynamics of the rotating skyrmion lattice	46
3.11	Skyrmion lattice domain wall in simulation and experiment	47
3.12	Effective skyrmion–skyrmion potential for different magnetic fields	51
4.1	Spin wave excitation modes of the conical state at $\mathbf{k} = 0$	54
4.2	Conical spectrum from micromagnetic simulations	56
4.3	Non-linear spin waves in the conical state	57
4.4	Driving frequency dependence of the screw frequency ω_{screw}	58
4.5	Azimuthal angle difference showing the population of a second spin wave mode	59

SYMBOLS

\mathbf{a}	a vector
$\hat{\mathbf{a}}$	a unit vector
$\hat{\mathbf{e}}_d$	unit vector in d -direction
\mathbf{r}	spacial coordinate
\mathbf{r}_{ij}	relative coordinate: $\mathbf{r}_{ij} := \mathbf{r}_j - \mathbf{r}_i$
\mathbf{k}	wavevector
a_d	lattice spacing in d -direction
V_{dc}	(volume of) a discretization cell
L_{dc}	lattice of discretization cells
V_{uc}	(volume of) a unit cell
L_{uc}	lattice of unit cells
L_{uc}^*	reciprocal lattice of L_{uc}
\mathbf{M}	magnetization
\mathbf{m}	magnetic moment
\mathbf{B}	magnetic flux density ¹
\mathbf{H}	magnetic field
μ_0	vacuum permeability
J	exchange interaction strength
D	Dzyaloshinskii–Moriya interaction strength
α	LLG damping parameter
γ	gyromagnetic ratio
N_V	demagnetization tensor
$N(\mathbf{r}_{ij})$	demagnetization tensor field/demagnetization kernel
N_i	demagnetization factor
W	topological charge
ρ	topological charge density
χ	helicity
$\mathbb{1}_n$	identity matrix in n dimensions
ϵ_{ijk}	Levi-Civita symbol

¹We will also use “magnetic field” for \mathbf{B} as well as \mathbf{H} .

ABSTRACT

In ordinary ferromagnets, individual magnetic moments tend to align with their neighbors, as long as temperatures are below the critical Curie temperature of the material. Cubic chiral magnets are a class of dominantly ferromagnetic, or rarer ferrimagnetic, materials with a literal twist. Due to broken inversion symmetry, weak spin–orbit coupling can induce a competing Dzyaloshinskii–Moriya interaction, which twists the magnetic texture into helical structures. One of these textures is of special interest to us. In it, the magnetization twist into whirl-like topological structures, called skyrmions.

In this thesis, we will explore various aspects of the equilibrium and non-equilibrium properties of chiral magnets. The first chapter will give an introduction to the subject, focusing on both the phenomenology of chiral magnets and the models we use to describe them. Special attention will be given to the description and effects of dipolar interaction.

In the second chapter, we will explore the effects of cubic magnetocrystalline anisotropy on chiral magnets. In particular, we will examine their effect on the magnetic phase diagram, and compare the results to recent experiments performed by our collaborators on Cu_2OSeO_3 . We will find two new helimagnetic phases, a tilted conical phase with an unexpected propagation vector \mathbf{q} , and a second skyrmion lattice phase.

The third chapter will describe two studies that, as it turns out, both involve defects in skyrmion lattices. In the first of these, we will explore the mechanism with which skyrmion lattices rotate when driven by a radial heat current. This mechanism is based on continuous plastic deformations of the skyrmion lattice. For the second project, we will set out to develop a theoretical description of the two-step melting process of a skyrmion lattice, as observed in experiments performed by our collaborators.

In the final chapter, we will discuss excitations of the conical phase of chiral magnets. The existing theoretical description, based on linear response theory, successfully describes many experiments in various chiral magnets. We will explore the effects of excitations beyond the regime of validity of linear response theory. We will find that the existing description is incomplete. The two homogeneous conical excitation modes both feature an Archimedean screw-like rotation of the magnetic structure, on top of the previously known spin compression waves.

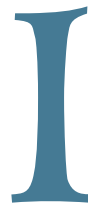
In gewöhnlichen Ferromagneten tendieren die einzelnen magnetischen Momente dazu sich parallel aneinander auszurichten, solange die Temperatur unterhalb der kritischen Curie-Temperatur liegt. Chirale Magnete sind Materialien die lokal ferromagnetisch, oder seltener auch ferrimagnetisch, geordnet sind, sich auf größeren Distanzen jedoch anders verhalten. Da ihre Kristallstruktur keine Inversionssymmetrie besitzt, kann die schwache Spin–Bahn-Kopplung eine sogenannte Dzyaloshinskii–Moriya Wechselwirkung erzeugen, die die Magnetische Textur zu helikalen Strukturen verdrillt. Eine dieser Texturen ist dabei von besonderem Interesse für uns. Sie besteht aus wirbelartigen topologischen Strukturen der Magnetisierung, die Skymionen genannt werden.

In der vorliegenden Dissertation werden wir verschiedene Gleichgewichts- und Nichtgleichgewichts-Eigenschaften von chiralen Magneten untersuchen. Das erste Kapitel gibt eine Einführung zur Phänomenologie chiraler Magnete, sowie zu den Modellen, die wir verwenden um sie zu beschreiben. Dabei werden wir insbesondere noch einmal auf die dipolare Wechselwirkung eingehen.

Im zweiten Kapitel werden wir den Einfluss kubischer magnetischer Kristallanisotropie auf chirale Magnete untersuchen. Insbesondere werden wir die Auswirkungen auf das magnetische Phasendiagramm betrachten, und die Ergebnisse mit an Cu_2OSeO_3 durchgeführten Experimenten vergleichen. Dabei werden zwei neue helimagnetische Phasen auftauchen. Eine gekippte konische Phase deren Wellenvektor \mathbf{q} eine unerwartete Ausrichtung aufweist, sowie eine zweite Skymion-Gitter Phase.

Im dritten Kapitel werden wir zwei Studien behandeln, in denen, wie sich herausstellt, in beiden Fällen Defekte im Skymion-Gitter eine zentrale Rolle spielen. Für die erste der beiden Studien werden wir den Mechanismus untersuchen, durch den Skymion-Gitter rotieren, die einem radialen Wärmestrom ausgesetzt werden. Der Mechanismus basiert auf der kontinuierlichen plastischen Deformation des Skymion-Gitters. Für die zweite Studie werden wir versuchen eine Theorie für den zweistufigen Schmelzprozess von Skymion-Gittern zu entwickeln, der in Experimenten an Cu_2OSeO_3 beobachtet wurde.

Im letzten Kapitel werden wir Anregungen der konischen Phase chiraler Magnete diskutieren. Die bisher existierende Theorie beschreibt, basierend auf der Theorie der linearen Antwort, erfolgreich verschiedene Experimente an diversen chiralen Magneten. Wir werden den Effekt von Anregungen jenseits der Grenzen der Validität der Theorie der linearen Antwort untersuchen. Unsere Ergebnisse werden zeigen, dass die bisherige Theorie unvollständig ist. Die zwei homogenen Anregungsmoden der konischen Phase weisen, jenseits der bekannten Spin-Kompressionswellen, beide eine kontinuierliche Rotation um \mathbf{q} auf, vergleichbar mit einer Archimedischen Schraube.



— CHIRAL MAGNETS AND SKYRMIONS —

This chapter serves to introduce the reader to the study of chiral magnets in general, and magnetic skyrmions in particular. We will start with a general introduction to the subject, focusing on phenomenology and context. In the second section we will discuss the major models used to describe chiral magnets, before focusing on the treatment of dipolar interaction in the last section of the chapter.

1.1 GENERAL INTRODUCTION

Electrons are fermions. The electronic wavefunction in a magnetic material therefore has to be antisymmetric under electron exchange. This leads to an effective interaction between the spins of neighboring electrons. The symmetry of the crystal lattice determines the symmetry of this interaction. In many magnetic materials the high symmetry of the crystal lattice ensures that any contributions depending on anything other than the scalar product of the spins involved cancel with their symmetry-related counterparts. The resulting effective interaction is called *Heisenberg exchange interaction* and promotes either ferromagnetic or antiferromagnetic behavior. In contrast to that, crystal lattices with lower symmetry can exhibit much more complicated resulting interactions. In particular, in lattices with broken inversion symmetry, some contributions no longer cancel each other, and the resulting interaction will generally also break inversion symmetry. One of these contributions is called *Dzyaloshinskii–Moriya interaction (DMI)* [1–3]. It is induced by weak spin–orbit interaction, and plays a crucial role in this thesis.

Cubic chiral magnets are magnetic materials in the cubic crystal system whose crystal structure does break inversion symmetry. They usually have the $P2_13$ space group, and most have a B20 crystal structure, as depicted in [figure 1.1a](#). Correspondingly, their point-group is the chiral tetrahedral group T . The most notable exception is Cu_2OSeO_3 , which also has the $P2_13$ space group, but has a different crystal structure, as illustrated in [figure 1.1b](#). The resulting DMI competes with a usually dominant ferromagnetic exchange interaction. Since this exchange interaction favors parallel alignment of spins, and DMI favors neighboring spins to be perpendicular to each other, the combination of both prefers neighboring spins to be at a

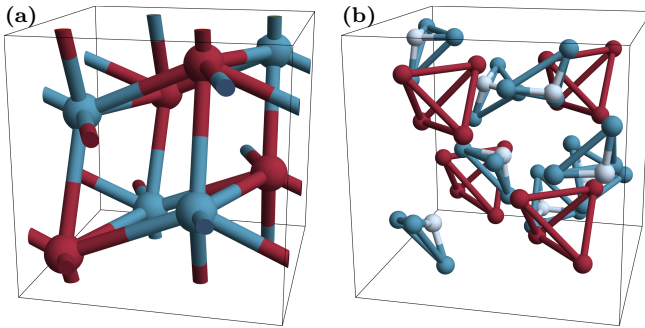


Figure 1.1: Crystal structures of (a) MnSi and (b) Cu_2OSeO_3 . Spheres mark the positions of (a) \bullet Mn, \bullet Si, (b) \bullet Cu, \bullet Se and \bullet O atoms. Atomic positions are taken from (a) Nakanishi et al. [3] and (b) Effenberger et al. [4].

slight angle. Optimal spin configurations therefore feature a twisted, or *helical*, structure of the magnetic texture. Again, Cu_2OSeO_3 is slightly different in that it is dominantly ferrimagnetic. Note that while chiral magnets fall under the category of helimagnets, not all materials with helimagnetic phases have a lattice breaking inversion symmetry. Helimagnetism can also be a result of magnetic frustration [5], which we will not be considering here.

Most chiral magnets show a magnetic phase diagram very similar to the one depicted in figure 1.2a. At high temperatures the system is *paramagnetic*. Upon cooling in strong magnetic fields, the system undergoes a crossover to a *ferromagnetically* ordered phase. When cooling instead without a magnetic field, the system first enters a *fluctuation disordered* regime, before ordering into the *helical* phase. Figure 1.2c shows a uniform helical state, characterized by a propagation vector \mathbf{q} . In this state, all spins lie in the plane perpendicular to \mathbf{q} , and the magnetization is constant in the corresponding real-space directions. In the direction parallel to \mathbf{q} , the spins continuously rotate around \mathbf{q} . Measurements, however, often find the system in a state with multiple domains, characterized by different propagation vectors \mathbf{q} . The directions of these are determined by the easy axes of weak magnetocrystalline anisotropy.¹ The domains are separated by complicated domain walls [6]. Upon application of a critical external magnetic field \mathbf{H}_{c1} , the system undergoes a phase transition into the *conical* phase. This phase is described by a single- \mathbf{q} structure very similar to the helical state. Here, however, the spins are not perpendicular to \mathbf{q} , but rather tilted towards \mathbf{q} , such that together they form the mantle of a cone aligned with \mathbf{q} , as shown in figure 1.2d. Also, the direction of the \mathbf{q} vector is no longer determined by anisotropy. Instead, it aligns with the magnetic field. Finally, in a small range of temperatures and fields, just below the magnetic ordering temperature, a phase historically called “A-phase” can be found. In their seminal work from 2009 Mühlbauer et al. reported discovering this phase to host a triangular *lattice of skyrmions* [7]. This sparked a large number of publications on chiral magnets and magnetic skyrmions. Later, other materials and magnetic systems were discovered to host skyrmions as well. This includes, among others, βMn -type compounds [8], lacunal spinels [9, 10] and, maybe most importantly for potential applications, magnetic thin films and multi-layers [11, 12]. For an overview see for example [13].

Skyrmions are named for Tony H. R. Skyrme, who proposed to describe nucleons as topologically nontrivial quasi-particle excitation of pion fields in a nonlinear field theory [14]. Since then the concept was generalized and used to describe a wide array of physics, including particle physics, liquid crystals, quantum hall states, and now chiral magnets — see for example Schütte’s thesis for an overview [15].

² ¹A more detailed description will follow in chapter 2.

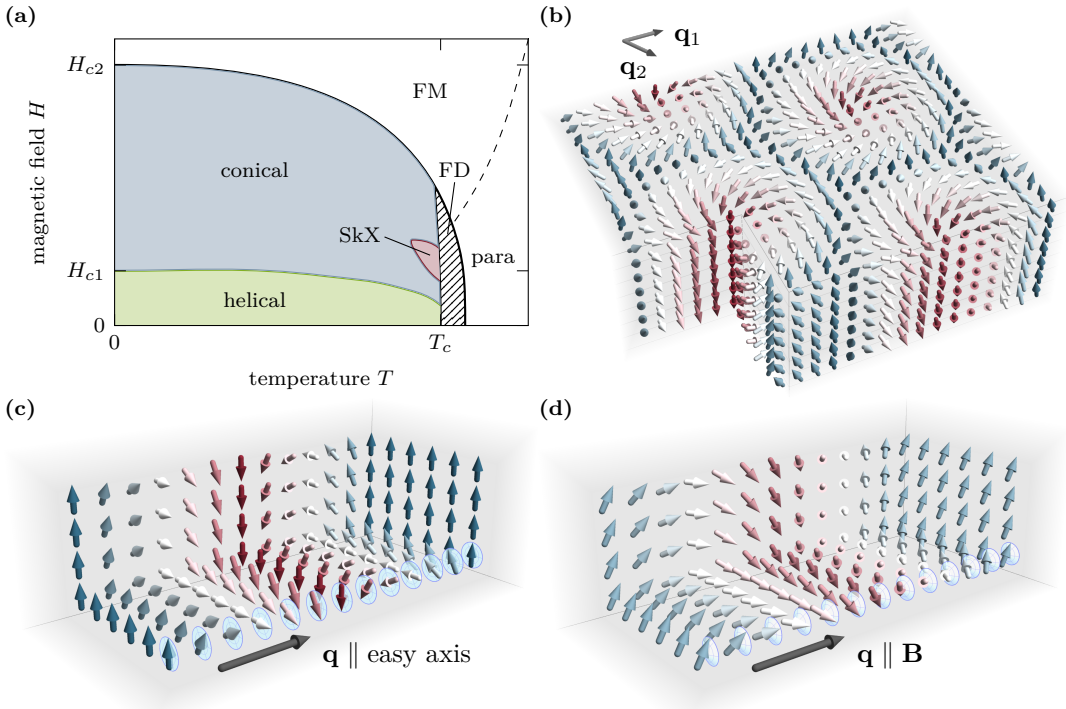


Figure 1.2: (a) Typical magnetic phase diagram of a chiral magnet and (b–c) schematic views of the phases of interest. (b) The skyrmion lattice phase (SkX) consists of a triangular lattice of skyrmions. The symmetry axis is aligned with the magnetic field. (c) The helical phase typically exhibits multiple domains like the one shown here, each oriented along an easy axis. (d) The conical phase is similar to a single helical domain, but the spins are tilted in \mathbf{q} -direction, which aligns with \mathbf{B} . Not illustrated are the paramagnetic (para) and field-polarized (FM) phases and the fluctuation disordered regime (FD). For the newly discovered further phases of Cu_2OSeO_3 , we refer to [chapter 2](#).

We will study magnetic skyrmions as they appear in chiral magnets. There, the term is used to describe whirl-like configurations of the magnetic texture, as illustrated in [figure 1.2b](#). They can appear in a typically triangular lattice, as depicted, or isolated in a polarized background. While the latter is more interesting for applications, the former constitutes the mean-field description of the skyrmion lattice phase.

For a mathematical description of chiral magnets, we can use a continuous function $\mathbf{M} : \mathbb{R}^3 \rightarrow \mathbb{R}^3$ to describe the coarse grained magnetization. At low temperatures, fluctuations of the magnitude $|\mathbf{M}|$ are small, and the normalized magnetization $\hat{\mathbf{M}} : \mathbb{R}^3 \rightarrow S^2$ contains the essential information. Looking, for a moment, at the special case when the magnetization is constant along a certain direction, call it z , and also constant at infinity (or equivalently confined to a finite area A and constant along its boundary), we can map the relevant parameter space as $\mathbb{R}^3 \mapsto \mathbb{R}^2 \mapsto S^2$. We then arrive at a description $\hat{\mathbf{M}} : S^2 \rightarrow S^2$. As the homotopy group of such functions is isomorphic to the integer numbers: $\pi_2(S^2) \cong \mathbb{Z}$, they

can be characterized by an integer. This number, often called topological charge or *winding number*, can be calculated as

$$W[\hat{\mathbf{M}}] = \frac{1}{4\pi} \iint_A \hat{\mathbf{M}} \cdot (\partial_x \hat{\mathbf{M}} \times \partial_y \hat{\mathbf{M}}) dx dy \in \mathbb{Z}, \quad (1.1)$$

where x and y are defined to be perpendicular to z . The fact that this integral is quantized to an integer under the stated conditions may not be immediately obvious. By realizing, though, that the integrand corresponds to the infinitesimal solid angle spanned by $\hat{\mathbf{M}}$ on an infinitesimal real-space area, it is clear that the integral gives the total solid angle spanned by $\hat{\mathbf{M}}$ over A . Since $\hat{\mathbf{M}}$ is required to be constant on the boundary ∂A , this solid angle must be a multiple of 4π , and hence $W[\hat{\mathbf{M}}] \in \mathbb{Z}$.

Notice that while in two dimensions the winding number can be uniquely defined by fixing the real-space orientation, in three spacial dimensions it is at most defined up to a sign. What can be defined uniquely is the generalization of the topological charge density:

$$\text{2D: } \rho[\hat{\mathbf{M}}] = \frac{1}{4\pi} \hat{\mathbf{M}} \cdot (\partial_x \hat{\mathbf{M}} \times \partial_y \hat{\mathbf{M}}) \quad (1.2)$$

$$\text{3D: } \rho_i[\hat{\mathbf{M}}] = \frac{1}{8\pi} \epsilon_{ijk} \hat{\mathbf{M}} \cdot (\partial_j \hat{\mathbf{M}} \times \partial_k \hat{\mathbf{M}}), \quad (1.3)$$

with $W[\hat{\mathbf{M}}] = \iint \rho[\hat{\mathbf{M}}] dx dy$. In three dimensions, $\rho[\hat{\mathbf{M}}]$ is an axial vector field parallel to the axis along which the configuration is constant, if such an axis exists. For configurations that are not constant along any axis, the situation is more complicated. Of course, we can still choose an axis $\hat{\mathbf{e}}_z$, and integrate ρ over an area $A(z)$ perpendicular to it. If $\hat{\mathbf{M}}$ is still constant along the boundary $\partial A(z)$ of this area for any fixed z and everywhere continuous, the result will still be an integer number. Since

$$W_z[\hat{\mathbf{M}}] = \iint_{A(z)} \hat{\mathbf{e}}_z \cdot \rho[\hat{\mathbf{M}}] dx dy \quad (1.4)$$

is then a continuous map $z \mapsto W_z[\hat{\mathbf{M}}]$ to the integers, it must be a constant function of z , even if $\hat{\mathbf{M}}$ is not. Even on the boundary $\partial A(z)$ $\hat{\mathbf{M}}$ may be a function of z , without changing this fact, although it does depend on the choice of $\hat{\mathbf{e}}_z$. If, however, $\hat{\mathbf{M}}$ is discontinuous along z , while still being continuous within $A(z)$ and constant on $\partial A(z)$ for any fixed z , $W_z[\hat{\mathbf{M}}]$ becomes a function $\mathbb{R} \rightarrow \mathbb{Z}$ of z , that is not necessarily constant. Similarly, for $\hat{\mathbf{M}}$ discontinuous within $A(z)$, or non-constant along its boundary $\partial A(z)$, $W_z[\hat{\mathbf{M}}]$ becomes a function $\mathbb{R} \rightarrow \mathbb{R}$ of z .

A skyrmion, in our convention, is then a localized configuration of the magnetization that fulfills these requirements at least approximately, and has a winding number of $W = -1$ throughout its height. While this still leaves significant room for variety (see e.g. Müller's thesis [16]), the skyrmions that we will treat in this thesis will always be similar to those depicted in [figure 1.2b](#). A particularly noteworthy variation comes from the fact that the winding number is invariant under rotations of all spins around the z -axis. The corresponding degree of freedom is called helicity χ . We start from an axisymmetric skyrmion with the central spins pointing down and rotating directly away from the central axis as we move outward, until they point up at the boundary. A skyrmion with helicity χ can be generated

from this configuration by rotating all spins around the z -axis by an angle χ . Skyrmions with $\chi = \pm \frac{\pi}{2}$ are called *Bloch-type* (figure 1.2b shows skyrmions with $\chi = \frac{\pi}{2}$), and those with $\chi \in \{0, \pi\}$ are known as *Néel-type*. Which type of skyrmion occurs in a system depends on its symmetry. Chiral magnets host Bloch-type skyrmions, where the sign of χ is determined by the sign of the DMI strength D discussed in the next section. This, in turn, is determined by the chirality of the underlying crystal structure, which can be left- or right-handed. Note, though, that sample surfaces have lower symmetry, which is reflected in the configuration of skyrmions at the surface. At surfaces perpendicular to the skyrmion-axis, the magnetization twists, changing the local helicity [LH4, 17, 18]. Néel-type skyrmions are unstable in chiral magnets. In other systems, like magnetic multi-layers and lacunal spinels, however, they can be stable and may form the ground state [9–12]. Note that in some other conventions, the name skyrmion also refers to comparable configurations with other winding numbers—especially $W = 1$, which we would call an anti-skyrmion.

Due to their topological nature, skyrmions are often said to be topologically protected. Indeed, under the assumption of a continuous magnetization with near-constant magnitude, skyrmions can only be destroyed by moving them to the sample surface. In real materials, however, so-called Bloch points may form, at which the magnetization formally becomes discontinuous, and the underlying lattice can no longer be ignored. By introducing such Bloch points, the topological protection of skyrmions is lifted, and skyrmions can be destroyed [19]. However, these processes require a sizable activation energy—the energy needed to create a Bloch point, or even a pair of Bloch points, depending on the details of the process. Therefore, the topological nature of skyrmions is associated with an energy barrier enhancing their stability, see for example [20]. Interestingly though, this energy barrier is not the only major factor determining the lifetime of skyrmions. While it has been shown to follow a typical Arrhenius law with exponential dependence on the barrier and temperature, the associated entropy-related prefactor varies by more than 30 orders of magnitude [21].

Interestingly, skyrmions were initially believed to occur only metastably in chiral magnets, because they usually have higher energy than a conical state. It has been shown, however, that in the small phase pocket of the skyrmion lattice, they have lower *free* energy [7]. Thus, the skyrmion lattice phase is actually stabilized by thermal fluctuations.

Beyond purely academic interest for these topological quasi-particles, skyrmions have also attracted significant interest for their promise for applications. They pose strong candidates for possible so-called spintronic devices, due to their small size, exceptional stability, and how readily they can be manipulated. They can be driven by oscillating magnetic fields [22], thermal gradients [23], and electric currents [24, 25]. A number of possible applications have already been proposed [26–31]. For further reading on chiral magnets, skyrmions and a review of current research on the topic see for example [13, 26, 32–34].

1.2 MODELS OF CHIRAL MAGNETS

Theoretical descriptions of chiral magnets are usually based on one of three closely related models, or their generalizations. Here we will take a short look at all three of them, and how they are related to each other. The first of these, usually called *non-linear sigma model*, describes a coarse-grained magnetization as a continuous vector field \mathbf{M} of constant magnitude. For convenience, units are often chosen so that $|\mathbf{M}| = 1$. In its basic form the model is

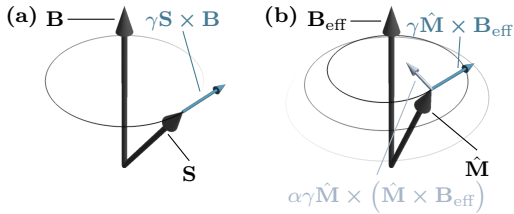


Figure 1.3: (a) Precession of a (classical) spin in a magnetic field according to the Heisenberg equation (1.7). (b) Damped precession of the magnetization according to the LLG equation (1.8). Both are shown for negative γ (electron-like).

governed by the following free energy functional:

$$F_{\text{base},V}[\mathbf{M}] = \int_V f_{\text{base},V}[\mathbf{M}](\mathbf{r}) d^3r \quad (1.5)$$

$$f_{\text{base},V}[\mathbf{M}](\mathbf{r}) = -\frac{J}{2} \hat{\mathbf{M}} \cdot (\Delta \hat{\mathbf{M}}) + D \hat{\mathbf{M}} \cdot (\nabla \times \hat{\mathbf{M}}) - \mathbf{B} \cdot \mathbf{M}. \quad (1.6)$$

With positive Heisenberg exchange coupling constant $J > 0$, the first term favors constant magnetization. Together with the DMI described by the second term a helical configuration is favored, where the sign of the DMI coupling constant D determines the chirality. The third term gives the Zeeman coupling to the applied magnetic field \mathbf{B} . Finally, the model is routinely extended to incorporate further effects, such as dipolar interaction of spins described by $f_{\text{demag},V}[\mathbf{M}](\mathbf{r})$, which we will discuss in the next section. This model is the one most amenable to analytical treatment and will serve as our reference.

Regarding the dynamics of the magnetization, we will first take a look at the Hamiltonian dynamics of a single spin in a magnetic field. Using the simple Hamiltonian $\hat{H} = -\gamma \hat{\mathbf{S}} \cdot \mathbf{B}$ with the gyromagnetic ratio γ , the Heisenberg equation of motion for the spin reads

$$\frac{d\hat{\mathbf{S}}}{dt} = \frac{i}{\hbar} [\hat{H}, \hat{\mathbf{S}}] = \gamma \hat{\mathbf{S}} \times \mathbf{B}, \quad (1.7)$$

the result of which is a precession of the spin around the magnetic field which is illustrated in figure 1.3a by a classical trajectory [35]. This precession of spins also translates to the coarse-grained magnetization \mathbf{M} . To describe its full dynamics, however, we need to take dissipative processes like electron-phonon interaction into account. This is usually done phenomenologically, resulting in the Landau–Lifshitz–Gilbert (LLG) equation:²

$$\frac{\partial \hat{\mathbf{M}}}{\partial t} = \gamma \hat{\mathbf{M}} \times \mathbf{B}_{\text{eff}} - \alpha \frac{\gamma}{|\gamma|} \hat{\mathbf{M}} \times \frac{\partial \hat{\mathbf{M}}}{\partial t}. \quad (1.8)$$

The second term, proportional to the dimensionless damping parameter α , describes the simplest effect of non-spin-conserving dissipative processes. Importantly, the first term no longer contains only the applied field \mathbf{B} , but rather the effective magnetic field

$$\mathbf{B}_{\text{eff}}[\mathbf{M}](\mathbf{r}) = -\frac{\delta F[\mathbf{M}]}{\delta \mathbf{M}(\mathbf{r})} = -\frac{1}{|\mathbf{M}|} \frac{\delta F[\mathbf{M}]}{\delta \hat{\mathbf{M}}(\mathbf{r})} \quad (1.9a)$$

$$= \frac{J}{|\mathbf{M}|} \Delta \hat{\mathbf{M}} - \frac{2D}{|\mathbf{M}|} \nabla \times \hat{\mathbf{M}} + \mathbf{B} + \mathbf{B}_{\text{extensions}}[\mathbf{M}](\mathbf{r}), \quad (1.9b)$$

containing the effects of all interactions considered in the model, where $\mathbf{B}_{\text{extensions}}$ represents all contributions coming from any extensions of F beyond $F_{\text{base},V}$. An exemplary solution

²Note that there are different conventions regarding the sign of γ . Equation (1.8) gives properly damped results for any sign of γ , and a counter-clockwise precession for $\gamma < 0$.

of the LLG equation for constant \mathbf{B}_{eff} is shown in figure 1.3b. Note that sometimes the effective field $\mathbf{H}_{\text{eff}} = \frac{1}{\mu_0} \mathbf{B}_{\text{eff}}$ is inserted instead of \mathbf{B}_{eff} . Correspondingly, there is an alternative definition of γ , compensating for the relative factor.

The LLG equation was introduced by Gilbert [36, 37] as a refinement of the Landau-Lifshitz equation [38], which reads

$$\frac{\partial \hat{\mathbf{M}}}{\partial t} = \gamma' \hat{\mathbf{M}} \times \mathbf{B}_{\text{eff}} - \lambda \hat{\mathbf{M}} \times (\hat{\mathbf{M}} \times \mathbf{B}_{\text{eff}}). \quad (1.10)$$

It is equivalent to the LLG equation via the reparametrization $\gamma' = \gamma / (1 + \alpha^2)$, $\lambda = |\gamma| \alpha / (1 + \alpha^2)$. Since the latter is effectively the result of solving the LLG equation for $\frac{\partial}{\partial t} \hat{\mathbf{M}}$, it is in most cases more convenient to use than the LLG equation, and we will in the following not distinguish between the two.

Note that $\mathbf{B}_{\text{eff}} = 0$ is not required for local minima of the free energy, due to the constant magnitude constraint on the magnetization. Instead, such configurations fulfill $\mathbf{M}(\mathbf{r}) \parallel \mathbf{B}_{\text{eff}}(\mathbf{r})$ and $\mathbf{M}(\mathbf{r}) \cdot \mathbf{B}_{\text{eff}}(\mathbf{r}) > 0$, which is just the requirement for attractive fixed points of the LLG equation (1.8), as long as the external field is independent of time.

For numerical calculations we need some kind of discretization. When choosing to discretize on an orthorhombic lattice in real space, we arrive at a *Heisenberg-type model* describing discrete classical magnetic moments $\mathbf{m}_i = \int_{V_{\text{dc}}} \mathbf{M}(\mathbf{r}_i + \mathbf{r}) d^3r$ on a lattice $L_{\text{dc}} \ni \mathbf{r}_i$ defined by $V = L_{\text{dc}} + V_{\text{dc}} = \{\mathbf{r}_1 + \mathbf{r}_2 | \mathbf{r}_1 \in L_{\text{dc}}, \mathbf{r}_2 \in V_{\text{dc}}\}$, where $V_{\text{dc}} = a_x a_y a_z$ is the volume of a single cuboid discretization cell³ with edges a_d . The free energy reads

$$F_{\text{base}, L_{\text{dc}}}[\mathbf{m}] = V_{\text{dc}} \sum_{\substack{i, j \in L_{\text{dc}} \\ \langle i, j \rangle}} \left(-\frac{J}{2|\mathbf{r}_{ij}|^2} \hat{\mathbf{m}}_i \cdot (\hat{\mathbf{m}}_j - \hat{\mathbf{m}}_i) + \frac{D}{|\mathbf{r}_{ij}|} \hat{\mathbf{m}}_i \cdot (\hat{\mathbf{r}}_{ij} \times \hat{\mathbf{m}}_j) \right) - \sum_{i \in L_{\text{dc}}} \mathbf{B} \cdot \mathbf{m}_i, \quad (1.11)$$

where the indices i and j separately run over all sites $\mathbf{r}_i \in L_{\text{dc}}$ such that they are nearest neighbors, and $\mathbf{r}_{ij} := \mathbf{r}_j - \mathbf{r}_i$ connects the two coordinates and has length $|\mathbf{r}_{ij}| \in \{a_x, a_y, a_z\}$, depending on direction. We assume all \mathbf{m}_i to have equal magnitude $|\mathbf{m}| = V_{\text{dc}} |\mathbf{M}|$, which is a good approximation in the limit $a_d \rightarrow 0$. Note that the Heisenberg exchange term can equivalently be written as $\hat{\mathbf{m}}_i \cdot \hat{\mathbf{m}}_j$, like in the original Heisenberg model. Mathematically, these two ways to write the interaction only differ by an inconsequential constant, but the $\hat{\mathbf{m}}_i \cdot \hat{\mathbf{m}}_j$ term usually has inferior numerical accuracy due to rounding errors.⁴ This is why implementations tend to use $\hat{\mathbf{m}}_i \cdot (\hat{\mathbf{m}}_j - \hat{\mathbf{m}}_i)$ [39, 40].

There are, of course, other options for discretizing the non-linear sigma model, resulting in energy functionals similar to equation (1.11). One option is to increase the range of interactions with prefactors chosen to better approximate the original derivatives, see for example [15, 16]. It is also possible to choose a lattice other than the orthorhombic lattice we chose. The resulting models are, however, mostly relevant not as approximations to the non-linear sigma model, but rather as *atomistic* models, where each magnetic moment represents a single atomic spin instead of the many spins they represent for us. In this vein

³In our notation we will not distinguish between a set $V_{\text{dc}} = \prod_d [-a_d/2, a_d/2] \subset \mathbb{R}^3$ and its volume $V_{\text{dc}} = a_x a_y a_z$.

⁴For a smooth magnetic texture, $\hat{\mathbf{m}}_i \cdot \hat{\mathbf{m}}_j$ is of order one, giving a large overall energy with small relative differences between different configurations. $\hat{\mathbf{m}}_i \cdot (\hat{\mathbf{m}}_j - \hat{\mathbf{m}}_i)$ on the other hand will be much smaller, resulting in much larger relative differences (but mathematically equal absolute differences). This form is therefore more accurate when rounding to the same number of significant digits. A similar, if weaker, statement is also true for the effective field.

some studies also looked at the effects of treating the spins quantum mechanically, instead of classically, with a Hamiltonian similar to [equation \(1.11\)](#) [41, 42].

To describe the dynamics in the Heisenberg model, we discretize the [LLG equation \(1.8\)](#), the result of which looks identical except for the replacement $\hat{\mathbf{M}} \mapsto \hat{\mathbf{m}}$. However, the effective magnetic field is now defined as

$$\mathbf{B}_{\text{eff},i} = -\frac{\partial F[\mathbf{m}]}{\partial \mathbf{m}_i} = -\frac{1}{|\mathbf{m}|} \frac{\partial F[\mathbf{m}]}{\partial \hat{\mathbf{m}}_i} \quad (1.12a)$$

$$= \frac{V_{\text{dc}}}{|\mathbf{m}|} \sum_{\substack{j \in L_{\text{dc}} \\ \langle i,j \rangle}} \left(\frac{J}{|\mathbf{r}_{ij}|^2} (\hat{\mathbf{m}}_j - \hat{\mathbf{m}}_i) - \frac{2D}{|\mathbf{r}_{ij}|} (\hat{\mathbf{r}}_{ij} \times \hat{\mathbf{m}}_j) \right) + \mathbf{B} + \mathbf{B}_{\text{extensions},i}[\mathbf{m}]. \quad (1.12b)$$

While the result, in our case, is identical to discretizing the effective field [\(1.9b\)](#), the same is not always true for more complicated energy functionals. There, it can be critical to use [equation \(1.12a\)](#). The reason behind this discrepancy lies in the fact that some seemingly innocuous operations for the continuous effective field, like applying the product rule to a derivative, do not have a discrete counterpart [LH6].

Using [equation \(1.11\)](#) in conjunction with the [LLG equation \(1.8\)](#) and [equation \(1.12\)](#), we can simulate the magnetization dynamics of chiral magnets [40, 39]. Such simulations are known as micromagnetic simulations. Mathematically they amount to solving the initial value problem of the LLG. Micromagnetic simulations are one of the most important tools used to study chiral magnets.

The last model on our list is the *Ginzburg–Landau model* for the paramagnetic to heli-magnetic phase transition, where the magnitude of the magnetization $|\mathbf{M}(\mathbf{r})|$ will be the order parameter. For this, we lift the restriction of constant magnitude $|\mathbf{M}(\mathbf{r})|$, and add the free energy contributions $r_0 \mathbf{M}(\mathbf{r})^2 + U \mathbf{M}(\mathbf{r})^4$ to [equation \(1.6\)](#). The basic principle of how these contributions describe a phase transition is illustrated in [figure 1.4](#): with positive $r_0 \sim (T - T_c)/T_c$ the Energy is minimal for $|\mathbf{M}| = 0$, while with negative r_0 the ground state is $|\mathbf{M}| = \sqrt{-r_0/2U}$. The details are much more involved, of course, when the full functional is considered.

While the resulting model can be useful without any further modifications, we will only consider a discrete version of it. However, in contrast to before, where we discretized in real space, we will discretize this model in momentum space. This has the advantage that local terms quadratic in $\mathbf{M}(\mathbf{r})$, and even the highly non-local dipolar interaction, become simple. Assuming a periodic magnetic structure with a unit cell V_{uc} , we write $\mathbf{M}_{\mathbf{k}} = \frac{1}{V_{\text{uc}}} \int_{V_{\text{uc}}} \exp(-i \mathbf{k} \cdot \mathbf{r}) \mathbf{M}(\mathbf{r}) d^3r$, and $\mathbf{M}(\mathbf{r}) = \sum_{\mathbf{k} \in L_{\text{uc}}^*} \exp(i \mathbf{k} \cdot \mathbf{r}) \mathbf{M}_{\mathbf{k}}$, and arrive at the mean free energy density functional

$$\begin{aligned} f_{\text{base},V}[\mathbf{M}] = & \sum_{\mathbf{k} \in L_{\text{uc}}^*} \left(\left(\frac{J}{2} \mathbf{k}^2 + r_0 \right) \mathbf{M}_{\mathbf{k}} \cdot \mathbf{M}_{-\mathbf{k}} + i D \mathbf{M}_{-\mathbf{k}} \cdot (\mathbf{k} \times \mathbf{M}_{\mathbf{k}}) \right) \\ & + U \sum_{\substack{\mathbf{k}, \mathbf{k}_2, \mathbf{k}_3, \mathbf{k}_4 \in L_{\text{uc}}^* \\ \mathbf{k} + \mathbf{k}_2 + \mathbf{k}_3 + \mathbf{k}_4 = 0}} \mathbf{M}_{\mathbf{k}} \cdot \mathbf{M}_{\mathbf{k}_2} \mathbf{M}_{\mathbf{k}_3} \cdot \mathbf{M}_{\mathbf{k}_4} - \mathbf{B} \cdot \mathbf{M}_0, \end{aligned} \quad (1.13)$$

where $f_{\cdot,V}[\mathbf{M}]$ is defined by $f_{\cdot,V}[\mathbf{M}] = \frac{1}{V} F_{\cdot,V}[\mathbf{M}] = \frac{1}{V} \int_V f_{\cdot,V}[\mathbf{M}](\mathbf{r}) d^3r$. All sums run over the reciprocal lattice L_{uc}^* , and we assumed the magnetic field to be constant. Note that J and

D are slightly different from those used in the two other models. In those models, the two terms contain the dimensionless normalized magnetic moments or magnetization, respectively. Here, on the other hand, they contain the full magnetization. Consequently, J and D differ by factors of $|\mathbf{M}|$ from their values in the other models.

In contrast to the previous models, we unfortunately do not know the equation of motion for $\mathbf{M}_{\mathbf{k}}$. While the dynamics of the direction $\hat{\mathbf{M}}$ still has to obey the **LLG equation** (1.8), the dynamics of the magnitude $|\mathbf{M}|$ remains, to the best of our knowledge, unexplored. Thus, we will have to resort to one of the previous models, when studying the dynamics of chiral magnets. On the other hand, by considering the energy functional as an action and performing a saddle point approximation, it is possible to factor in further fluctuations, beyond what is already built into the Ginzburg–Landau model [7].

1.3 DIPOLAR INTERACTION

Dipolar interaction, as we discuss it here, stems from the fact that each spin carries a magnetic dipole moment \mathbf{m}_i , which generates a magnetic field. This field, in turn, acts on all other spins, resulting in the total energy

$$F_{\text{dipole}}[\mathbf{m}] = \frac{\mu_0}{8\pi} \sum_{\substack{i,j \\ i \neq j}} \mathbf{m}_i \cdot \frac{\mathbf{1}_3 - 3\hat{\mathbf{r}}_{ij} \otimes \hat{\mathbf{r}}_{ij}}{|\mathbf{r}_{ij}|^3} \cdot \mathbf{m}_j. \quad (1.14)$$

For atomistic models, this expression can immediately be used in place of $F_{\text{demag}}[\mathbf{m}]$. In the non-linear sigma model, however, we need an expression based on the continuous magnetization. The Heisenberg model, on the other hand, which we derived from the non-linear sigma model, should take into account that each discretization cell hosts many spins at different locations within the cell. An obvious way to write a continuous term for the energy would be to simply replace the double sum with two integrals. This limiting process, however, results in a series that does not converge absolutely. The resulting integral would only be semi-convergent and must be avoided. Following Brown [43, Ch. 2, §3], we should instead be careful about the definition of a magnetic dipole. It can be defined as a limit of either two magnetic monopoles or an infinitesimal current loop, and either can be used. Depending on which we choose, we rewrite the energy in terms of the potentials ϕ or \mathbf{A} before taking the limit. Finally, we arrive at one of the following expressions for the energy density in a volume V due to dipolar interaction:

$$f_{\text{demag},V}[\mathbf{M}](\mathbf{r}) = -\frac{\mu_0}{2} \mathbf{M} \cdot \mathbf{H}_{\text{demag}} = -\frac{\mu_0}{2} \mathbf{M} \cdot \left(\frac{1}{\mu_0} \mathbf{B}_{\text{demag}} - \mathbf{M} \right) \quad (1.15a)$$

$$= \frac{\mu_0}{8\pi} \mathbf{M}(\mathbf{r}) \cdot \nabla \int_V \frac{\mathbf{r} - \mathbf{r}'}{|\mathbf{r} - \mathbf{r}'|^3} \cdot \mathbf{M}(\mathbf{r}') d^3r' \quad (1.15b)$$

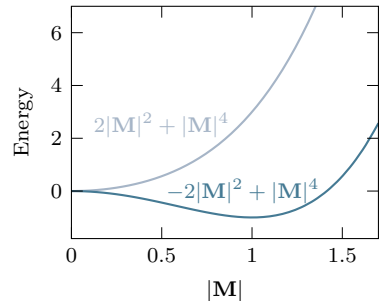


Figure 1.4: Illustration of a phase transition from the Ginzburg–Landau model. For $r_0 \geq 0$ the ground state is $|\mathbf{M}| = 0$, while for $r_0 < 0$ the ground state is $|\mathbf{M}| > 0$.

$$= \frac{\mu_0}{8\pi} \mathbf{M}(\mathbf{r}) \cdot \left(\int_V \frac{\mathbf{r} - \mathbf{r}'}{|\mathbf{r} - \mathbf{r}'|^3} \nabla' \cdot \mathbf{M}(\mathbf{r}') d^3 r' - \int_{\partial V} \frac{\mathbf{r} - \mathbf{r}'}{|\mathbf{r} - \mathbf{r}'|^3} \mathbf{n}(\mathbf{r}') \cdot \mathbf{M}(\mathbf{r}') d^2 r' \right) \quad (1.15c)$$

$$= \frac{\mu_0}{8\pi} \mathbf{M}(\mathbf{r}) \cdot \left(\nabla \times \left(\int_V \frac{\mathbf{r} - \mathbf{r}'}{|\mathbf{r} - \mathbf{r}'|^3} \times \mathbf{M}(\mathbf{r}') d^3 r' \right) \right) + \frac{\mu_0}{2} \mathbf{M}(\mathbf{r})^2 \quad (1.15d)$$

$$= \frac{\mu_0}{8\pi} \mathbf{M}(\mathbf{r}) \cdot \left(\int_V \frac{\mathbf{r} - \mathbf{r}'}{|\mathbf{r} - \mathbf{r}'|^3} \times (\nabla' \times \mathbf{M}(\mathbf{r}')) d^3 r' - \int_{\partial V} \frac{\mathbf{r} - \mathbf{r}'}{|\mathbf{r} - \mathbf{r}'|^3} \times (\mathbf{n}(\mathbf{r}') \times \mathbf{M}(\mathbf{r}')) d^2 r' \right) + \frac{\mu_0}{2} \mathbf{M}(\mathbf{r})^2, \quad (1.15e)$$

where \mathbf{n} is the outward normal vector of the surface ∂V . It is important to note that the derivatives and integrals in equations (1.15b) and (1.15d) may *not* be exchanged, as otherwise the result would again be semi-convergent.

For the Heisenberg model, now, we need to find a discretization scheme for these integrals. This task should not be underestimated, since the resulting integrals can be rather complicated, and it is very easy to make mistakes by accidentally rewriting them into a semi-convergent form. Fortunately, this problem has been studied in quite some detail [44–48]. A common approximation is to assume that \mathbf{M} is constant within each discretization cell. Using this assumption and equation (1.15b), we can write

$$F_{\text{demag}, L_{\text{dc}}}[\mathbf{m}] = \frac{\mu_0}{2} \frac{1}{V_{\text{dc}}} \sum_{i,j} \mathbf{m}_i \cdot N(\mathbf{r}_{ij}) \cdot \mathbf{m}_j \quad (1.16a)$$

$$N(\mathbf{r}_{ij}) = \frac{1}{4\pi V_{\text{dc}}} \int_{V_{\text{dc}}} d^3 r \nabla \otimes \int_{V_{\text{dc}}} d^3 r' \frac{\mathbf{r}_{ij} + \mathbf{r}' - \mathbf{r}}{|\mathbf{r}_{ij} + \mathbf{r}' - \mathbf{r}|^3}. \quad (1.16b)$$

Except for $\mathbf{r}_{ij} = 0$, the remaining integrals in the demagnetization kernel $N(\mathbf{r}_{ij})$, also called demagnetization tensor field, can be expressed as surface integrals using Stokes' theorem. Those can then be evaluated either analytically [44] or numerically [49, 39]. For $\mathbf{r}_{ij} = 0$, on the other hand, $N(\mathbf{r}_{ij})|_{\mathbf{r}_{ij}=0}$ is nothing but the demagnetization tensor of the discretization cell $N_{V_{\text{dc}}}$. For any uniformly magnetized body the magnetostatic energy can be given in terms of its demagnetization tensor:

$$E_{\text{demag}} = \frac{\mu_0}{2} \mathbf{m} \cdot N_V \cdot \mathbf{m} / V. \quad (1.17)$$

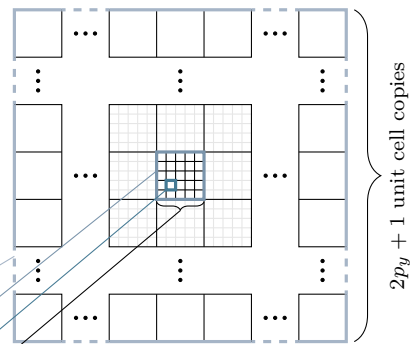
N_V can easily be shown to be a symmetric real matrix, and as such it has a set of eigenvectors forming an orthonormal basis of \mathbb{R}^3 . The corresponding eigenvalues are called demagnetization factors N_i , and can be calculated analytically for some geometries, such as cuboids and ellipsoids [47, 48]. They can also be shown to always add up to one: $\text{tr}(N_V) = N_x + N_y + N_z = 1$. In our case, the demagnetization tensor of the discretization cell is already diagonal, which follows from the fact that the coordinate axes are aligned with the cuboid axes.

Expressing the dipolar interaction in terms of the kernel $N(\mathbf{r}_{ij})$ has further advantages. For example, it lets us consistently express the cases of point dipoles and integrated magnetic moments by setting

$$N_{\text{dipole}}(\mathbf{r}_{ij}) = \begin{cases} 0 & , \mathbf{r}_{ij} = 0 \\ \frac{V_{\text{dc}}}{4\pi} \frac{\mathbf{1}_3 - 3\hat{\mathbf{r}}_{ij} \otimes \hat{\mathbf{r}}_{ij}}{|\mathbf{r}_{ij}|^3} & , \text{else} \end{cases}. \quad (1.18)$$

Figure 1.5: Macrogeometry approach to PBCs. Instead of endlessly repeating copies of the unit cell as for true PBCs, we can place a finite number of copies around our system, effectively describing a much larger, but finite system. Here we place p_d copies of a rectangular unit cell of size $a_{\text{uc},d}$ on each side of the main cell, which in turn consists of n_d discretization cells of size a_d in d -direction.

$$\begin{aligned} \text{total volume } V &= \prod_d (2p_d + 1) n_d a_d = \prod_d (2p_d + 1) a_{\text{uc},d} \\ \text{unit cell volume } V_{\text{uc}} &= \prod_d n_d a_d = \prod_d a_{\text{uc},d} \\ \text{discretization cell volume } V_{\text{dc}} &= \prod_d a_d \\ & n_x \text{ discretization cells} \end{aligned}$$



It is also useful for practical purposes of micromagnetic simulations, since the kernel can be computed in advance, so that during a simulation step only the sum has to be evaluated, which can be done efficiently using fast Fourier transformations. Importantly, the kernel can also be used to include the effects of periodic boundary conditions (PBCs).

For local interactions, PBCs are simple and straightforward. For long-ranged interactions, such as dipolar interaction, on the other hand, they can present a significant problem. Each spin interacts with every other spin, which, for a periodic and thereby infinite system, is an infinite number. Since, however, there are only a finite number of spins per unit cell, we can absorb the sum over unit cells into the kernel, leaving only the same sum over all pairs of spins as for the open system, just with a different kernel. For one- and two-dimensional PBCs the resulting infinite series in the kernel can be calculated numerically, effectively describing rod-like or disk-like samples [50]. For three-dimensional PBCs on the other hand, this series does not converge absolutely. Physically, this is because the energy of a magnetic configuration depends on the shape of the sample in question. It depends on the details of the boundary, no matter how large the sample, no matter how far the boundary is away. Consequently, calculations using three-dimensional PBCs together with dipolar interaction have to specify the shape of the surrounding sample in some way, and are formally, actually, ill defined. One possibility, which we will use in a similar calculation for the Ginzburg–Landau model, is to state the demagnetization tensor directly, since this is the only shape-dependent parameter in the limit of a very large system, which we will show below. Alternatively, we can use a so-called macrogeometry approach, by placing a finite number of copies next to our system [51, 39], instead of the infinitely many copies for PBCs. It is also referred to as quasi PBCs. From now on, we will write true PBCs when referring to the usual definition of PBCs, while PBCs alone may refer to either true PBCs or quasi PBCs/macrogeometry. One implementation of a macrogeometry for rectangular cells is illustrated in figure 1.5.

By choosing a large number of copies, we can then ensure that the influence of the sample boundaries on the central cell is minimized, while retaining the convergence of the kernel sum. Finally, the demagnetization factors can be controlled by changing the number of copies per direction and thereby the aspect ratio of the larger sample. This approach does not model the sample boundaries correctly any more than true PBCs do. Instead, they are assumed to have the same magnetic texture as the central cell deep inside the bulk. However, it does give the correct energy for such a configuration, including effects of the sample shape.

After summation over periodic copies, we can write the demagnetization kernel as

$$N_{\text{PBC}}(\mathbf{r}_{ij}) = \sum_{\mathbf{R} \in L_{\text{uc}}} N(\mathbf{r}_{ij} + \mathbf{R}), \quad (1.19)$$

where $L_{\text{uc}} \subset \mathbb{R}^3$ is the lattice of unit cells, defined by $V = L_{\text{uc}} + V_{\text{uc}}$, for the volume V of the total sample. The unit cell shown in [figure 1.5](#) consists of a rectangular arrangement of n_d cuboid discretization cells in d -direction, with edges a_d . Placing p_d unit cell copies on each side, we can write in this case

$$L_{\text{uc}} = \left\{ \sum_{d \in \{x, y, z\}} m_d n_d a_d \hat{\mathbf{e}}_d \mid m_d \in \{-p_d, \dots, p_d\} \quad \forall d \in \{x, y, z\} \right\}. \quad (1.20)$$

N_{PBC} can then be used instead of N in [equation \(1.16a\)](#) to implement PBCs for dipolar interaction in the Heisenberg model.

Some closely related considerations have to be made when including dipolar interaction in the Ginzburg–Landau model. Here, we will assume the same type of magnetic configuration as described above—periodic magnetization up to the finite boundary. For the continuous magnetization, we can write this as

$$\mathbf{M}'(\mathbf{r}) = \overline{\mathbf{M}}(\mathbf{r}) \chi_V(\mathbf{r}), \quad (1.21)$$

where \mathbf{M}' is the proper magnetization, $\overline{\mathbf{M}}$ is truly periodic with a unit cell V_{uc} , and χ_V is the characteristic function of V , which is 1 inside and 0 outside of V . After a mostly straightforward calculation, using the convention $\chi_V(\mathbf{k}) = \frac{1}{(2\pi)^3} \int \exp(-i\mathbf{k} \cdot \mathbf{r}) \chi_V(\mathbf{r}) d^3r$, we obtain

$$f_{\text{demag}, V}[\mathbf{M}'] = \frac{\mu_0}{2} \sum_{\mathbf{k}_1, \mathbf{k}_2 \in L_{\text{uc}}^*} \mathbf{M}_{\mathbf{k}_1} \cdot N_{V, \mathbf{k}_1, \mathbf{k}_2} \cdot \mathbf{M}_{-\mathbf{k}_2} \quad (1.22a)$$

$$N_{V, \mathbf{k}_1, \mathbf{k}_2} = \frac{(2\pi)^3}{V} \int \chi_V^*(\mathbf{k}_3 + \mathbf{k}_1) \chi_V(\mathbf{k}_3 + \mathbf{k}_2) \hat{\mathbf{k}}_3 \otimes \hat{\mathbf{k}}_3 d^3k_3. \quad (1.22b)$$

While this expression is exact under the stated assumptions, it is also not very useful, due to the double sum and the generally very complicated and highly oscillating integral. Fortunately, it simplifies significantly when V is much larger than V_{uc} in any direction where $\overline{\mathbf{M}}$ is not constant. Using that χ_V decays quickly in this case, it is not too difficult to show that

$$N_{V, \mathbf{k}_1, \mathbf{k}_2} \approx \delta_{\mathbf{k}_1, \mathbf{k}_2} N_{V, \mathbf{k}_1} \quad (1.23a)$$

$$N_{V, \mathbf{k}} = \begin{cases} \hat{\mathbf{k}} \otimes \hat{\mathbf{k}} & , \mathbf{k} \neq 0 \\ N_V & , \mathbf{k} = 0 \end{cases}. \quad (1.23b)$$

Thus, for large V , we can write

$$f_{\text{demag}, V}[\mathbf{M}'] \approx \frac{\mu_0}{2} \sum_{\mathbf{k} \in L_{\text{uc}}^*} \mathbf{M}_{\mathbf{k}} \cdot N_{V, \mathbf{k}} \cdot \mathbf{M}_{-\mathbf{k}}, \quad (1.24)$$

in correspondence to [equation \(1.16\)](#). Since the relation between \mathbf{M} and \mathbf{M}' is fully determined by specifying V , and for most purposes the two are identical, we will no longer distinguish between them in the following text.

Besides the obvious benefits for calculating the energy of a magnetic configuration, compared to [equation \(1.22\)](#), another important result of this calculation is that for large volumes contributions to the magnetization with different wave vectors \mathbf{k}_1 and \mathbf{k}_2 are coupled only negligibly by dipolar interaction. More accurately, for $\mathbf{k}_1 - \mathbf{k}_2$ in d -direction, their coupling is proportional to $(l_{\text{uc},d}/l_d)^{\sigma_d}$ for a linear extend $l_{\text{uc},d}$ of the magnetic unit cell and l_d of the whole system, with a shape- and direction-dependent exponent σ_d . For a spherical V , we find $\sigma_d = 2$, while $\sigma_d \in [1, 3]$ for a cuboid. Specifically for the mean magnetization $\mathbf{M}_{\mathbf{k}}|_{\mathbf{k}=0}$, the remaining contribution gives the right-hand side of [equation \(1.17\)](#). This term is also referred to as *shape anisotropy*, since it constitutes a generally anisotropic contribution to the energy, that depends on the shape of the sample via the demagnetization tensor N_V , see also [section 2.1](#). Especially in an experimental context, its effect is often described by combining the demagnetization field due to the mean magnetization $\mathbf{H}_{\text{demag}}[\mathbf{M}_{\mathbf{k}}|_{\mathbf{k}=0}]$ with the uniform applied *external* magnetic field \mathbf{H} into the total *internal* field \mathbf{H}_{int} . Measurements are then interpreted as functions of \mathbf{H}_{int} , instead of \mathbf{H} . For a usage example including some explanation see [\[52\]](#). It is often emphasized that for ellipsoid V , \mathbf{H}_{int} is also uniform, but this is actually only true if the whole system is truly in a single domain state. Also, for regions deep in the bulk, the difference is usually irrelevant. Note also that the only remaining information on the shape of V is contained in $N_{V,\mathbf{k}}|_{\mathbf{k}=0} = N_V$, verifying our previous claim.

2

CUBIC ANISOTROPY AND THE PHASE DIAGRAM

This chapter is about the influence of cubic magnetic anisotropy on chiral magnets, focusing primarily on the phase diagram. The first section gives a short introduction to magnetic anisotropy in the context of chiral magnets. In the following section, we will detail the method we use, before exploring the effect of cubic anisotropy on the phase diagram, while comparing the results with those of recent experiments on Cu_2OSeO_3 . Finally, in the third section, we will discuss the individual phases we find in more detail.

2.1 MAGNETIC ANISOTROPY

Magnetic materials usually have crystalline structure. Since crystal structures necessarily break the continuous rotational symmetry of space, the magnetic properties do so as well, retaining the same symmetries as the lattice. The simplest effect of such *magnetic anisotropy* is that magnetic moments will preferentially align with certain directions, determined by the crystal lattice.

Arguably the simplest type of magnetic anisotropy is *uniaxial anisotropy*, where a single axis is distinguished. This anisotropy is either labeled *easy-axis*, if magnetic moments aligned with this axis have lower energy, or *easy-plane*, if they have higher energy. To lowest order in powers of \mathbf{M} , it can be expressed as a term

$$f_{\text{uniaxial}}[\mathbf{M}](\mathbf{r}) = K (\mathbf{M} \cdot \hat{\mathbf{a}})^2 \quad (2.1)$$

in the energy density, where it is easy-axis for $K < 0$ and $\hat{\mathbf{a}}$ determines the axis. Uniaxial anisotropy is present whenever a single axis is distinguished in the crystal structure — typically in thin films, layered materials, and under application of uniaxial pressure.

While uniaxial anisotropy is often important, it does not play a role in the systems we will be studying in this chapter. In cubic crystals, such as the cubic chiral magnets we are interested in, the relevant type of anisotropy is *cubic anisotropy*. Textbook introductions to magnetic anisotropy are often only concerned with ferromagnetic materials, and so they

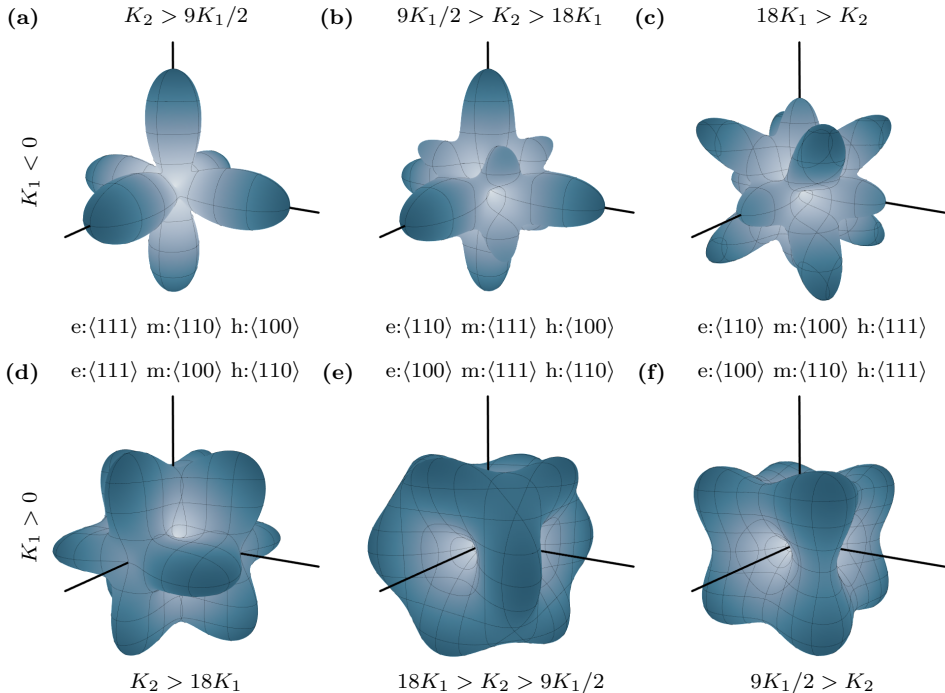


Figure 2.1: Energy surfaces for cubic crystal anisotropy as given by [equation \(2.2\)](#). For a magnetization pointing in a certain direction, both the radius and the color give the energy in arbitrary units where the minimum is shifted to zero. The axes are aligned with $\langle 100 \rangle$ -directions. Depending on the parameters K_1 and K_2 , any of the high-symmetry axes can be an easy- (e), intermediate- (m), or hard-axis (h), as designated per panel. The specific parameters used for the plots are: (a–c) $K_1 = -1$, (a) $K_2 = 0$, (b) $K_2 = -14$, (c) $K_2 = -22$, (d–f) $K_1 = 1$, (d) $K_2 = 40$, (e) $K_2 = 6$, (f) $K_2 = 0$. Panels (a) and (f) are especially important to us, since we will be neglecting K_2 .

usually give a free energy contribution like

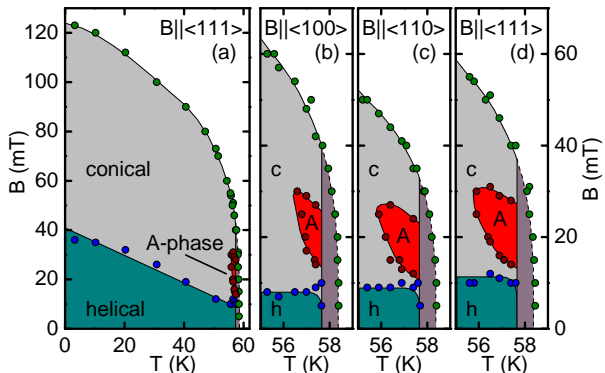
$$f_{\text{cubic}}^{\text{t.b.}}[\mathbf{M}](\mathbf{r}) = -K_1 (\alpha_1^4 + \alpha_2^4 + \alpha_3^4) - K_2 \alpha_1^2 \alpha_2^2 \alpha_3^2, \quad (2.2)$$

where α_i is the cosine of the angle between the magnetization and the crystal axis i — the i th direction cosine of the magnetization. Since we will align the crystal and coordinate axes we can write $\alpha_i = \cos(\angle(\mathbf{M}, \hat{\mathbf{e}}_i)) = M_i/|\mathbf{M}|$. Note that [equation \(2.2\)](#) in a way contains all symmetry-allowed contributions up to sixth order in the magnetization.¹ While there are other symmetry-allowed terms of the same order, they are equivalent to the terms in [equation \(2.2\)](#) up to isotropic constants. For example we could write $\alpha_1^2 \alpha_2^2 + \alpha_2^2 \alpha_3^2 + \alpha_1^2 \alpha_3^2$, which is equivalent to the K_1 contribution via $2(\alpha_1^2 \alpha_2^2 + \alpha_2^2 \alpha_3^2 + \alpha_1^2 \alpha_3^2) + (\alpha_1^4 + \alpha_2^4 + \alpha_3^4) = (\alpha_1^2 + \alpha_2^2 + \alpha_3^2)^2 = 1$.

Since we are concerned with the non-collinear magnetic structures of chiral magnets, we also need to consider contributions of cubic anisotropy containing derivatives of the magnetization. Such terms are sometimes called exchange anisotropy, but should not be confused with the exchange bias in ferromagnet-antiferromagnet interfaces, also called exchange anisotropy.

¹⁶ More accurately, we should do an expansion in powers of spin-orbit coupling, but for simplicity we will consider the expansion in powers of \mathbf{M} and the order of derivatives.

Figure 2.2: Magnetic phase diagram of Cu_2OSeO_3 for different magnetic field directions. (a) Overview of the helimagnetic phases for $\mathbf{B} \parallel \langle 111 \rangle$. (b–d) Detail close to T_c for $\mathbf{B} \parallel \langle 100 \rangle$, $\langle 110 \rangle$, $\langle 111 \rangle$. Most of the anisotropy evident in the differences between these panels is due to demagnetization effects [54]. Reproduced figure with permission from [54]. Copyright 2012 by The American Physical Society.



Some low-order terms allowed by the $P2_13$ space group are:

$$f_{\text{cubic}}^{\text{deriv.}}[\mathbf{M}](\mathbf{r}) = -K'_1 (M_x \partial_x^2 M_x + M_y \partial_y^2 M_y + M_z \partial_z^2 M_z) + K'_4 \mathbf{M} (\partial_x^4 + \partial_y^4 + \partial_z^4) \mathbf{M}. \quad (2.3)$$

Finally there is *shape anisotropy*, which is nothing but one of the effects of dipolar interaction. For any magnetic sample whose symmetry group includes the cubic symmetry group the demagnetization tensor is proportional to the three-dimensional identity matrix. This includes all cube-like objects and spheres, but neither generic cuboids nor generic ellipsoids. For all other samples the demagnetization tensor describes an anisotropic self-interaction of the mean magnetization, as given by the $\mathbf{k} = 0$ contribution in equations (1.24) and (1.23b).

Since cubic chiral magnets do not have a distinguished axis per se, uniaxial anisotropy does not play a role for bulk samples, unless uniaxial pressure is applied. For thin film samples, on the other hand, it can become a central contribution. It has been found to either increase the range of stability of the conical phase, or instead stabilize a helical and a skyrmion lattice phase, depending on the sign and magnitude of K [53]. Concerning bulk samples, experimental studies found the influence of cubic anisotropy in several chiral magnets to be small [54–56]. Figure 2.2 shows phase diagrams of Cu_2OSeO_3 for several directions of the applied magnetic field by Adams et al. According to the authors, most of the differences shown in panels (b–d) can be attributed to shape anisotropy, not cubic anisotropy.

2.2 MAPPING THE PHASE DIAGRAM

Originally, publications on Cu_2OSeO_3 reported a phase diagram as it is very typical for chiral magnets [54, 57]. As shown in figure 2.2, it contained the usual helical, conical, polarized, and skyrmion lattice (here still called A-phase) phases. Recent experiments, however, found the phase diagram to be much richer [LH2, 58, LH3]. Among other new features, which we will discuss in more detail below, they found another phase with a one-dimensionally modulated spin structure, dubbed the tilted conical phase, at low temperatures. Usually, the propagation vector \mathbf{q} of such phases is either parallel to a high-symmetry axis, when pinned by anisotropy, or parallel to the magnetic field, since, for these directions, the corresponding energy terms lower their energy. For this new phase, these two directions are identical, but, very surprisingly,

\mathbf{q} points in a different direction. For $\mathbf{B} = 0$, the anisotropy-preferred directions are the $\langle 001 \rangle$ -directions, and this new phase was only observed when also $\mathbf{B} \parallel \langle 001 \rangle$. Since it appears only for some directions of the magnetic field, the mechanism for its stabilization must clearly involve some kind of anisotropy. Since Cu_2OSeO_3 has cubic crystal structure, and the experiments were conducted on unstrained samples, uniaxial anisotropy can be ruled out. Furthermore, the tilted phase was also found in spherical samples [LH2], where no shape anisotropy is present. We will therefore take a closer look at the influence of cubic anisotropy on the magnetic phase diagram of chiral magnets.

To model the system, we will use an extension of the isotropic Ginzburg–Landau model of equations (1.13) and (1.24). Technically, Ginzburg–Landau models represent expansions of the free energy around a critical point or line. In our case, this is the paramagnetic to helimagnetic transition, that occurs at the critical temperature T_c . It might therefore be a surprising choice to use a Ginzburg–Landau model to describe effects occurring at temperatures well below T_c . It has been demonstrated, however, that this model gives very good agreement with experiments on a variety of chiral magnets [2, 7, 52]. Furthermore, we will not try to achieve quantitative agreement with the experiments, due to the number of parameters involved. Instead, we will establish phase diagrams taking the various contributions of cubic anisotropy into account, and identify the relevant parameters governing the phase diagram of Cu_2OSeO_3 .

Since it is the low temperature regime, that we are interested in, we can neglect the effects of thermal fluctuation beyond what is built phenomenologically into the Ginzburg–Landau model. Such fluctuations were previously used to explain the thermodynamic stability of the skyrmion lattice [7]. For now, we will also assume that there is no phase coexistence, and only consider states with a homogeneous phase throughout the sample. Under these assumptions, the problem of calculating a phase diagram reduces to a straight forward minimization of the free energy density, for which we use

$$f_V[\mathbf{M}] = f_{\text{base},V}[\mathbf{M}] + f_{\text{demag},V}[\mathbf{M}] + f_{\text{cubic},V}[\mathbf{M}], \quad (2.4)$$

with

$$\begin{aligned} f_{\text{cubic},V}[\mathbf{M}] = \sum_{\mathbf{k} \in L_{\text{uc}}^*} & \left[K'_1 (k_x^2 M_{\mathbf{k}}^x M_{-\mathbf{k}}^x + k_y^2 M_{\mathbf{k}}^y M_{-\mathbf{k}}^y + k_z^2 M_{\mathbf{k}}^z M_{-\mathbf{k}}^z) \right. \\ & + K'_2 (k_x k_y M_{\mathbf{k}}^x M_{-\mathbf{k}}^y + k_y k_z M_{\mathbf{k}}^y M_{-\mathbf{k}}^z + k_x k_z M_{\mathbf{k}}^x M_{-\mathbf{k}}^z) \\ & + K'_3 (k_x^2 M_{\mathbf{k}}^y M_{-\mathbf{k}}^y + k_y^2 M_{\mathbf{k}}^z M_{-\mathbf{k}}^z + k_z^2 M_{\mathbf{k}}^x M_{-\mathbf{k}}^x) \\ & + K'_4 (k_x^4 + k_y^4 + k_z^4) \mathbf{M}_{\mathbf{k}} \cdot \mathbf{M}_{-\mathbf{k}} \\ & \left. - K_1 \sum_{\substack{\mathbf{k}_2, \mathbf{k}_3, \mathbf{k}_4 \in L_{\text{uc}}^* \\ \mathbf{k} + \mathbf{k}_2 + \mathbf{k}_3 + \mathbf{k}_4 = 0}} (M_{\mathbf{k}}^x M_{\mathbf{k}_2}^x M_{\mathbf{k}_3}^x M_{\mathbf{k}_4}^x + M_{\mathbf{k}}^y M_{\mathbf{k}_2}^y M_{\mathbf{k}_3}^y M_{\mathbf{k}_4}^y + M_{\mathbf{k}}^z M_{\mathbf{k}_2}^z M_{\mathbf{k}_3}^z M_{\mathbf{k}_4}^z) \right]. \end{aligned} \quad (2.5)$$

Here, K'_1 , K'_2 , and K'_3 parameterize all anisotropic contributions allowed by the $P2_13$ space group up to order $\mathbf{k}^2 \mathbf{M}^2$. Similarly, K_1 gives the only symmetry-allowed term up to order $\mathbf{k}^0 \mathbf{M}^4$, see the previous section. Finally, we also include K'_4 as a common example for higher-order terms. Note that the term proportional to K_1 in equation (2.5) is not quite identical to that from equation (2.2), since \mathbf{M} is not normalized in the Ginzburg–Landau

(a)	phase	L_{uc}^* -parameters	reciprocal lattice L_{uc}^*	$ L_{\text{uc}}^* $
	FM	–	$\{0\}$	1
	conical	$n \in \mathbb{R}, \mathbf{q} \in \mathbb{R}^3$	$\text{span}(\mathbf{q}) \cap B_{n \mathbf{q} }$	$2n + 1$
	$\square\text{SkX}_A$	$n, q \in \mathbb{R}$	$\text{span}(q\hat{\mathbf{e}}_x, q\hat{\mathbf{e}}_y) \cap B_{nq}$	$\sim \pi n^2$
	$\square\text{SkX}_B$	$n, q \in \mathbb{R}$	$\text{span}\left(\frac{q}{\sqrt{2}}(\hat{\mathbf{e}}_x + \hat{\mathbf{e}}_y), \frac{q}{\sqrt{2}}(\hat{\mathbf{e}}_x - \hat{\mathbf{e}}_y)\right) \cap B_{nq}$	$\sim \pi n^2$
	$\triangle\text{SkX}$	$n, q, \kappa \in \mathbb{R}$	$\begin{pmatrix} 1 & 0 & 0 \\ 0 & \kappa & 0 \\ 0 & 0 & 1 \end{pmatrix} (\text{span}(q\hat{\mathbf{e}}_x, \frac{q}{2}(\hat{\mathbf{e}}_x + \sqrt{3}\hat{\mathbf{e}}_y)) \cap B_{nq})$	$\sim 3.6n^2$

(b)	phase	symmetries	$n = 6: L_{\text{uc}}^* $	f
	FM	$\mathbf{M}_{\mathbf{k}} = \mathbf{M}_{-\mathbf{k}}^*$	1	3
	conical	$\mathbf{M}_{\mathbf{k}} = \mathbf{M}_{-\mathbf{k}}^*$	13	39
	$\square\text{SkX}_A$	$\mathbf{M}_{\mathbf{k}} = \mathbf{M}_{-\mathbf{k}}^*, \mathbf{M}_{\mathbf{k}} = R_{\hat{\mathbf{e}}_z, -\pi/2} \cdot \mathbf{M}_{R_{\hat{\mathbf{e}}_z, \pi/2} \cdot \mathbf{k}},$ $\mathbf{M}_{\mathbf{k}} = -R_{\hat{\mathbf{e}}_x, \pi} \cdot \mathbf{M}_{R_{\hat{\mathbf{e}}_x, \pi} \cdot \mathbf{k}}$	113	48
	$\square\text{SkX}_B$	$\mathbf{M}_{\mathbf{k}} = \mathbf{M}_{-\mathbf{k}}^*, \mathbf{M}_{\mathbf{k}} = R_{\hat{\mathbf{e}}_z, -\pi/2} \cdot \mathbf{M}_{R_{\hat{\mathbf{e}}_z, \pi/2} \cdot \mathbf{k}},$ $\mathbf{M}_{\mathbf{k}} = -R_{\hat{\mathbf{e}}_x, \pi} \cdot \mathbf{M}_{R_{\hat{\mathbf{e}}_x, \pi} \cdot \mathbf{k}}$	113	48
	$\triangle\text{SkX}$	$\mathbf{M}_{\mathbf{k}} = \mathbf{M}_{-\mathbf{k}}^*, \mathbf{M}_{\mathbf{k}} = R_{\hat{\mathbf{e}}_z, \pi} \cdot \mathbf{M}_{R_{\hat{\mathbf{e}}_z, \pi} \cdot \mathbf{k}},$ $\mathbf{M}_{\mathbf{k}} = -R_{\hat{\mathbf{e}}_y, \pi} \cdot \mathbf{M}_{R_{\hat{\mathbf{e}}_y, \pi} \cdot \mathbf{k}}$	127	100

Table 2.1: (a) States considered for calculation of phase diagrams and their reciprocal lattices. Also listed are the parameters we use to describe L_{uc}^* , and its cardinality $|L_{\text{uc}}^*|$. A closed ball of radius r around the origin is denoted by $B_r = \{\mathbf{x} \in \mathbb{R}^3 \mid |\mathbf{x}| \leq r\}$. (b) A list of symmetries assumed for each phase, along with the cardinality $|L_{\text{uc}}^*|$ and the remaining degrees of freedom f after the application of all symmetries—both for $n = 6$ where applicable. Note that with minimal symmetry $f = 3|L_{\text{uc}}^*|$, as is the case for the ferromagnetic and conical phases. Rotations by ϕ around \mathbf{v} are denoted by $R_{\mathbf{v}, \phi}$.

model. It should also be noted that [equation \(2.5\)](#) assumes that the coordinate system is aligned with the crystal axes. We choose the conventional axes $\hat{\mathbf{e}}_x \parallel [100]$, $\hat{\mathbf{e}}_y \parallel [010]$, and $\hat{\mathbf{e}}_z \parallel [001]$.

The free parameters of the model are the reciprocal lattice L_{uc}^* and the components $\mathbf{M}_{\mathbf{k}} \in \mathbb{C}^3$ of the magnetization. Due to the rather large number of degrees of freedom involved when using large reciprocal lattices, we will treat each phase separately on a tailored reciprocal lattice. This way, we are able to make use of the respective symmetries of the states to decrease the number of free parameters for the minimization process by up to $\sim 86\%$, enabling us to compute detailed phase diagrams in a reasonable time frame. [Table 2.1](#) lists the states we consider for those phase diagrams, together with details on the corresponding parameters used for the minimization. They include a polarized state (FM), helical/conical states, two skyrmion square lattices ($\square\text{SkX}_A/\square\text{SkX}_B$) rotated by $\frac{\pi}{4}$ relative to each other, and a triangular skyrmion lattice ($\triangle\text{SkX}$) with an additional parameter κ for allowing anisotropy-induced deformation. The reciprocal lattices L_{uc}^* of the four types of modulated states are truncated using a spherical cutoff of radius $n|\mathbf{q}|$, where \mathbf{q} is a reciprocal lattice vector and $n \in \mathbb{R}$. In the case of the two-dimensional lattices, n is sometimes referred to as the “number

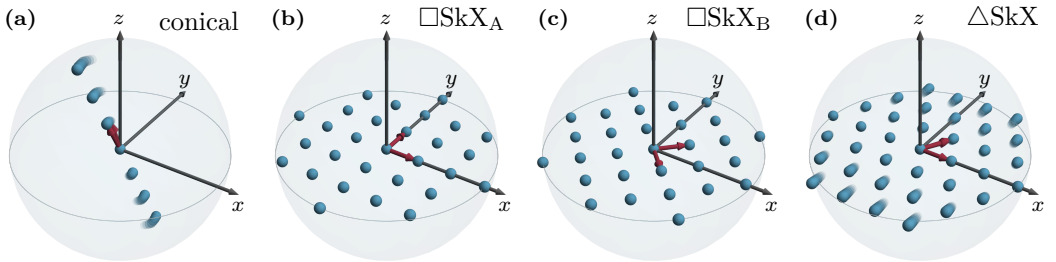


Figure 2.3: Reciprocal lattices of the four modulated states considered. (a) For the conical state, the lattice consists of points on a single line. This line can be oriented in any direction. (b) The first square lattice is aligned with the x - and y -axes. (c) The second square lattice is simply rotated by $\frac{\pi}{4}$ around z with respect to the first. (d) The triangular lattice is the only one that does not use the same spherical momentum cutoff $n|\mathbf{q}|$ as the others. For $\kappa > 1$ (< 1) it effectively uses an ellipsoid cutoff region that is elongated (shortened) in y -direction. Each lattice is drawn for $n = 3$ and fixed $|\mathbf{q}|$. The effect of the remaining parameters ((a) $\hat{\mathbf{q}}$ (b–c) none (d) κ) is hinted at by a blurring effect.

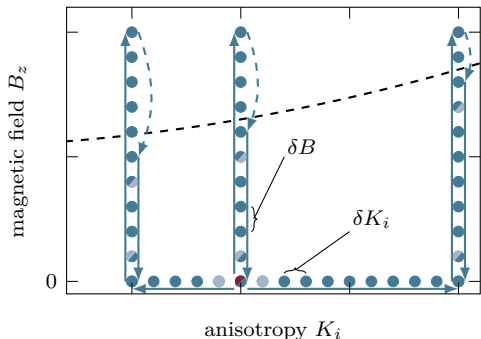
of rings” in the lattice. Importantly, the cutoff scales with the reciprocal lattice vector during the minimization procedure, which makes the algorithm simpler and more stable. For the same reason, the deformation of the triangular skyrmion lattice by κ is applied *after* the cutoff, see the definition of L_{uc}^* for ΔSkX in table 2.1a. Thereby, this lattice occasionally includes points outside the cutoff region, or disregards points that would have been included had the deformation been applied first. The four non-trivial reciprocal lattices are visualized in figure 2.3.

While the mathematical description of each states is tailored towards a specific phase, each of them can take on values corresponding to states of other phases. They are defined by the respective reciprocal lattice L_{uc}^* and the corresponding symmetries we enforce. A polarized state $\mathbf{M} = |\mathbf{M}|\hat{\mathbf{e}}_z$, for example, is a valid solution of any of the listed sets of symmetries and lattices. The conical state, in particular, actually permits any one-dimensionally modulated state. We use it to describe the conical, helical, and tilted conical phases. This phenomenon can become a problem when the minimization results in a state corresponding to a different than the intended phase. A particularly relevant example is how a minimization for strong magnetic field will often result in a polarized state, even if we use the description intended for a skyrmion lattice. In some cases, the intended phases would have lower energy and the minimization simply get stuck in a higher-energy local minimum. However, even when the result has lower energy than the intended phase, this complicates the generation of phase diagrams, because we have to take care in identifying the phase the result corresponds to. One way we use to mitigate this problem to some extent will be discussed below.

At selected points in parameter space, we also searched for phases that do not satisfy the symmetries of any of the listed states. By using a general three-dimensional reciprocal lattice with minimal symmetry $\mathbf{M}_{\mathbf{k}} = \mathbf{M}_{-\mathbf{k}}$, any magnetic configuration can, in principle, be parameterized. All states identified in this manner were either close to one of the listed states, or much higher in energy, see also below.

Having reduced the number of internal degrees of freedom by enforcing the symmetries we expect the respective states to have, we can also reduce the number of external parameters

Figure 2.4: Three exemplary parameter paths used to generate phase diagrams. Points mark the parameters for which a minimization is performed, where the color shows the origin of the initial configuration — from \bullet a script, \circ a previous result, or \circ an interpolation of previous results. Points with two colors are visited twice with different types of inputs, where the top-left color corresponds to the first minimization. Points are visited along the paths (\rightarrow) through the anisotropy–magnetic field parameter space. The descending B -paths start at the highest B with a non-polarized result ($---$) — see the main text.



by rescaling. Mapping

$$\begin{aligned}
 \mathbf{k} &\mapsto \tilde{\mathbf{k}} \frac{D}{J}, & \mathbf{M} &\mapsto \tilde{\mathbf{M}} \frac{D}{\sqrt{JU}}, & f_V &\mapsto \tilde{f}_V \frac{D^4}{J^2 U}, \\
 r_0 &\mapsto \tilde{r}_0 \frac{D^2}{J}, & \mathbf{B} &\mapsto \tilde{\mathbf{B}} \frac{D^3}{\sqrt{J^3 U}}, & K'_{1/2/3} &\mapsto \tilde{K}'_{1/2/3} J, & K'_4 &\mapsto \tilde{K}'_4 \frac{J^3}{D^2}, & K_1 &\mapsto \tilde{K}_1 U,
 \end{aligned}$$

we arrive at set of dimensionless parameters, while, at the same time, eliminating the parameters J , D , and U from the model, at the price of introducing the new parameter $\tau = \frac{\mu_0 J}{D^2}$ in front of $f_{\text{demag},V}$. For the actual calculations we use this reduced set of dimensionless parameters. For clarity, however, we will state the dimensionful parameters whenever appropriate.

Neglecting anisotropy for a moment, τ is identical with the so-called internal conical susceptibility $\chi_{\text{con}}^{\text{int}} = \frac{\partial |\mathbf{M}|}{\partial |\mathbf{H}_{\text{int}}|}$, which has been reported to be $\chi_{\text{con}}^{\text{int}} \approx 1.76$ in Cu_2OSeO_3 [52]. Although this identity no longer holds exactly in the presence of anisotropy, it will still hold approximately, as long as the anisotropy is weak. Therefore, and since we do not have any better data on its actual value, we will use $\tau = 1.76$ for all calculations shown here, unless otherwise stated. Since the experiments found the tilted conical phase for a magnetic field $\mathbf{B} \parallel \langle 001 \rangle$, we will also restrict the external field to such a direction and write $\mathbf{B} = B_z \hat{\mathbf{e}}_z$, further reducing the number of external parameters. For the temperature-like Ginzburg–Landau parameter r_0 , the demagnetization factors N_i , and the maximal order of \mathbf{k} -modes n we will use $r_0 = -100 \frac{D^2}{J}$, $N_i = \frac{1}{3}$, and $n = 6$, respectively, unless otherwise stated.

For the minimization we use a quasi-Newton algorithm built into Wolfram Mathematica. Since this is a method for searching local minima, we have to provide some starting configuration. Depending on situation and objective, we do this in one of the following ways: by choosing a random state, scripting a representative configuration by hand, inserting the result from a previous minimization with similar external parameters, or interpolating from several previous results. For selected parameter sets, we generated several thousand random configurations as input for the minimization procedure on a minimal-symmetry reciprocal lattice, to check for relevant states beyond those listed in table 2.1. We found that while all qualitatively different results have significantly higher energy, there are often several similar configurations

with comparable energy. This complicates the task of reliably identifying the minimal-energy configuration across a range of external parameters. Therefore we implemented the following procedure when compiling phase diagrams, which is also visualized in [figure 2.4](#).

We start with a scripted configuration as input for a minimization without any anisotropy. The resulting configuration is then used as input for a minimization with small anisotropy δK_i in one of the $K'_{1/2/3/4}$, K_1 parameters. Successive minimizations with anisotropy further increased in steps of δK_i receive a configuration interpolated from the two preceding minimizations as input until a target K_i is reached. At that point the same procedure is used to first increase the magnetic field in steps of δB , but with the final result of the previous path as initial input instead of a manually scripted configuration. Finally, we repeat the procedure once more to decrease B again to 0. There, however we do not start at the final value of B and the corresponding result, but rather at the highest value of B for which the resulting configuration shows a minimum of spatial variation — i. e. a non-vanishing $|\mathbf{M}_{\mathbf{k}}|$ for at least one value of $\mathbf{k} \neq 0$. The reason is that otherwise the minimization would in some cases start with a polarized initial state, and often stay in this local minimum, instead of giving results for the intended phase. When computing phase diagrams of other parameters, like r_0 , we use the appropriate equivalent, adding a third path segment to tune up the corresponding parameter where necessary. Note that some of the presented results, particularly those with $r_0 = -1000 \frac{D^2}{J}$, were obtained with simpler parameter paths, relying more on scripted input.

Beyond improving the stability of the minimization, the hysteresis-loop-like increasing–decreasing- \mathbf{B} part of this procedure is very useful whenever there is a first-order transition between states of the same group. At low magnetic fields, for example, we often find a triangular skyrmion lattice state featuring strongly elongated skyrmions, sometimes called bimerons, approximating a helical state, which is much closer to the actual ground state in this region. This state then changes to a state with properly localized nearly circular skyrmions in a first order transition between metastable states. By first increasing then decreasing the magnetic field, we are much more likely to find the optimal state for all parameters, even in the vicinity of such transitions. For the final phase diagram, we select for each point the state with minimal energy, considering and comparing all the different phases and ways of generation.

Using this procedure, we compute several magnetic phase diagrams as a function of the magnetic field and the various anisotropy parameters. For simplicity, we only choose one anisotropy parameter to be non-zero for now. As candidate states we consider all states listed in [table 2.1](#). For the conical state specifically, we find that the best results are obtained by fixing the direction of \mathbf{q} , and repeating the minimization for different directions, tracing a path in parameter space as described for each $\hat{\mathbf{q}}$. Since the individual anisotropic contributions to the energy all favor \mathbf{q} to be either parallel to $\langle 001 \rangle$, $\langle 111 \rangle$, or $\mathbf{B} \parallel \hat{\mathbf{e}}_z$, we expect \mathbf{q} to lie on the high-symmetry line between $\hat{\mathbf{e}}_z$ and $(1, 1, 1)^T$. Using spherical coordinates for \mathbf{q} , we therefore fix its azimuthal angle to $\phi = \frac{\pi}{4}$ for now and vary its polar angle as $\theta \in [0, 1]$, where $\mathbf{q} \parallel (1, 1, 1)^T$ corresponds to $\theta = \arctan(\sqrt{2}) \approx 0.955$. In the next section, we will check this assumption. Beyond that, the most likely candidate for a one-dimensionally modulated state is a helical phase with $\mathbf{q} \parallel \hat{\mathbf{e}}_x \perp \mathbf{B}$, which we also consider.

[Figure 2.5](#) shows the resulting phase diagrams and a set of exemplary energy curves used in generating these. In panel (a), the phase diagram as a function of K'_1 and B_Z is shown. For $K'_1 = 0$, we find the two phases expected in a bulk chiral magnet without anisotropy — a conical phase with $\mathbf{q} \parallel \mathbf{B}$ at low magnetic fields and a ferromagnetic phase (FM) at high fields.

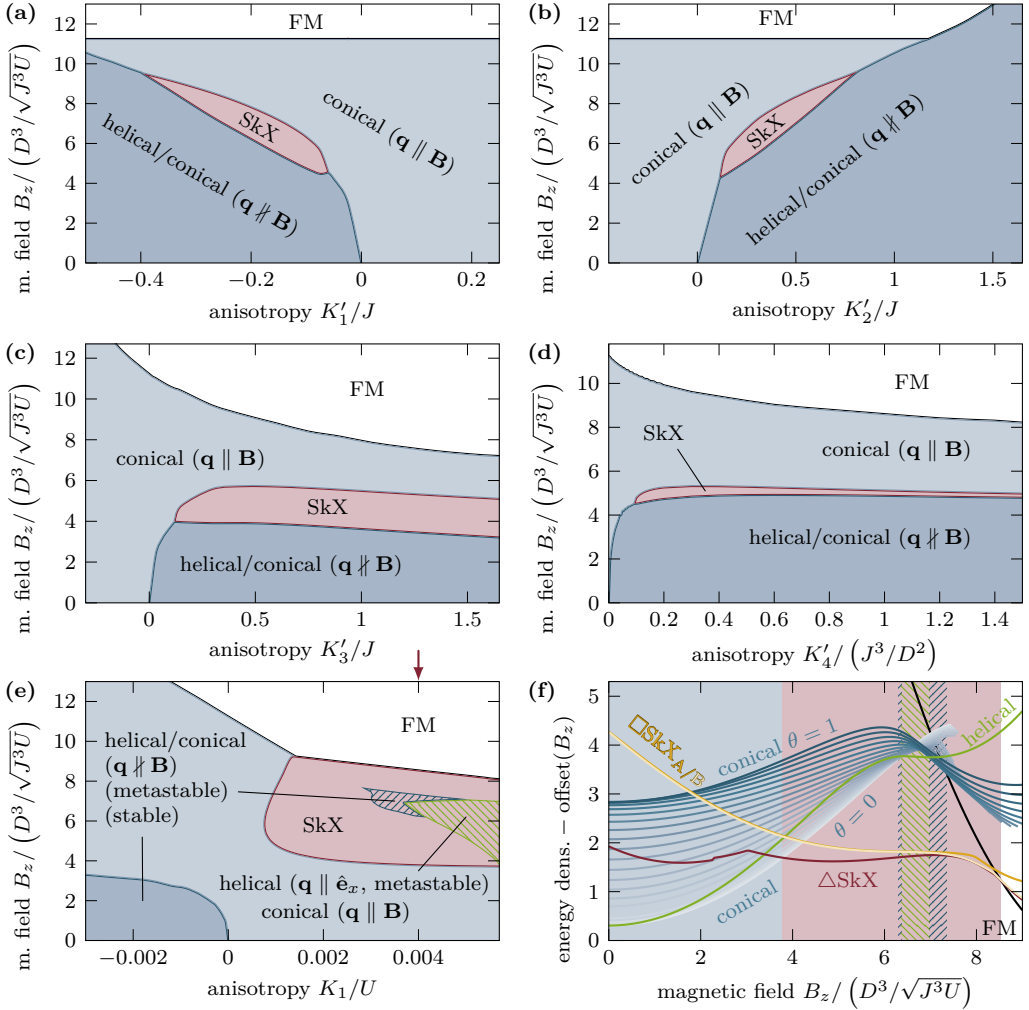


Figure 2.5: Magnetic phase diagrams as a function of magnetic field and anisotropy parameters and exemplary energy functions. (a–d) Phase diagrams as a function of anisotropy $K'_{1/2/3/4}$ and magnetic field $\mathbf{B} \parallel \hat{\mathbf{e}}_z \parallel [001]$. Phases occurring are: polarized phase (FM, white), conical phase with $\mathbf{q} \parallel \mathbf{B}$ (light blue), helical/conical phase with $\mathbf{q} \not\parallel \mathbf{B}$ (dark blue, for more information see next section), and skyrmion lattice (SkX, red). (e) Phase diagram as a function of anisotropy K_1 and magnetic field $\mathbf{B} \parallel \hat{\mathbf{e}}_z \parallel [001]$. Additional occurring phases are: metastable helical/conical phase with $\mathbf{q} \not\parallel \mathbf{B}$ (shaded dark blue) and metastable helical phase with $\mathbf{q} \parallel \hat{\mathbf{e}}_x$ (shaded green). (f) Exemplary energy density curves as used in the generation of the phase diagrams. Shown for $K_1 = 0.004U$ as marked by the red arrow in (e). For better visibility a B_z -dependent offset was subtracted from the energy densities. The respectively lowest energy density determines which phase occurs in the phase diagram. Between $B_z \approx 6.3 D^3/\sqrt{J^3U}$ and $B_z \approx 7.3 D^3/\sqrt{J^3U}$, the lowest-energy metastable state is a tilted conical state ($\theta \neq 0$, blue) or a helical state ($\mathbf{q} \parallel \hat{\mathbf{e}}_x$, green). This defines the shaded regions in (e) and (f). For a more detailed discussion see the main text.

A helical phase does not appear for $K'_1 = 0$, since without anisotropy, the conical state will have lower energy for any finite magnetic field, while at $\mathbf{B} = 0$ the conical and helical states are identical. For $K'_1 > 0$, we find no change in the phases up to the highest K'_1 we used. This is easily understood by examining the structure of the K'_1 -term. Since the conical state with $\mathbf{q} \parallel \mathbf{B} \parallel \hat{\mathbf{e}}_z$ has $M_{\mathbf{k}}^z|_{\mathbf{k} \neq 0} = 0$, and the polarized state is not modulated, it evaluates to zero for both of them. As the term can only be positive for positive K'_1 , both states represent local minima and are unchanged by $K'_1 > 0$. It should be noted though, that for very strong anisotropy, the true ground state will likely be a very different state that we do not consider in our analysis. Since the term does not vanish for helical or conical states with $\mathbf{q} \not\parallel (001)$, we conclude that the easy axes for these states are the $\langle 001 \rangle$ -directions. A phase transition between distinct helical and conical phases should therefore exist for $\mathbf{B} \not\parallel \hat{\mathbf{e}}_z$.

For $K'_1 < 0$, the situation is different. First, we do find a helical-like one-dimensionally modulated state with $\mathbf{q} \not\parallel \mathbf{B}$, that is distinct from the conical phase with $\mathbf{q} \parallel \mathbf{B}$. The critical magnetic field required to transition to the conical phases rises with increasing $|K'_1|$. Such behavior should be expected, given that stronger anisotropy should result in stronger pinning. For an intermediate range of K'_1 values, a skyrmion lattice phase (SkX) appears on the boundary between the 1D-modulated states. It only covers a relatively small range of magnetic fields, but extends along the phase boundary. We will discuss the precise nature of both the skyrmion lattice phase and the one-dimensionally modulated phase in detail in the next section, but let us note that the latter mostly corresponds to a helical phase with $\mathbf{q} \parallel (1, 1, 1)^T$. Important for now is the observation that it extends down to $\mathbf{B} = 0$, which does not match the experimental results for the tilted conical phase of Cu_2OSeO_3 . Note that for $K'_{1/3} < -\frac{J}{2}$ the model becomes unstable.

The phase diagram as a function of K'_2 and \mathbf{B} , shown in [figure 2.5b](#), is very similar to that of K'_1 and \mathbf{B} . By identifying $K'_1 \hat{=} -K'_2/2$, they appear nearly identical within the region $-\frac{J}{2} < K'_1 < \frac{J}{4}$. Analytically this can be understood in a zeroth order approximation. We first calculate the optimal conical solution for $f_{\text{base},V}[\mathbf{M}]$ with $\mathbf{B} = 0$ (i. e. no magnetic field, dipolar interaction, or anisotropy), which is easy to obtain. Then, we calculate the anisotropy energy of this solution, once with $\mathbf{q} = \frac{D}{J}\hat{\mathbf{e}}_z$ and once with $\mathbf{q} = \frac{D}{J}(1, 1, 1)^T$. The respective resulting energies are indeed identical if $K'_1 = -K'_2/2$. Numerically, we find the terms typically differing by a few percent at most, except in cases where both are very small. It should be noted, though, that this correspondence is not universal — not even approximately. For example, according to the correspondence the model should become unstable at $K'_2 > 1$. Numerically, we only find an instability at $K'_2 > 2$.

In contrast to the relevant contributions of the two previously discussed phase diagrams, the K'_3 -term directly couples to a conical state with $\mathbf{q} \parallel \hat{\mathbf{e}}_z$. Consequently, the conical–polarized phase transition is not independent of K'_3 , as is evident in [figure 2.5c](#). Still, the resulting phase diagram has several similarities with the previous ones. Again, we find a one-dimensionally modulated state with $\mathbf{q} \not\parallel \mathbf{B}$ at low fields, distinct from the usual conical state with $\mathbf{q} \parallel \mathbf{B}$ at higher fields. As before, we find a skyrmion lattice phase on the boundary between the two phases above some critical anisotropy strength. Here, however, the skyrmion lattice extends up to very high K'_3 . It also occurs in a wider range of magnetic fields, relative to the other helimagnetic phases.

The phase diagram for K'_4 in [figure 2.5d](#) is again similar to the previous one, but the similarity is much less pronounced than in the case of K'_1 and K'_2 . Here the similarity is

merely qualitative. Quantitatively, the two phase diagrams are rather different. In particular, the skyrmion lattice phase occurs in a much narrower range of magnetic fields. Note that the model becomes unstable for any $K'_4 < 0$, since a k_i^4 -term will always dominate the \mathbf{k}^2 Heisenberg exchange coupling at large k_i , resulting in $\lim_{k_i \rightarrow \pm\infty} (f_V) = -\infty$ for a negative prefactor.

Finally, the phase diagram as a function of K_1 and B_z is shown in [figure 2.5e](#). For $K_1 < 0$ it loosely resembles the already discussed phase diagrams, in that it includes a conical phase with $\mathbf{q} \parallel \mathbf{B}$ at high fields and a one-dimensionally modulated state with $\mathbf{q} \nparallel \mathbf{B}$ at low fields. Here, however, no skyrmion lattice phase appears on the boundary between the two up to the highest negative K_1 explored. Instead, such a phase appears between the polarized and conical phases for $K_1 \gtrsim 7.6 \cdot 10^{-4}U$. It covers a much larger portion of the phase diagram than even the skyrmion lattice phase occurring for K'_3 . The most significant difference to the other phase diagrams, however, is the appearance of additional helical/conical states for $K_1 \gtrsim 0.0028U$. While these two states appear only metastably in the explored parameter region, they do show the attributes we are looking for to explain the existence of a tilted conical phase in Cu_2OSeO_3 , namely $\mathbf{q} \nparallel \mathbf{B}$ and a minimal $B_z > 0$.

Since, for most parameter regimes, there are many possible metastable states, we should take a closer look at why these states are special. [Figure 2.5f](#) shows the energy density of the states we consider as a function of the magnetic field for $K_1 = 0.004U$. This value is also marked by a red arrow in [figure 2.5e](#). The plots in panel (f) nicely demonstrate how the phase diagrams are generated. For every point in parameter space, the phase with lowest free energy density is identified as the ground state. In the present case, at $K_1 = 0.004U$, this leads to a conical state with $\theta = 0$ ($\mathbf{q} \parallel \hat{\mathbf{e}}_z$) for low fields, followed by a triangular skyrmion lattice for intermediate fields and a ferromagnetic phase for the highest magnetic fields. Note that while the energy of the two square skyrmion lattices is always higher than that of the triangular lattice, they come very close for $B_z \approx 7.5 D^3 / \sqrt{J^3 U}$. Indeed, around that value and above, the energy of the second square lattice ($\square\text{SkX}_B$) is almost identical to that of the triangular lattice. We will discuss this feature in more detail in the next section. Regarding the reason why we single out these two states from all metastable states we consider, in their respective regions they are the lowest-energy states that do not contain skyrmions. The absence of skyrmions, as it turns out, might be a significant factor. Here, the extraordinary stability of skyrmions comes into play. The same energy barrier that prevents skyrmions from being easily destroyed can also prevent them from being easily created. After all, we are currently discussing the low temperature regime, where skyrmions have been shown to be metastable with very long lifetimes [20]. This could easily mean that, depending on the magnetic field and temperature history, an experiment might well find a metastable tilted conical phase by simply not being able to reach the skyrmion lattice phase in any reasonable amount of time.

At this point, we should take a closer look at the experimental results. Two independent studies, explored the phase diagram of Cu_2OSeO_3 around the same time [LH2, 58]. Both used small-angle neutron scattering (SANS) to image the momentum-space structure of the magnetization. Both data sets show, besides the known phases and the tilted conical phase we already mentioned, a weak ring-like structure of neutron intensity, shown in [figure 2.6e](#). It appears for very similar conditions as the tilted conical phase. Chacon et al. were able to show that this ring actually corresponds to a disordered skyrmion lattice [LH2]. By slightly rotating their sample back and forth in the magnetic field, the ring changed into the six-fold pattern known from SANS images of triangular skyrmion lattices [7], as shown in [figure 2.6f](#)—

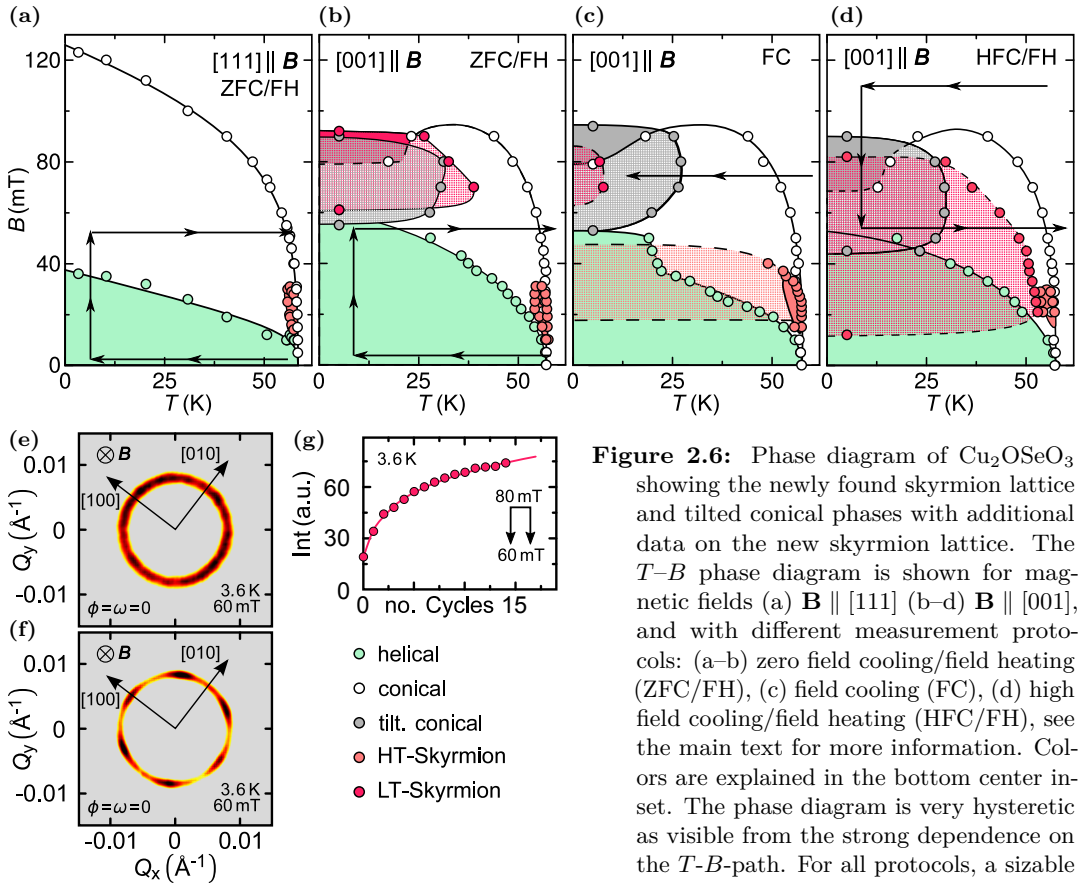


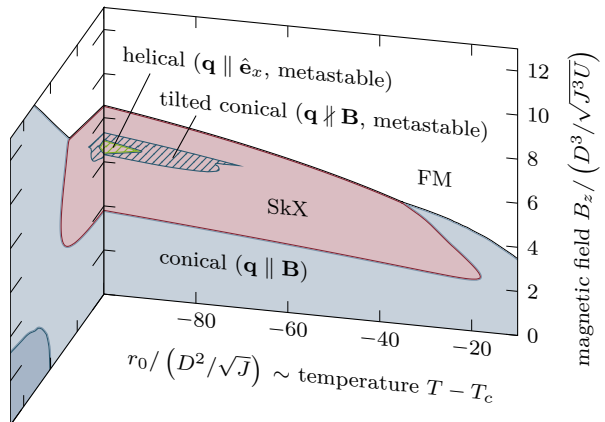
Figure 2.6: Phase diagram of Cu_2OSeO_3 showing the newly found skyrmion lattice and tilted conical phases with additional data on the new skyrmion lattice. The T - B phase diagram is shown for magnetic fields (a) $\mathbf{B} \parallel [111]$ (b-d) $\mathbf{B} \parallel [001]$, and with different measurement protocols: (a-b) zero field cooling/field heating (ZFC/FH), (c) field cooling (FC), (d) high field cooling/field heating (HFC/FH), see the main text for more information. Colors are explained in the bottom center inset. The phase diagram is very hysteretic as visible from the strong dependence on the T - B -path. For all protocols, a sizable tilted conical phase appears. The extend

of the newly found skyrmion lattice depends strongly on the protocol. In SANS-data it appears as a ring (e), showing its lack of order. By slightly tilting the sample in the magnetic field, it can be ordered, showing the usual six spots (f). By repeatedly raising and lowering the magnetic field, the intensity of the skyrmion-related signal increases (g), indicating that the skyrmion lattice actually is the ground state in that region and the tilted conical state is merely metastable. Figure adapted from [LH2] with permission.

the skyrmion lattice ordered. Furthermore, as shown in figure 2.6g, by repeatedly raising and lowering the magnetic field, they were able to enhance the corresponding signal by more than a factor of five, indicating that the ground state might indeed be a skyrmion lattice in that region.

Chacon et al. carefully mapped the phase diagram of a spherical single crystal of Cu_2OSeO_3 . Using the SANS patterns to identify the various phases, the performed different temperature-magnetic field protocols to also explore its hysteretic properties. The results are summarized in figures 2.6a to 2.6d. Panel (a) shows the same data as figure 2.2a, with $\mathbf{B} \parallel [111]$ and only the commonly known phases occurring. The helical phase is shown in green, the skyrmion lattice phase in orange, and the conical, polarized, and paramagnetic phases in white. The

Figure 2.7: Phase diagram as a function of r_0 and B_z . Drawn together with a part of the K_1 – B_z phase diagram to visualize the connection. The newly found skyrmion lattice phase (SkX) covers much of the phase diagram. Within is a small area where a metastable tilted conical phase is the lowest-energy state that does not contain skyrmions. It surrounds an area where a helical state fulfills this condition. At low (high) fields we find the usual conical (polarized) states. Calculated for $K_1 = 0.004U$ as visualized here and by the red arrow in figure 2.5e.



black arrow visualizes the measurement protocol used for this data. It consists of cooling the sample without a magnetic field, turning the field up to the desired value, and only then taking measurements while heating the sample. The abbreviated name for this scheme, zero field cooling/field heating (ZFC/FH), is also given in the image. Figure 2.6b shows results obtained with the same protocol, but for $\mathbf{B} \parallel [001]$. It shows a significantly larger helical phase, and above it the two new coexisting phases superimposed. The tilted conical phase is shown in gray, while the new skyrmion phase is shown in magenta. In panel (c), data measured with a different protocol is shown. Here, the sample was cooled under a magnetic field $\mathbf{B} \parallel [001]$, while taking measurements (field cooled: FC). With this protocol, the newly found skyrmion lattice phase is much diminished and confined to a small region inside the tilted conical phase. The original skyrmion lattice phase, on the other hand, is metastably extended down to the lowest measured temperatures, highlighting again the stability of skyrmions. Finally, by following a temperature–magnetic field protocol similar to the first one, where, instead of cooling without a magnetic field, they cooled in a strong field (high field cooling/field heating: HFC/FH), they recorded the data shown in figure 2.6d. Here, the new skyrmion lattice phase covers a large portion of the phase diagram.

An important observation is that for all three measurement protocols, the newly found skyrmion lattice phase only appears after the system is driven through a rather small region of the phase diagram, contained within the tilted conical phase. After it is generated, however, it is remarkably stable. Together with the strengthening of the skyrmion signal when cycling the magnetic field, we conclude that the new skyrmion lattice indeed represents the ground state in some part of the phase diagram. Unfortunately, it is not possible to reliably determine this region from the present data. We can only deduce the outer bounds of it by taking the largest extend of the newly found skyrmion lattice phase throughout all measurement protocols. The result is fully consistent with the prediction of a purely metastable tilted conical phase surrounded by a skyrmion lattice.

In order to be better able to compare our theoretical results with the experimental temperature–magnetic field phase diagram, we have to vary the temperature-like parameter r_0 . A corresponding phase diagram is shown in figure 2.7. It was calculated for $K_1 = 0.004U$,

as indicated by the red arrow in figure 2.5e. It is drawn together with most of the K_1 - B_z phase diagram of figure 2.5e to visualize the context and connection. In it, we find a large skyrmion lattice phase surrounding the metastable tilted conical phase. This fits nicely with our interpretation of the experimental results. What the experiments did not find is the metastable helical phase with $\mathbf{q} \parallel \hat{\mathbf{e}}_x \perp \mathbf{B}$ that replaces the tilted conical state as the lowest-energy non-skyrmion state. There are several aspects to this. On the one hand, since we do not have a full quantitative description of Cu_2OSeO_3 and the appearance of this metastable state is a rather small effect that might well vanish for slightly different parameters, this discrepancy should not be surprising. It notably does not invalidate our findings. On the other hand, it might actually be a correct description of the system, but the experiments simply did not detect this state. It is, after all, just a metastable state and it might simply not have been realized in the sample. Interestingly, the area where we identify this helical state corresponds rather well to the area where, in the experiments, the new skyrmion phase was always generated. Chacon et al. already speculated that the tilted conical state might help nucleate the skyrmion lattice. The same role might also be played by this helical state. This is corroborated by the facts that its structure is much closer to that of the skyrmion lattice than the structure of the tilted conical is, and that transitions between a helical and a skyrmion lattice state are well documented, see for example [19] for a theoretical treatment.

Note that we do not map the region close to $r_0 = 0$. It has been shown that the influence of fluctuations is key for describing this area of the phase diagram such that it matches the experimental results. In particular, the previously known skyrmion lattice phase was found to critically depend on the presence of Gaussian fluctuations [7]. Since, however, we neglect these fluctuations, we can not reliably make any predictions for this area. In particular, we can not make any definite statements on the influence of anisotropy on the high-temperature skyrmion lattice phase. Interestingly, however, we do see that the skyrmion lattice we find, does not stretch up into the critical region. It rather ends at parameters, where we can reasonably expect the mean-field approximation, i. e. neglecting Gaussian fluctuations, to hold. We conclude that we most likely have two separate areas in the phase diagram with skyrmion lattices. The previously known high-temperature phase, which is stabilized by fluctuations, and the new low-temperature phase, which is stabilized by anisotropy. This matches well with the experimental results. Even though this is not well visible in figure 2.6, even for the HFC/FH \mathbf{B} - T -protocol the high- and low-temperature skyrmion lattice phases have been found to be separated by a small area with minimal skyrmion-related scattering intensity.

We have demonstrated that anisotropy of the $K'_{1/2/3/4}$ -type is not easily able to stabilize a tilted conical phase that only appears for finite $\mathbf{B} \parallel \langle 001 \rangle$. While there might be a way to achieve this by combining several competing contributions of this type, this would almost certainly require fine tuning to work. K_1 , however, directly stabilizes such a state, no fine tuning required. The fact that this tilted state is only metastable is not a problem, since the experiments indicate that this is likely also true in Cu_2OSeO_3 . Indeed, there is a simple analytical argument why this works with K_1 , which is not valid for $K'_{1/2/3/4}$. To see it, let us first look at the details of a conical state under the influence of a finite magnetic field $\mathbf{B} \parallel \hat{\mathbf{e}}_z$. Its main qualitative effect is that the M_0^z -component becomes non-zero. Other components change as well, of course, but this is merely a quantitative change. The main effect of it is that the total real-space magnitude is still approximately constant $|\mathbf{M}(\mathbf{r})| \approx \sqrt{(D^2 - 2r_0J)/4JU}$, despite the change in M_0^z . The suddenly non-zero M_0^z , on the other hand, has significant consequences. Decomposing the sum in the K_1 -contribution, one of the resulting terms can

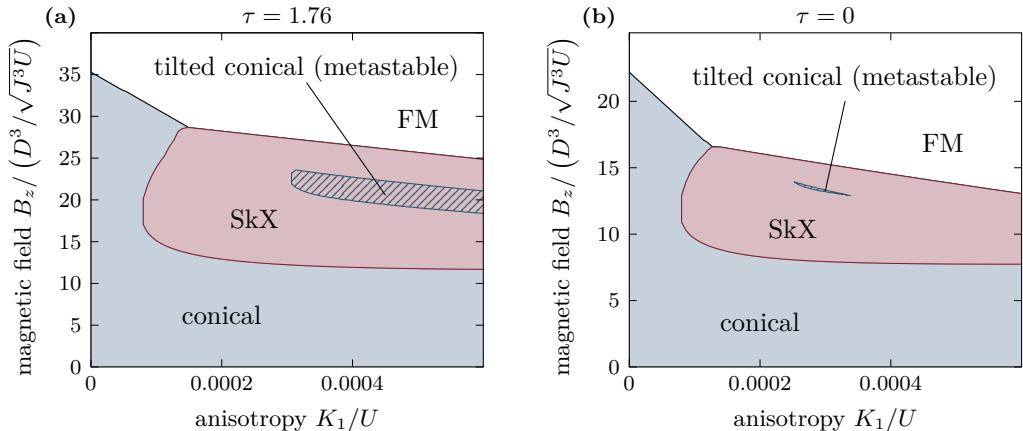


Figure 2.8: Phase diagram as a function of K_1 and B_z with and without dipolar interaction. (a) Similar to [figure 2.5e](#), but using $r_0 = -1000 D^2/J$, and $n = 4$, and with parameter ranges adapted accordingly. (b) Same as (a) except for $\tau = 0$. Except for trivial demagnetization effects the main phase boundaries are only weakly affected. The metastable tilted conical phase on the other hand is reduced to a much smaller area. This change is mostly driven by the demagnetization energy of the competing polarized state, as discussed in the main text. Redrawn from a similar figure in [\[LH2\]](#).

be written as

$$\Delta f_1[\mathbf{M}] = -6K_1 (M_0^z)^2 \sum_{\mathbf{k} \in L_{\text{uc}}^* \setminus \{0\}} M_{\mathbf{k}}^z M_{-\mathbf{k}}^z. \quad (2.6)$$

Without a magnetic field, Δf_1 does not contribute to the energy of a helical state, since $M_0^z = 0$. The usual conical state with $\mathbf{q} \parallel \mathbf{B} \parallel \hat{\mathbf{e}}_z$ is also unaffected since it has $M_{\mathbf{k}}^z = 0$ for $\mathbf{k} \neq 0$. It only gets a contribution $-K_1 (M_0^z)^4$ that does not come with the combinatorial prefactor of 6. The same is true for the polarized state. In a tilted conical state with $\mathbf{q} \not\parallel \hat{\mathbf{e}}_z$, on the other hand, both components are non-zero. Since $\Delta f_1 \leq 0$ if $K_1 > 0$, it is energetically favored by Δf_1 , with a factor $-6K_1 (M_0^z)^2$ that grows with the magnetic field. Thus, the optimal $\hat{\mathbf{q}}$ may tilt away from $\mathbf{B} \parallel \hat{\mathbf{e}}_z$, even though $\mathbf{q} \parallel \mathbf{B}$ is favored by the Zeeman term and $K_1 > 0$ favors $\mathbf{q} \parallel \langle 001 \rangle$ at $\mathbf{B} = 0$. Note that this effect requires a term of order \mathbf{M}^n with $n \geq 4$, which rules out $K'_{1/2/3/4}$. It does, however, also apply for skyrmion lattices, which explains the extent of the corresponding phase.

One thing that remains to be explored, is the influence of dipolar interaction. Up to now, we have simply taken the relevant factor as $\tau = 1.76$, in order to match Cu_2OSeO_3 . To explore the influence of dipolar interaction, and gain an understanding of other materials, we should also vary τ . [Figure 2.8](#) shows two phase diagrams as a function of K_1 and B_z , computed with identical parameters, except one uses $\tau = 1.76$, while the other neglects dipolar interaction by using $\tau = 0$. While quantitatively, the two phase diagrams are rather different, there is only one major qualitative difference. In panel (a), as in [figure 2.5e](#), we see a metastable tilted conical phase in a sizable region of the phase diagram. Without dipolar interaction, on the other hand, this shrinks down to a short and very narrow area, as shown in

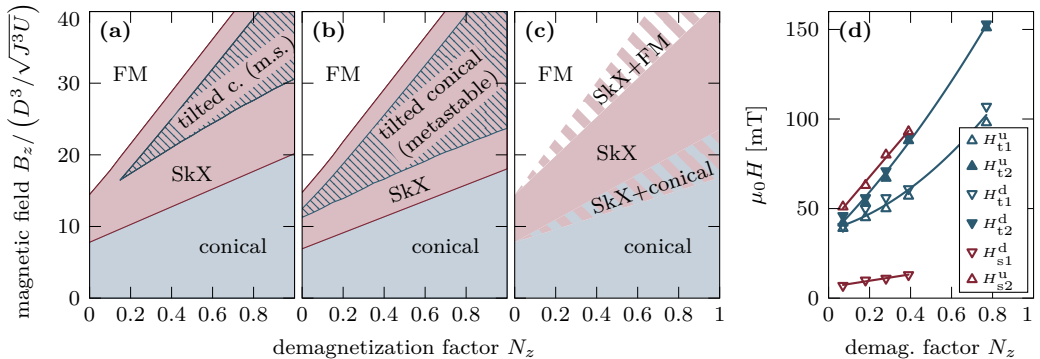


Figure 2.9: Phase diagram as a function of sample shape and magnetic field. The shape varies from infinite rod ($N_x = N_y = \frac{1}{2}$, $N_z = 0$) to infinite disk ($N_x = N_y = 0$, $N_z = 1$). (a) Parameters are $K_1 = 4 \cdot 10^{-4} U$, $r_0 = -1000 D^2/J$, and $n = 4$. The metastable tilted conical phase does not reach down to $N_z = 0$. (b) Parameters as in (a) except $K_1' = -0.06 J$. Here, the tilted conical phase does reach $N_z = 0$. (c) Dipolar interaction stabilizes regions of phase coexistence around first order phase transitions. (d) Phase boundaries for samples of Cu_2OSeO_3 with different demagnetization factors, determined from magnetization measurements. Notation: H_{pm}^o is the lower ($m = 1$) or upper ($m = 2$) critical field of the skyrmion ($p = s$) or tilted ($p = t$) phase measured with increasing ($o = u$) or decreasing ($o = d$) field. The tilted phase is found in all samples down to lowest N_z . Redrawn with permission from a similar figure in [LH3]. Original copyright 2018 by The American Physical Society.

panel (b). To understand this, remember that the definition of the shaded area required the tilted phase to be the lowest-energy non-skyrmion state. The area does not shrink because the tilted state becomes less stable by the lack of dipolar interaction, but rather because the polarized state becomes energetically more favorable in comparison. The comparatively strong dipolar interaction in Cu_2OSeO_3 with $\tau = 1.76$ brings with it a significant energy penalty $\frac{\mu_0}{2} N_z (M_0^z)^2$ for the polarized state. Consequently, the tilted conical state with lower mean magnetization \mathbf{M}_0 becomes relatively more favorable. Regarding the missing helical state in both panels, compared to figure 2.5e, we refer to the next section.

Since the energy penalty on the polarized state is proportional to the demagnetization factor N_z for $\mathbf{M} \parallel \hat{\mathbf{e}}_z$, the same effect can be observed by changing the sample shape. To be clear, changing the sample shape is not the same as changing τ , as $f_{\text{demag},V}$ from equation (1.24) contains other contributions without N_z , but the term including N_z is the most relevant one for this effect. Figure 2.9a shows a phase diagram as a function of N_z and B_z . For the parameters used, including $r_0 = -1000 D^2/J$, and $K_1 = 4 \cdot 10^{-4} U$, the tilted conical phase does not extend down to $N_z = 0$. A series of experiments were performed by Halder et al. on a range of differently shaped samples of Cu_2OSeO_3 , determining the phase boundaries from measurements of the magnetization and the susceptibility [LH3]. They found a tilted conical phase even for the most elongated (low N_z) samples available, as is shown in figure 2.9d.

There are different ways this discrepancy can be alleviated or even removed. The first thing to note is that, in the neutron scattering experiments, the system was always found to be in a state with multiple tilted conical domains, instead of a single domain. This has the effect of

reducing or eliminating the mean magnetization M_0^x and M_0^y . In our simulations, we only consider single domain states which, for the tilted conical state, results in finite M_0^x and M_0^y . Such components, however, are energetically penalized by dipolar interaction with an energy cost of

$$\frac{\mu_0}{2} \left(N_x (M_0^x)^2 + N_y (M_0^y)^2 \right). \quad (2.7)$$

This energy cost becomes even higher when N_z becomes small, as the demagnetization factors have to obey $N_x + N_y + N_z = 1$. We can include the effect of the cancellation of the mean magnetization by multiple domains into the model by artificially setting $N_x = N_y = 0$, breaking this constraint. Thereby, the mean magnetization in x - and y -direction apparently vanishes, as far as dipolar interaction is concerned. The local interactions, on the other hand, still act on the full mean magnetization. The result is that the tilted conical state has lower energy, widening the area where it represents the lowest-energy non-skyrmion state, although we find that it still does not reach down to $N_z = 0$ for these parameters.

Another way to treat the discrepancy between theory and experiment is to simply take further anisotropy contributions into account. **Figure 2.9b** shows the same N_z - B_z phase diagram as panel (a), except that we additionally set $K'_1 = -0.06 J$ in addition to $K_1 = 4 \cdot 10^{-4} U$. There, the relevant area of the tilted conical state reaches down to $N_z = 0$, removing the discrepancy.

We have thereby shown that adding cubic anisotropy of K_1 -type, together with dipolar interaction, to the basic model for chiral magnets is sufficient to explain the appearance of the two newly found phases in Cu_2OSeO_3 . To get quantitative agreement with the experiments, however, we would need to include further contributions, increasing the number of parameters of model. Beyond that, there is one more basic aspect of these phase diagrams left to explore—phase coexistence.

We find a number of different phase transitions throughout the space of explored parameters. Most of these are of first order and between phases of different mean magnetization. In such situations, dipolar interaction can broaden the transitions, creating parameter regions, where the thermodynamic ground state is not a single homogeneous phase. Instead, it is a mixture of the two bordering phases. One way to show this goes as follows.

We begin by making two simplifying assumptions, to be able to describe such a phase mixture in a way that is both general and treatable. First, we assume that within the mixture, the two phases interact solely through the homogeneous part of dipolar interaction. That means we completely neglect all domain walls, as well as the spacial distribution of the domains. Second, we assume that the transitions between the pure phases and the phase mixture are smooth, in the sense that we can introduce a phase mixing parameter p , that is 0 if we have pure phase α , and 1 if we have pure phase β , and evolves continuously. Next, for each pure phase we define

$$e_\alpha(\mathbf{M}_0) := \min_{\mathbf{M}_{\mathbf{k} \neq 0}} \left(f_V[\mathbf{M}] + \mathbf{B} \cdot \mathbf{M}_0 - \frac{\mu_0}{2} \mathbf{M}_0 \cdot N_V \cdot \mathbf{M}_0 \right), \quad (2.8)$$

which, by construction, is independent of \mathbf{B} and N_V . e_α is simply the energy density excluding the Zeeman coupling to the external field and the homogeneous part of dipolar interaction, written as a function of \mathbf{M}_0 by minimizing over all remaining degrees of freedom of phase α . Under the given assumptions, we can then write the mean Gibbs free energy of the phase mixture as a function of the mixing parameter p and the individual values of the mean

magnetization per phase as

$$g(p, \mathbf{M}_{0,\alpha}, \mathbf{M}_{0,\beta}) = (1-p)(e_\alpha(\mathbf{M}_{0,\alpha}) - \mathbf{B} \cdot \mathbf{M}_{0,\alpha}) + p(e_\beta(\mathbf{M}_{0,\beta}) - \mathbf{B} \cdot \mathbf{M}_{0,\beta}) + \frac{\mu_0}{2} ((1-p)\mathbf{M}_{0,\alpha} + p\mathbf{M}_{0,\beta}) \cdot N_V \cdot ((1-p)\mathbf{M}_{0,\alpha} + p\mathbf{M}_{0,\beta}). \quad (2.9)$$

The equilibrium condition is now that g is minimal, subject to the condition $p \in [0, 1]$. In particular at the phase boundary between α and the mixed phase $\alpha + \beta$, this condition becomes

$$\left. \frac{\partial g}{\partial p} \right|_{p=0} \stackrel{!}{=} 0 \quad \Rightarrow \quad \begin{aligned} e_\alpha(\mathbf{M}_{0,\alpha}) - \mathbf{B} \cdot \mathbf{M}_{0,\alpha} + \mu_0 \mathbf{M}_{0,\alpha} \cdot N_V \cdot \mathbf{M}_{0,\alpha} \\ \stackrel{!}{=} e_\beta(\mathbf{M}_{0,\beta}) - \mathbf{B} \cdot \mathbf{M}_{0,\beta} + \mu_0 \mathbf{M}_{0,\beta} \cdot N_V \cdot \mathbf{M}_{0,\alpha}. \end{aligned} \quad (2.10)$$

Notice the interaction in the very last term. Instead of the critical field $\mathbf{B}_{c,\alpha}$, this can also be interpreted as a condition for the *internal* critical field of phase α , defined by $\mu_0 \mathbf{H}_{\alpha,c}^{\text{int}} = \mathbf{B}_{c,\alpha} - \mu_0 N_V \cdot \mathbf{M}_{0,\alpha}$. It then reads

$$\mu_0 \mathbf{H}_{\alpha,c}^{\text{int}} \cdot (\mathbf{M}_{0,\alpha} - \mathbf{M}_{0,\beta}) = e_\alpha(\mathbf{M}_{0,\alpha}) - e_\beta(\mathbf{M}_{0,\beta}), \quad (2.11)$$

which, importantly, is now independent of N_V . All dependence on the demagnetization tensor is contained in the relation between $\mathbf{H}_{\alpha,c}^{\text{int}}$ and $\mathbf{B}_{c,\alpha}$. Specifically for $N_z = 0$ and $\mathbf{M}_{0,\alpha} \parallel \hat{\mathbf{e}}_z$ (or alternatively, unphysically $N_V = 0$), $\mathbf{H}_{\alpha,c}^{\text{int}} = \mathbf{B}_{c,\alpha}$, and the condition reduces to one that is equivalent to what we have been doing previously when neglecting phase coexistence. Thus, we can infer the $\alpha \leftrightarrow \alpha + \beta \leftrightarrow \beta$ phase boundaries from the single boundary acquired from this special case via

$$\mathbf{B}_{c,\alpha} = \mu_0 \mathbf{H}_{\alpha,c}^{\text{int}} + \mu_0 N_V \cdot \mathbf{M}_{0,\alpha} = \mathbf{B}_c \Big|_{N_V=0} + \mu_0 N_V \cdot \mathbf{M}_{0,\alpha}. \quad (2.12)$$

In the case of $\mathbf{M}_0 \parallel \mathbf{B} \parallel \hat{\mathbf{e}}_z$, this takes the simple form $B_{c,\alpha,z} = B_{c,z} \Big|_{N_z=0} + \mu_0 N_z M_{0,\alpha}^z$. The resulting phase diagram as a function of N_z and B_z is shown in [figure 2.9c](#). The original phase transitions are broadened into wide areas of phase coexistence. Comparing these regions to the much larger areas of coexistence shown in [figures 2.6](#) and [2.9d](#) is, however, not particularly meaningful, as the latter are dominated by hysteresis effects, which we did not consider in our analysis.

We have now explored the effect of cubic anisotropy on the phase diagram of chiral magnets, with a particular focus on the two newly discovered phases in Cu_2OSeO_3 . One is a new skyrmion lattice phase, stabilized by anisotropy instead of thermal fluctuations and disconnected to the previously known phase pocket. The other is a tilted conical phase, which is only metastable, but is still realized in the experiments due to hysteresis effects. Further, we have identified the relevant parameters for the appearance of these phases, and have demonstrated that a comprehensive portrayal of a helimagnetic phase diagram should take phase coexistence into account.

2.3 SIGNATURES OF THE NEW PHASES

After mapping the phase diagram of chiral magnets subject to cubic anisotropy in the previous section, we will now examine the properties of the different phases in more detail. We will examine the one-dimensionally modulated states first, before turning to the skyrmion lattices.

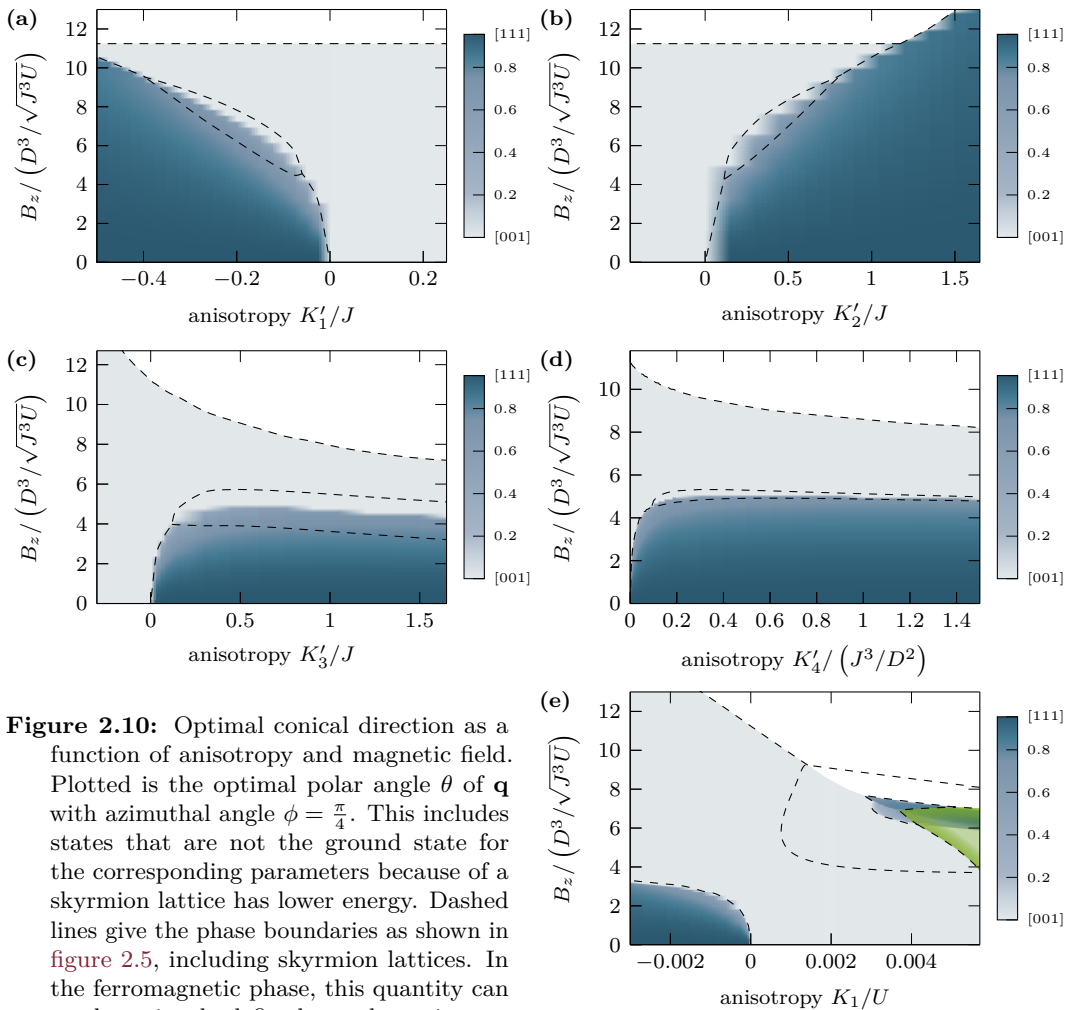


Figure 2.10: Optimal conical direction as a function of anisotropy and magnetic field. Plotted is the optimal polar angle θ of \mathbf{q} with azimuthal angle $\phi = \frac{\pi}{4}$. This includes states that are not the ground state for the corresponding parameters because of a skyrmion lattice has lower energy. Dashed lines give the phase boundaries as shown in figure 2.5, including skyrmion lattices. In the ferromagnetic phase, this quantity can not be uniquely defined, see the main text.

Accordingly, these areas are left blank. Parameters are as in figure 2.5, with all anisotropy parameters except one vanishing. (a–d) For all types of anisotropy involving gradients (primed prefactors), the phase with $\mathbf{q} \nparallel \hat{\mathbf{e}}_z$ is dominantly characterized by \mathbf{q} being approximately parallel to $(1, 1, 1)^T$, with some turning towards \mathbf{B} close to the sharp transition — these are the known helical phases. They all extend down to $\mathbf{B} = 0$. (e) For $K_1 < 0$ we find an analogous phase much like in (a–d). Only for $K_1 \gtrsim 0.0028U$ we observe a second (metastable) phase with $\mathbf{q} \nparallel \hat{\mathbf{e}}_z$ that only exists for finite \mathbf{B} . Usually it is obscured by the skyrmion lattice phase. For some parameters it also shows a sharp internal transition between states with different θ . In the partially transparent green area, the lowest-energy non-skyrmion state is a helical state with $\mathbf{q} \parallel \hat{\mathbf{e}}_x$. It is drawn transparently to show the θ -structure of the tilted phase underneath. The steps observed in some of the boundaries are due to limited resolution of the underlying data.

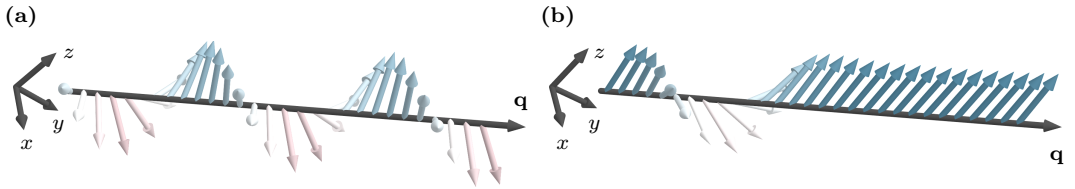


Figure 2.11: Real-space structure of exemplary conical states with $\mathbf{q} \parallel \mathbf{B}$. (a) The low- \mathbf{B} helical/conical phases that appear for any of the explored anisotropy types have a structure very close to an ordinary helix. They do have a slightly conical shape, though, and some further deformations too small to see in this plot. Shown here for $K_1' = 0.1 J$ and $\mathbf{B} = 4 D^3 / \sqrt{J^3 U} \hat{\mathbf{e}}_z$. The lower- \mathbf{B} -part of the metastable tilted conical phase (medium blue for $K_1 > 0$ in figure 2.10e) also has this type of structure. (b) The upper- \mathbf{B} -part of the metastable tilted conical phase (dark blue for $K_1 > 0$ in figure 2.10e) consists of single conical windings with polarized areas in between. Shown here for $K_1 = 0.004 U$ and $\mathbf{B} = 7 D^3 / \sqrt{J^3 U} \hat{\mathbf{e}}_z$.

We have yet to identify the nature of the helical/conical phases with $\mathbf{q} \parallel \mathbf{B}$ shown in figure 2.5. A first step towards a proper classification is to look at the direction of their respective propagation vectors \mathbf{q} . In figure 2.10, we plot the polar angle θ of \mathbf{q} of the lowest-energy non-skyrmion state for the same parameters as in figure 2.5. Since the polarized state is not modulated and therefore is not associated with a \mathbf{q} -vector, the corresponding areas are left blank. All five panels show a very similar picture for these phases. At $\mathbf{B} = 0$, we find $\mathbf{q} \parallel (1, 1, 1)^T$, immediately identifying these phases as the usual helical phases found in almost all chiral magnets. Upon increasing $\mathbf{B} \parallel \hat{\mathbf{e}}_z$, however, we see the optimal angle θ decreasing slightly, which corresponds to \mathbf{q} tilting away from $(1, 1, 1)^T$ and towards $\hat{\mathbf{e}}_z$, similar to previous results for the helical phase [59]. This is accompanied by the development of a small mean magnetization component parallel to \mathbf{q} , which is synonymous with the state becoming slightly conical, as shown in figure 2.11a. Close to the boundary to the regular conical phase or the skyrmion lattice phase, the polar angle θ decreases much more strongly, before falling to zero in a sharp transition.

The tilted conical phase, on the other hand, which exists metastably for $K_1 \gtrsim 0.0028 U$ and $\mathbf{B} \gtrsim 6 D^3 / \sqrt{J^3 U}$ (at least for $r_0 = -100 D^2 / J$), is very different, as is evident in figure 2.10e. Starting in the conical phase with $\mathbf{q} \parallel \mathbf{B}$ at $\mathbf{B} = 0$ and $K_1 \gtrsim 0.0028 U$, we increase the magnetic field. Since we disregard skyrmion lattices at the moment, taking only one-dimensionally modulated states into account, we stay in the conical phase until $\mathbf{B} \approx 6 D^3 / \sqrt{J^3 U}$. At that point, the optimal \mathbf{q} -direction jumps away from \mathbf{B} in a sharp transition to a value well away from both $\hat{\mathbf{e}}_z$ and $(1, 1, 1)^T$. Upon further increasing the magnetic field, for some parameter values, we actually find another sharp transition with \mathbf{q} tilting even further towards $(1, 1, 1)^T$, before the polarized state finally becomes the lowest-energy non-skyrmion state. The most striking difference between the tilted conical and the regular helical and conical phases, may, however, be its real-space structure in the area above this internal transition. The lower- \mathbf{B} tilted states, just as the previously discussed helical phases, are rather well described by the image of a continuously rotating helix with all spins tilted in \mathbf{q} -direction. The upper- \mathbf{B} tilted states, on the other hand, are better described as single such conical windings that have dissociated, with polarized areas in between, as shown in figure 2.11b. We find that the distance between these single windings decreases upon increasing the magnetic field towards

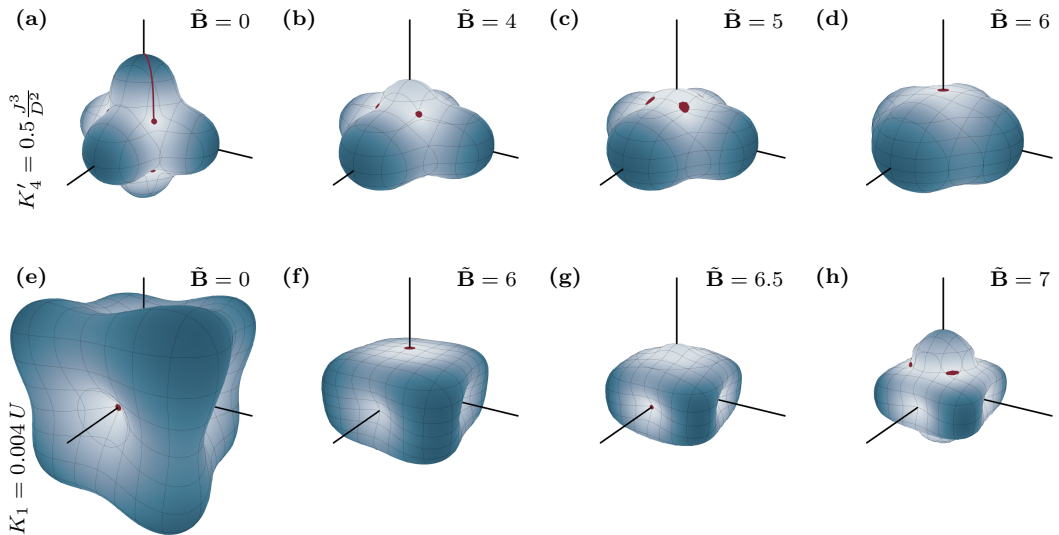


Figure 2.12: Energy surfaces for conical states with different anisotropy and magnetic field. For each direction of \mathbf{q} , the color and radius show the total energy. Radius is scaled per row to lie between $\frac{1}{2}$ and $\frac{3}{2}$, color is scaled per panel. The magnetic field $\mathbf{B} = \tilde{\mathbf{B}}D^3/\sqrt{J^3U}$ points up and changes per panel as given in the insets. Anisotropy changes per row and is given in the insets on the left. The red spots highlight the minima, the red line in panel (a) highlights the high symmetry line between $\hat{\mathbf{e}}_z$ and $(1, 1, 1)^T$. For a detailed discussion see the main text.

the polarized regime. This raises the interesting question whether this transition could be described as the melting or sublimation of a one-dimensional crystal of single conical windings. In this region, the tilted conical phase may also have a very different spin wave spectrum, since the individual windings are probably only weakly coupled. Unfortunately, these questions can not easily be answered with the method at hand, as it would likely require a much larger momentum-space cutoff.

Up to this point, we have not yet shown that the optimal \mathbf{q} -direction for the tilted phase actually lies on the high-symmetry line between $\hat{\mathbf{e}}_z$ and $(1, 1, 1)^T$. We can do this and at the same time gain a better understanding of the mechanism by examining the minimal energy of a one-dimensionally modulated state with fixed \mathbf{q} -direction for different directions and parameters. To visualize this energy function, we can plot it per set of parameters in the form of energy surfaces, like those in figure 2.1. There, we plotted for each direction of a constant magnetization the energy according to the respective cubic anisotropy contributions as the radius and color of a closed surface. Now, we will plot the total energy density of a helical/conical state for each direction of its \mathbf{q} vector in the same way. The result is shown in figure 2.12 for $K_1 = 0.004U$ and $K'_4 = 0.5 J^3/D^2$, respectively, and several magnetic fields. We have chosen $K'_4 = 0.5 J^3/D^2$ as a reference for the more intuitive and more commonly known helical to conical phase transition. The series with $K_1 = 0.004U$ then covers the path through the novel metastable helical and tilted conical phases. In each panel, the directions with minimal energy are marked by a red area, which is simply a sphere whose radius is slightly larger than the minimal energy. Specifically in panel (a), a red line marks the range

of directions on the high-symmetry line which we considered for the calculation of the phase diagrams.

First, we note that indeed, for the parameters shown here, the minimal-energy direction lies always either on the high-symmetry line, or in a $\langle 001 \rangle$ -direction. This was also the case for all parameters we have checked. Now, let us examine the evolution of the energy surface in the case where $K'_4 = 0.5 J^3 / D^2$, while scanning through the helical/conical phase, as shown in figures 2.12a to 2.12d. The K'_4 term is especially easy to understand, due to its simple structure $(k_x^4 + \dots) |\mathbf{M}_{\mathbf{k}}|^2$, where the entire anisotropy depends solely on \mathbf{q} . Changes in the structure of the state, meaning changes in $\mathbf{M}_{\mathbf{k}}$, only change the magnitude of the anisotropy, not which directions are preferred. At $\mathbf{B} = 0$, panel (a), the energy surface has cubic symmetry, which is not yet broken by \mathbf{B} . The $\langle 111 \rangle$ -directions have lowest energy and are thus preferred — we find a helical phase. With increasing magnetic field $\mathbf{B} \parallel \hat{\mathbf{e}}_z$, states with $\mathbf{q} \parallel \mathbf{B}$ and surrounding directions are lowered in energy, since they can more easily form a mean magnetization with large $\mathbf{M}_0 \cdot \mathbf{B}$ by becoming conical. Visually, this has the effect of flattening the energy surface, albeit non-uniformly, as shown in figures 2.12b to 2.12d. This in turn, has the effect of moving the minimum towards the z -direction — slowly at first and quickly towards the transition to the conical phase, which is reached in panel (d).

In the case where $K_1 = 0.004 U$, as shown in figures 2.12e to 2.12h, the situation is very different. At $\mathbf{B} = 0$, panel (e), we start in the conical phase with an energy surface that has its minima at the $\langle 001 \rangle$ -directions. With a magnetic field, the surface flattens, as before, but it also deforms. For the highest fields, shown in panels (g) and (h), the surface bulges *outward* on its top and bottom parts, instead of inward, as for lower fields. This can be understood by looking at the directions towards which the actual real-space magnetization points. In real space, the K_1 term is local and easier to understand. Figure 2.13 shows the bare anisotropy energy surface for directions of the magnetization with $K_1 > 0$, identical to that in figure 2.1f. It also depicts the magnetization of three simple conical states with different \mathbf{q} -directions and opening angles entered appropriately with a common origin. Each of the three states is represented by a different color. With a wide conical opening angle and $\mathbf{q} \parallel \hat{\mathbf{e}}_z$, as shown in green, the magnetization points mainly in low-energy directions. These are the conical states with $\mathbf{q} \parallel \mathbf{B}$

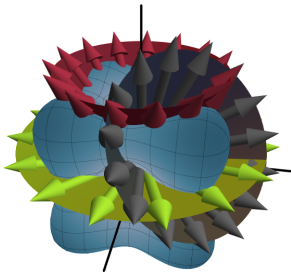
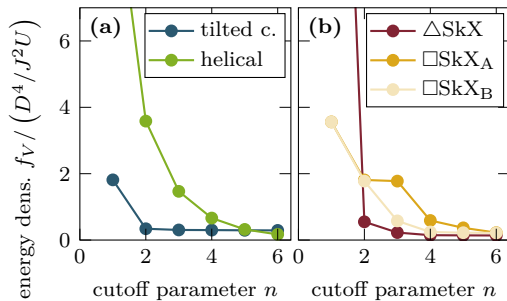


Figure 2.13: Anisotropy energy surface for the direction of the magnetization with the magnetization of three conical states. See main text for discussion.

at low fields. With increasing field the opening angle decreases. If then $\mathbf{q} \parallel (1, 1, 1)^T$, as shown in gray, the situation is similar. The tilted conical states are somewhat like this. If, however, $\mathbf{q} \parallel \mathbf{B}$ with an opening angle in the vicinity of $\frac{\pi}{4}$, as shown in red, the magnetization points mainly in high-energy directions. This is the effect causing the energy surfaces of figures 2.12g and 2.12h, which depict the total energy, to bulge outward at the top and bottom, and it is thereby mainly responsible for the appearance of the metastable tilted conical phase.

Interestingly, the energy surface shown in figure 2.12g is deformed so strongly, that the optimal \mathbf{q} -direction is perpendicular to the magnetic field. Thus, for these parameters, we draw a metastable helical phase as lowest-energy non-skyrmion state into the phase diagrams of figures 2.5e and 2.7. In figure 2.8, on the other hand, we do not find a helical phase at the corresponding position. The reason for that does not lie in the change of r_0 between the figures, but rather in the different momentum cutoff

Figure 2.14: Energy density as a function of the cutoff parameter n . (a) Helical and tilted conical ($\theta = \frac{1}{2}$, $\phi = \frac{\pi}{4}$) energy for $K_1 = 0.004U$ and $\mathbf{B} = 6.65 D^3/\sqrt{J^3U} \hat{\mathbf{e}}_z$. The anharmonic structure the helical state needs many \mathbf{q} -modes to be properly described. For these parameters it then has lower energy than the tilted conical state. (b) Energy of the three skyrmion lattices for $K_1 = 0.004U$ and $\mathbf{B} = 7 D^3/\sqrt{J^3U} \hat{\mathbf{e}}_z$. It is unclear which lattice has lowest energy for $n \rightarrow \infty$.



$n|\mathbf{q}|$. Figure 2.14a shows the energy of a helical state and a tilted conical state with $\theta = \frac{1}{2}$ and $\phi = \frac{\pi}{4}$ fixed as a function of the cutoff parameter n . For low n the tilted state has significantly lower energy, but above $n = 2$ it hardly changes. The energy of the helical state, on the other hand, continues to fall, until at $n = 6$ it lies below that of the tilted conical state. Evidently, the optimal helical state needs contributions of much higher \mathbf{q} -order to be properly described, compared with the tilted state. The reason for that becomes apparent by examining its real-space structure. Similar to the tilted conical state close to the boundary to the polarized state shown in figure 2.11b, the helical state consists of single helical windings with large polarized areas in between. Such structures many more significant Fourier components than the ordinary almost harmonic helical and conical states.

A similar complication also arises for the anisotropy-stabilized skyrmion lattices. Figure 2.14b shows the energy of the three different skyrmion lattice structures we consider as a function of the cutoff parameter n . For the parameters used in this plot, we find at $n = 1$ a significantly lower energy for the two square lattices. At $n = 2$, the situation is then reversed, and for high n all three states are very close to each other in energy. In fact, with the states so close in energy and not yet converged at $n = 6$, we can not with any certainty say which lattice structure will have lower energy in the limit $n \rightarrow \infty$. While this problem does not exist for all parameters (compare figure 2.5f), it is also not specific to K_1 . Generally, we find that with weak anisotropy and low fields the triangular lattice has lower energy, while for stronger anisotropy and higher fields, the situation is either reversed or unclear. The fact that the different lattice structures are so close in energy for a wide range of parameters actually fits rather well with the experiments. Remember that in neutron-scattering images, the newly found skyrmion lattice primarily appeared as a ring of intensity, as shown in figure 2.6e, due to disorder. Such disorder is exactly what should be expected from a crystallization process at low temperatures, where two or more different lattice structures are very close in energy.

In the previous section, we have explored how the phase diagram of the Ginzburg–Landau model for chiral magnets changes under the influence of cubic anisotropy, using extensive numerical minimization. Qualitatively, the results from taking one particular contribution into account match well with experiments on Cu_2OSeO_3 . We found the newly discovered tilted conical phase to be metastable, and found a new skyrmion lattice phase at low temperatures. In the present section we then examined the individual phases in more detail. Particular focus lay on the direction of \mathbf{q} in the helical and tilted conical phases. We also briefly discussed the role of the cutoff parameter n for the metastable helical phase and the structure of the skyrmion lattice. It would be interesting to explore this last point further, in order to

determine under which circumstances there might be structural transitions in the skyrmion lattice.

3

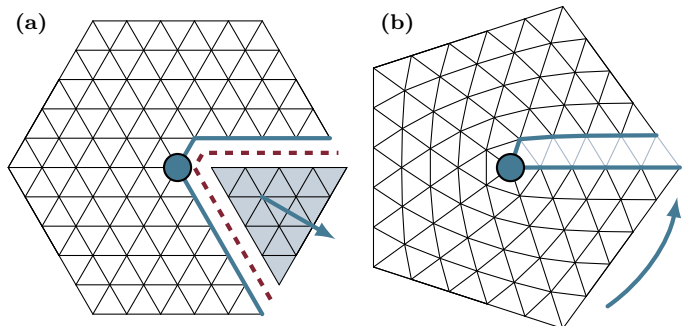
DEFECTS IN SKYRMION LATTICES

This chapter describes two projects, both of which turn out to depend on the physics of defects in skyrmion lattices. For this reason, we will start with a short introduction to lattice defects, focusing specifically on skyrmion lattices. In the following section, we will discuss the dynamics of a skyrmion lattice that is driven by the application of a radial heat current. Finally, the third section is about the melting transition of a skyrmion lattice. Both projects are related to experiments performed on Cu_2OSeO_3 .

3.1 LATTICE DEFECTS

Like other lattices, the skyrmion lattices found in chiral magnets are not always perfect. Just like atomic lattices, they can host lattice defects and undergo plastic deformation. Since introductions to lattice defects often focus on three-dimensional materials and use cubic lattices for illustration, we will have a very brief look at the specifics for skyrmion lattices. In particular, we will work in two not three dimensions, with triangular not square lattices, made from skyrmions not atoms.

Figure 3.1: Construction of a 5-disclination-defect. One way to construct a 5-defect (marked by the blue point) from a perfect triangular lattice is to (a) cut all bonds along the dashed line and remove the separated part of the lattice (shaded blue). Then (b) bend the whole lattice to close the resulting gap and creating new bonds where appropriate (light blue).



The ends of the blue lines, previously at an angle of $\frac{\pi}{3}$, are now approximately parallel.

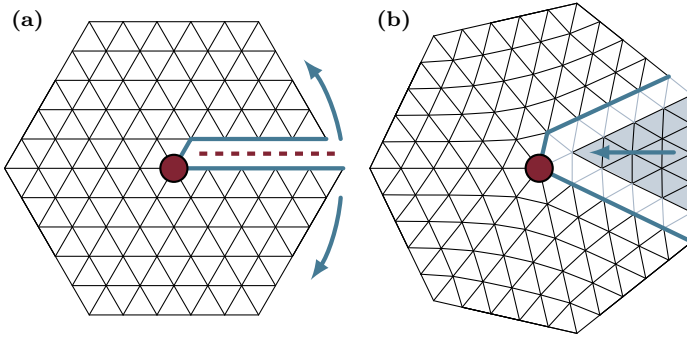


Figure 3.2: Construction of a 7-disclination-defect. One way to construct a 7-defect (marked by the red point) from a perfect triangular lattice is to (a) cut all bonds along the dashed line and bend the whole lattice to open a gap large enough to (b) insert a wedge-like additional crystal (shaded blue). Create new bonds where ap-

propriate (light blue). The ends of the blue lines, previously parallel, are now at an angle of about $\frac{2\pi}{7}$.

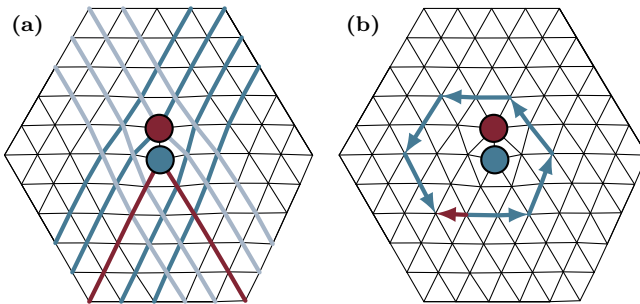


Figure 3.3: A 5-7-dislocation-defect and its Burgers vector. The combination of a 5- and 7-defect constitutes a dislocation. (a) Coloring individual lattice-lines light (dark) blue highlights the additional lattice-lines characteristic of dislocations (drawn in red). (b) The Burgers vector can be constructed by moving on bonds around the defect along a path

that would in a perfect lattice come back to the starting point. It is the vector connecting the start and end points of the path (shown in red). 20.0pt plus 6.0pt minus 6.0pt

Some types of defects present in atomic lattices, like impurity atoms, simply do not occur in skyrmion lattices. Others, like vacancies and interstitial type dislocation loops, do not seem to play a major role [LH1]. Furthermore, as skyrmion lattices are essentially two-dimensional (ignoring effects of skyrmion deformation and Bloch points), several types of defects which only exist in three-dimensional crystals, such as screw dislocations, do not occur either. Defects that do occur are disclinations and dislocations. Both types of defects can be characterized by the number of nearest neighbors the central skyrmions seem to have — their coordination number. This is how we will identify them later. In a defect-free triangular lattice each site has coordination number 6. A single skyrmion with coordination number 5 or 7 surrounded only by skyrmions with 6 neighbors each is called a 5-defect or 7-defect, respectively, and represents a disclination as illustrated in figures 3.1 and 3.2. The figures show how the lattice has to bend, when constructing a 5- or 7-defect from a perfect triangular lattice. The resulting change of the relative angles of lattice-lines is the defining characteristic of disclinations.

Combining a 5- and a 7-defect, the result is no longer a disclination, but a dislocation. Figure 3.3a shows the additional lattice-lines introduced by the dislocation in red. While there appear to be two such lines, carefully counting sites reveals that only one line was added — a consequence of the three lattice vectors of the triangular lattice being linearly dependent.

Dislocations have a topological invariant called the *Burgers vector*. It is defined as the vector connecting the start and end points of a path enclosing the defect, where the path is moving on bonds and is chosen such that it would be closed would it not circle the defect. Since the Burgers vector is a topological quantity, use of any such path enclosing the defect will result in the same vector, except for a sign which is given by the orientation of the path and can be fixed by convention — it is an axial vector [60]. Construction of the Burgers vector of a 5-7-defect is shown in figure 3.3b. An important observation on 5-7-defects can be made from the fact that the Burgers vector is topological in nature. A single such defect can only be created at the boundary of a lattice. In central regions, they can only be created in pairs or larger groups.

3.2 ROTATING A SKYRMION LATTICE

Soon after the first discovery of a skyrmion lattice in a chiral magnet, Mochizuki et al. set out to image such a skyrmion lattice in real space [23]. Using Lorentz transmission electron microscopy (LTEM), they not only managed to do so, but also observed a rotation of the skyrmion crystal. After ruling out other potential explanations, namely the electric current of the electron microscope and the magnetic field created by it, the authors concluded the rotation is caused by a small thermal gradient in the sample. This gradient is a direct consequence of the electron beam of the microscope locally irradiating the sample, causing equally localized heating. Consequently, an approximately radially symmetrical magnon current is generated, interacting with the skyrmion lattice. Importantly, magnons scatter off skyrmions asymmetrically in a process known as skew scattering [61] — see figure 3.4. For the magnons, this results in a topological magnon Hall effect, where a magnon current in the perpendicular direction — here: circular — is generated. So in a classical picture the magnons are deflected from a radial movement to spiral-like trajectories. For the skyrmions on the other hand, this results in a force driving them *towards* and to the *side* of the heat source. After cancellation of the radial component by repulsive inter-skyrmion interactions (see also below), the net effect is a force driving the skyrmions circularly. All this is illustrated in figure 3.5.

The effect observed in these experiments raises questions regarding the dynamics of skyrmion lattices under the influence of thermal gradients. While the forces required to depin a skyrmion lattice are weak, they do not vanish. Thus, it would be unreasonable to assume that the whole skyrmion crystal in a large sample rotates due to local heating without breaking up. So unless the samples used in the experiments were so small as to allow a rotation of the whole skyrmion lattice and the effect would vanish for larger samples, the rotational frequency must decrease with increasing distance from the heat source, most likely vanishing completely after some distance due to impurity pinning.

The mechanism behind this decrease in frequency is, however, unknown. One possible scenario might be that the frequency drops in discrete steps, with nested rigid concentric rings rotating at different speeds, separated by a layer of skyrmion liquid. To answer this question is one of the major aims of this section. Unfortunately, simulating this system micromagnetically is unfeasible, due to its large size. Instead we will model each skyrmion as a point-like particle, and compare our results to the experiments performed by Pöllath

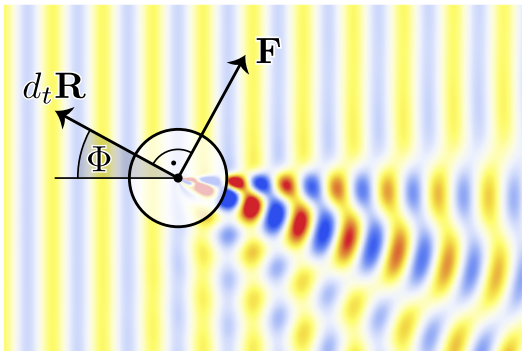


Figure 3.4: Magnon–skyrmion skew scattering. A magnon wave coming in from the left scatters asymmetrically off a skyrmion, exerting a force F on it. Due to its peculiar dynamics (see below), the skyrmion thus moves perpendicular to the force towards the origin of the incoming magnon wave at an angle Φ . Reproduced figure with permission from [61]. Copyright 2014 by The American Physical Society.

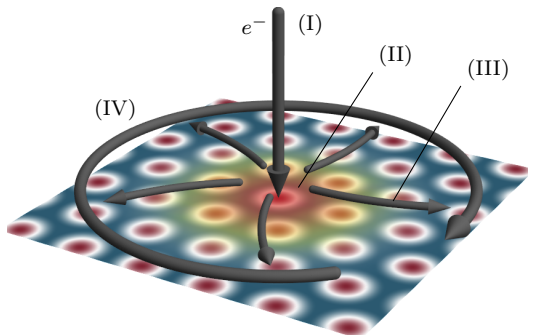


Figure 3.5: Skyrmion lattice rotated by an incoming electron beam. The electron beam (I) locally heats the sample, creating a temperature gradient (II). The resulting magnon flow (III) is deflected by skew scattering off the skyrmions. The counterforce causes the skyrmion lattice to rotate (IV).

et al. on Cu_2OSeO_3 [LH1]. While this introduces another layer of approximation, the method, often known as molecular dynamics simulation, has been applied successfully before [62, 63].

The motion of skyrmions can in a good approximation be described by the *Thiele equation* [64], named after Alfred A. Thiele who first derived a version of it to describe the motion of magnetic bubble domains [65]. Starting from the non-linear sigma model (1.6) in 2D, with the LLG equation (1.8), we assume that the magnetization is completely determined by specifying the set $\{\mathbf{R}_i\}$ of all skyrmion coordinates: $\mathbf{M}(\mathbf{r}) = \mathbf{M}(\{\mathbf{R}_i\})(\mathbf{r})$. We can then derive a version of the Thiele equation that takes the effects of the heat current-induced magnon flow into account [64, 61, 66]:

$$\mathbf{G} \times (\dot{\mathbf{R}}_i - \mathbf{v}(\mathbf{R}_i)) + \alpha D \dot{\mathbf{R}}_i - \beta D \mathbf{v}(\mathbf{R}_i) = \sum_j \mathbf{F}_{i,j}, \quad (3.1)$$

where $\mathbf{F}_{i,j}$ are forces from skyrmion–skyrmion interaction, $\mathbf{G} = -4\pi\hat{e}_z$ is the gyrocoupling vector, and α is the damping constant from the LLG equation. Here, we use a system of rescaled units, where $J = 1$, $D = 1$, $|\mathbf{M}| = 1$, $\gamma = 1$, lengths are given in units of J/D , and energies in units of J . From the micromagnetic simulation of a single skyrmion, we have determined the additional damping constant \mathcal{D} as

$$\mathcal{D}\delta_{i,j} = \int d^2r \frac{\partial \mathbf{M}}{\partial \mathbf{R}_i} \frac{\partial \mathbf{M}}{\partial \mathbf{R}_j} \approx 15.5 \delta_{i,j}. \quad (3.2)$$

The terms including the effective velocity \mathbf{v} model the influence of heat currents. Assuming a Gaussian profile $\sim e^{-(|\mathbf{r}|/r_0)^2/2}$ for the electron beam, and using that \mathbf{v} is proportional to the

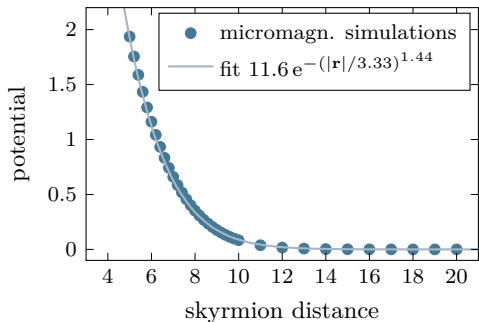


Figure 3.6: Skyrmion-skyrmion interaction potential in 2D. Extracted from four micromagnetic simulations per data point, as described in the main text. The fit is then used to calculate the repulsive forces between skyrmions in particle-based simulations.

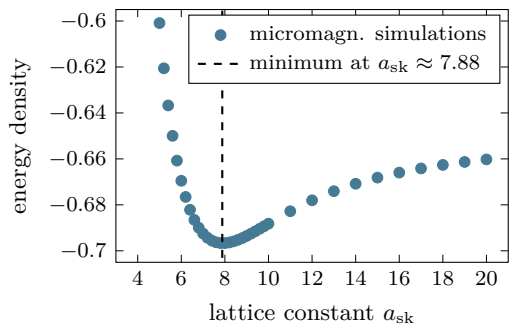


Figure 3.7: Energy density of a skyrmion lattice in 2D as a function of the lattice constant. The energy density shows a clear minimum, marking the equilibrium skyrmion distance.

heat current [66], we obtain

$$\mathbf{v}(\mathbf{r}) = -\frac{\mathbf{r}}{|\mathbf{r}|^2} v_0 \left(1 - e^{-(|\mathbf{r}|/r_0)^2/2} \right), \quad (3.3)$$

with the beam radius r_0 , and the base velocity v_0 , which will be our measure for the strength of the heat current. Note that \mathbf{v} points *towards* the heat source, reflecting the property of skyrmions to move in that direction [61, 66, 67]. Furthermore, β should be negative and much larger than α [66]. We use $\beta = -0.3$, but, for comparison, we have also performed simulations for $\beta = 0$, with qualitatively similar results.

Finally, we need to model the skyrmion-skyrmion interaction $\mathbf{F}_{i,j}$. To this end we calculate the energy of two skyrmions in the Heisenberg model, using micromagnetic simulations. In a large 2D simulation volume, we place two skyrmions at a distance \mathbf{r} to each other, within a polarized background. While holding them in place by fixing each central spin, we calculate the minimal energy for a magnetic field of $\mathbf{B} = 0.65 \hat{\mathbf{e}}_z$ in our units. To extract the potential, we subtract the energy of the polarized background, and the energy of each skyrmion relative to the background, which we obtain by a total of three additional simulations. The result is shown in figure 3.6 as a function of skyrmion distance \mathbf{r} . Evidently, $V(\mathbf{r}) \approx 11.6 e^{-(|\mathbf{r}|/3.33)^{1.44}}$ is a good fit to the data, resulting in the force $\mathbf{F}_{i,j} = -(\nabla V)(\mathbf{R}_j - \mathbf{R}_i)$. To model screening of interactions and to avoid the computationally costly calculation of the distances between all pairs of skyrmions, we cut off $\mathbf{F}_{i,j}$ using a hard cutoff at a distance of $\mathbf{R}_j - \mathbf{R}_i = 12$.

Unfortunately, even with this much simplified particle setup, we still cannot simulate on the experimentally relevant timescale of tens of seconds, since the microscopic timescale is about ten orders of magnitude smaller [52]. By applying current densities much larger than those in the experiments, we can, however, still qualitatively reproduce the dynamics observed in the experiments. For the simulations shown here we choose a current strength of $v_0 \in [0, 0.045]$, with a beam radius of $r_0 \approx 226$, and damping of $\alpha = 0.05$. With another set of micromagnetic

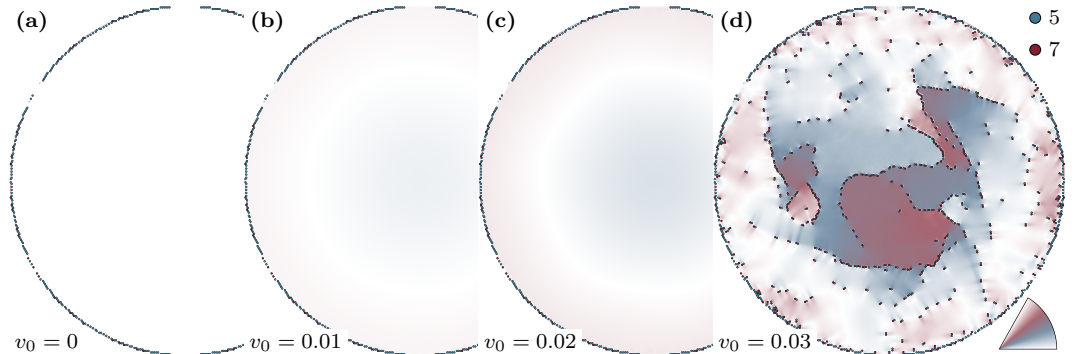


Figure 3.8: Lattice deformation and breaking as a function of heat current $\sim v_0$. Most individual skyrmions are not shown. The color corresponds to the local lattice orientation, as indicated by the inset in the bottom right corner. 5-defects (7-defects) are marked by blue (red) points. The outward heat current exerts a torque on the skyrmion lattice. For comparatively weak heat currents the lattice stays mostly intact, merely being deformed, and reaches a stationary state (a–c). Upon increasing the heat current, the deformation increases until at some critical strength lattice defects begin to form, enabling the lattice to form rotating domains in the center, never to reach a stationary state (d). See also [figure 3.9](#).

simulations, similar to before and with identical parameters, we calculate the energy density of a skyrmion lattice as a function of the lattice constant a_{sk} (i.e. the skyrmion distance at equilibrium). As shown in [figure 3.7](#), it is approximately $a_{\text{sk}} \approx 7.88$ in our units.

We initialize an undisturbed triangular lattice of skyrmions at the equilibrium distance on a disk with a radius of $100 a_{\text{sk}}$. Translated to the experimental values for Cu_2OSeO_3 , the disk has a radius of approximately $15 \mu\text{m}$. Since the particle based model that we use does not contain information on the energy of skyrmions relative to the background, which would determine the equilibrium distance, we fix the position of the outermost skyrmions. This has the added benefit of simulating a pinned lattice at large distances, thereby preventing the lattice from rotating as a whole, which might otherwise be a problem, since the model does not contain any pinning holding skyrmions in place either. For this setup, we solve the initial value problem of the [Thiele equation of motion \(3.1\)](#) by a straightforward application of the standard 4th order Runge-Kutta method.

To analyze the results, we first perform a Delaunay triangulation on the set of skyrmion coordinates, thereby identifying a lattice structure. For any triangulation of a set of points in two dimensions, a set of lines between these points must be found, such that no two lines cross, thus forming a set of triangles with the given points as corners. In order for it to be a Delaunay triangulation, none of the given points may lie inside the circumcircle of any of these triangles. In the resulting lattice, most skyrmions still have six nearest neighbors, as in the unperturbed triangular lattice. For these skyrmions we can define the local lattice orientation as $\varphi_i = \frac{1}{6} \sum_j \varphi_{i,j}$, where the sum runs over nearest neighbors, and $\varphi_{i,j} \in [-\pi, \pi]$ is the angle between $\mathbf{R}_j - \mathbf{R}_i$ and the x -Axis. φ_i is closely related to the orientational order parameter Ψ_6 . Importantly, however, some skyrmions have a different number of nearest neighbors — typically five or seven — representing lattice defects, where each individual 5-

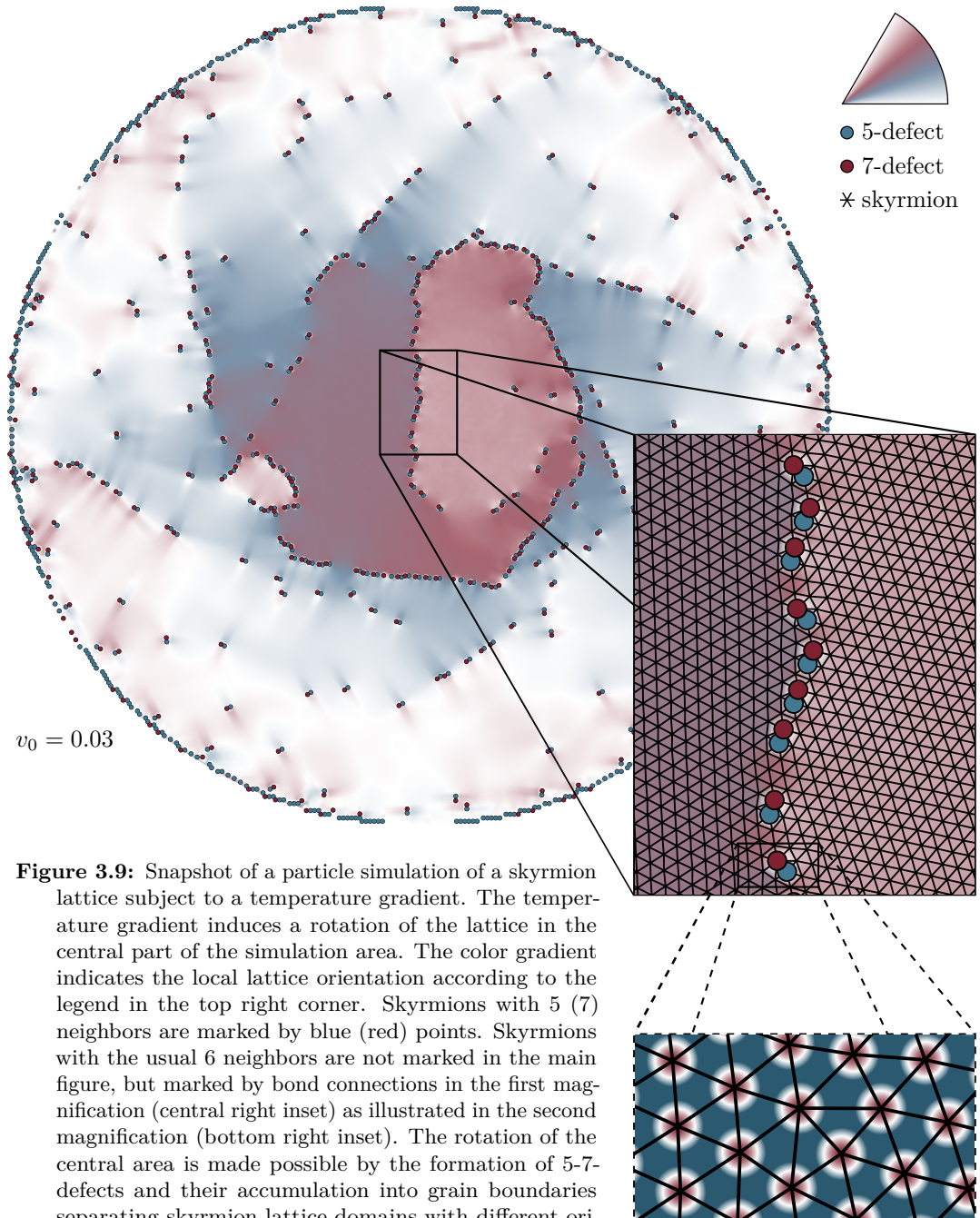


Figure 3.9: Snapshot of a particle simulation of a skyrmion lattice subject to a temperature gradient. The temperature gradient induces a rotation of the lattice in the central part of the simulation area. The color gradient indicates the local lattice orientation according to the legend in the top right corner. Skyrmions with 5 (7) neighbors are marked by blue (red) points. Skyrmions with the usual 6 neighbors are not marked in the main figure, but marked by bond connections in the first magnification (central right inset) as illustrated in the second magnification (bottom right inset). The rotation of the central area is made possible by the formation of 5-7-defects and their accumulation into grain boundaries separating skyrmion lattice domains with different orientations. Adapted figure with permission from [LH1]. Original copyright 2017 by The American Physical Society.

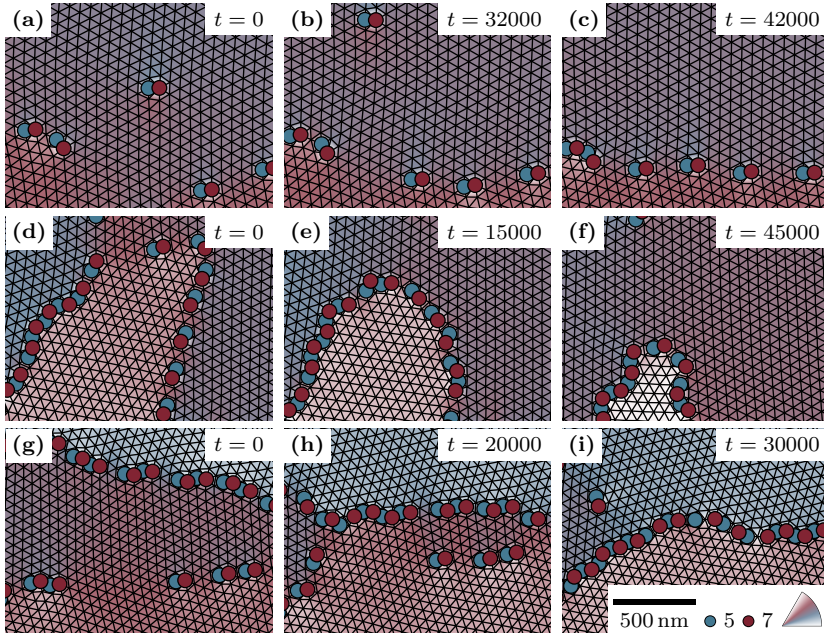


Figure 3.10: Time series showing three of the processes governing the dynamics of the rotating skyrmion lattice. For a discussion of the processes see the main text. For a description of the visualization see the previous figures. The scale bar shows the scale of all panels as calculated for the experimental parameters of Cu_2OSeO_3 . Adapted figure with permission from [LH1]. Original copyright 2017 by The American Physical Society.

or 7-defect is a disclination and the combined 5-7-defect is a dislocation, as discussed in section 3.1.

Figures 3.8 and 3.9 show snapshots of particle-based simulations, analyzed as described, where the color gives the local lattice orientation, and 5-defects (7-defects) are marked by blue (red) points. As visualized in figures 3.8a to 3.8c, for weak heat current the skyrmion lattice stays intact despite the torque exerted by the heat current. It is merely being deformed, as visible by the blue disk in the center (rotated counter clockwise) surrounded by a red ring (rotated clockwise). The deformation increases with increasing heat current, visible in the slightly increasing saturation of colors between figures 3.8b and 3.8c. At some critical strength, which for the given parameters corresponds to a critical base velocity v_0 between 0.02 and 0.025, 5-7-defects begin to form, as is visible in figures 3.8d and 3.9. The latter shows a snapshot of the same simulation as the former, but at an earlier time and in more detail. The defects mostly form at the boundary as single 5-7-defects, but also in other areas as pairs of 5-7-defects with opposite Burgers vector. These dislocations move through the sample, reducing strain in the process. Where previously the skyrmion crystal deformed elastically, it now undergoes plastic deformation. By arranging into lines, they begin forming domain walls, separating skyrmion lattice domains with different orientation. As more 5-7-defects accumulate on a domain wall, the angle difference between the adjacent domains increases

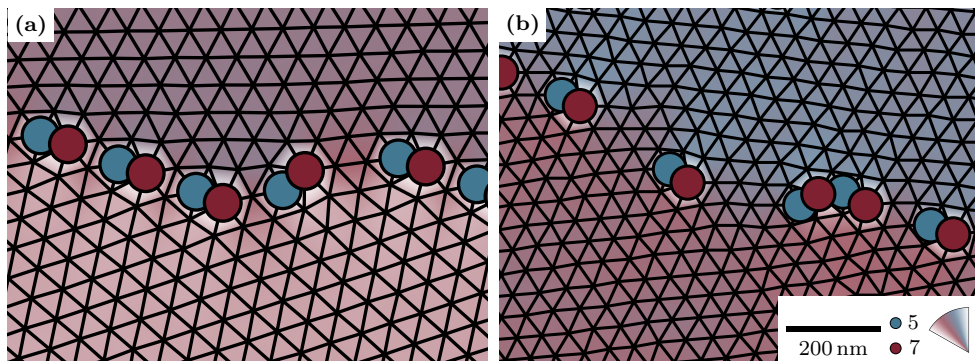


Figure 3.11: Skyrmion lattice domain wall in simulation and experiment. (a) Magnification of [figure 3.9](#). (b) LTEM image of a thin film of Cu_2OSeO_3 by Pöllath et al. [[LH1](#)], processed as described in the supplementary material of the reference and analyzed as described in the main text here. The scale bar is accurate for panel (b) and panel (a) is scaled to match, according to our calculations for the experimental parameters.

in accordance with Frank’s formula [[LH1](#)]. As the angle difference passes 30° , which is the maximal relative angle between two triangular lattices, defects recombine, effectively decreasing the number of defects again.

Such processes allow domains in the central area of the simulations to rotate and never reach a stationary state. They also give the system surprisingly rich dynamics, some of which is illustrated in [figure 3.10](#). Panels (a–c) show the formation of a domain wall by the accumulation of 5-7-defects, as already discussed. Panels (d–f) show a domain shrinking in favor of another, by a recombination of the 5-7-defects involved in the domain wall. Meanwhile, the whole lattice in the visible area is rotating, as is indicated by the slight change in color. Panels (g–i) show two domain walls combining into one, thereby destroying the central domain. Through processes like these, the domain-structure of the lattice is constantly changing, with new domains being formed, while others are destroyed.

[Figure 3.11](#) shows a comparison between a magnification of [figure 3.9](#) and an experimental LTEM image analyzed in the same way (after some image processing and skyrmion detection [[LH1](#)]). Both images show a single domain wall with the same structure: an alignment of 5-7-defects such that 5- and 7-defects alternate, with domains of different orientation on either side. The fact that the simulated lattice is more regular is most likely due to the fact that the simulations are done for $T = 0$, opposed to low but finite experimental temperatures. Interestingly, the lattice parameter a_{sk} does not match between the two images. This might either also stem from temperature effects, it might stem from imperfect parameter scaling, or it might be due to problems with the simulations which we used to calculate a_{sk} , for example the approximation of the thin film as a strictly two-dimensional material. Not visible in [figure 3.11](#), but in the supplementary movie by Pöllath et al. [[LH1](#)], is how in the experiment 5-7-defects seem to appear and disappear at random. The experiment simply does not have sufficient time resolution to capture the dynamics of the defects. With our simulations we can close this gap and observe the full dynamics of the defects.

With a moderate heat current, isolated 5- and 7-defects appear only rarely in the simulations. They almost exclusively appear as bound pairs, forming a 5-7-defect. With even stronger heat current, however, 5- and 7-defects increasingly start to dissociate, which mostly happens by a recombination of multiple 5-7-defects. It might be tempting to call this regime, which features rapidly decaying correlations, a skyrmion liquid. It is even preceded by the regime featuring rotating domains with reduced but prevalent correlations, which one might call a hexatic phase. These are, however, states far from equilibrium, and should not be confused with thermal states. Therefore, we discourage this nomenclature and refer to the following section instead, where such phases are discussed.

Even though we are unable to reach the parameter regime of the experiments, our simulations nicely reproduce the experimental results and reveal details not accessible in the experiments. In particular, we found that the mechanism behind the rotation of skyrmion lattice domains under the influence of radial heat currents is based on 5-7-defects moving through the lattice and forming domain walls. At present it is unclear how our results relate to other systems with densely packed 2D lattices such as colloids, with Newtonian dynamics in contrast to the gyrocoupling-dominated Thiele dynamics of the skyrmions. While the difference is clearly significant for excitations of the lattice, where also the internal degrees of freedom of the skyrmion are crucial [52], it is unclear if the same holds true for the effective dynamics of the lattice defects.

3.3 MELTING A SKYRMION LATTICE

In thin slabs of chiral magnets the skyrmion lattice phase may extend down to lowest temperatures [68, 18]. New experiments on a thin slab of Cu_2OSeO_3 by Huang et al. now demonstrated that, in contrast to previous theoretical results [69], upon increasing the magnetic field this system does not transition from the skyrmion lattice to the ferromagnetic phase in a single first order transition. Instead, the system undergoes a series of phase transitions from the skyrmion lattice through a hexatic skyrmion phase to a skyrmion liquid phase before transitioning to the ferromagnetic phase [LH5].

The Kosterlitz–Thouless–Halperin–Nelson–Young (KTHNY) theory for melting in two dimensions predicts exactly such a pair of transitions, from solid to hexatic to liquid. Years before its development, Peierls and Landau [70, 71] noted that true long range order can not generally exist in one or two dimensions, which is a consequence of the Mermin-Wagner theorem as we now know [72]. Mermin, however, found that in two dimensions it is not replaced by a disordered state with exponentially decaying correlations. Instead, two-dimensional solids are characterized by power-law decay of translational correlations, in what is now called quasi-long range order. They also show true long range orientational order, with the corresponding correlations converging to non-vanishing constants. In their seminal work, Kosterlitz and Thouless then predicted that such a 2D crystal might melt by a dissociation of topological defects [73]. Young [74] and Nelson and Halperin [75] refined their results, finding that, under certain conditions, a 2D crystal would indeed melt by a dissociation of dislocations, but not into an isotropic fluid with exponential decay of all correlations. Instead, they found a so-called hexatic phase with exponential decay of translational correlations and either long range, or quasi-long range orientational order, depending on the substrate. This phase would then transition into a typical liquid with exponentially decaying correlations via

the dissociation of disclinations. It is important to note, that the series of transitions predicted by KTHNY theory does depend on some assumptions (mainly on the particle interaction), and alternative scenarios exist. One such alternative was predicted by Kleinert [76]. For a more detailed review see for example the article by Gasser et al. [77].

KTHNY theory can be described as a theory of thermodynamic plasticity. It is based on the linearized theory of continuous elastic media, which can be found in many textbooks, e. g. one by Landau and Lifshitz [78]. It is important to keep in mind, though, that most books only treat the three-dimensional case, often without indication, where results subtly differ from the two-dimensional case. Also, the various definitions of strain should not be confused. For uniaxial strain, for example, the deformation in the perpendicular direction might be fixed to vanish or be free to minimize the energy. To arrive at a theory of plasticity, the elasticity theory is modified by allowing for the existence of lattice defects, which interact with each other via elastic deformations [73]. Finally, in the vicinity of the phase transitions, the variables pertaining lattice defects can be integrated out, using a renormalization group (RG) scheme with the defect core size as the RG parameter. It serves as a cutoff determining beyond which distance from the defect continuum elasticity theory can be applied. The elastic constants, thus renormalized, tend towards fixpoints corresponding to the different phases in question. Consequently, the phase boundary can be characterized by the separatrix of the RG flow. The result most relevant for us here is one for the crystal–hexatic phase boundary. There, the critical effective value of Young’s modulus, which is a measure of the crystals stiffness against uniaxial strain, is predicted to be universal. In particular, it is predicted to be 16π in units of $k_B T$ divided by the square of the lattice spacing of the underlying lattice. This gives a convenient method of detecting the crystal–hexatic phase transition, see [79] for a usage example.

To calculate Young’s modulus in the zero temperature limit, we use micromagnetic simulations of a slightly strained skyrmion lattice. In contrast to the previous section, we simulate in three dimensions, to take surface effects into account, and increase the accuracy of our results. Since the skyrmion lattice is triangular, we use an enlarged unit cell, containing two skyrmions, which is compatible with the employed implementation based on cuboid discretization cells [39, 80]. By using simulation cells of different in-plane length and width with periodic boundary conditions, we can calculate the energy area-density of the lattice under both uniaxial and biaxial strain. In the absence of shearing, we can write the elastic energy area-density in one unit cell of the skyrmion lattice to lowest order in the deformation as

$$e_{\text{elastic}}(l_x, l_y) = e_{\text{eq}} + \frac{1}{2} \left(2\mu (\tilde{l}_x^2 + \tilde{l}_y^2) + \lambda (\tilde{l}_x + \tilde{l}_y)^2 \right) + \mathcal{O}(\tilde{l}_x^3, \tilde{l}_y^3), \quad (3.4)$$

where $\tilde{l}_i = (l_i - l_{i,\text{eq}}) / l_{i,\text{eq}}$ is the relative change of the length l_i of the unit cell in i -direction away from its equilibrium value $l_{i,\text{eq}}$, e_{eq} is the energy area-density of the undeformed lattice, and μ and λ are the so-called Lamé coefficients. Any non-zero value of either \tilde{l}_i constitutes a deformation, which costs energy approximately proportional to some combination of μ and λ . When thinking about the lattice deformation in terms of a toy model built from balls and springs, μ , λ , and Y are directly related to the spring constants. Note that for a system of spins, the relevant thermodynamic potential, i. e. the one which thermodynamics minimizes, is the magnetic Gibbs free energy of the spins [81], not, say, the energy per skyrmion. Consequently, at $T = 0$, the relevant quantity for the elasticity of the skyrmion lattice is the energy area-density and not the energy of a unit cell. This is in contrast to a

system of atoms without external pressure, where the Helmholtz free energy of the atoms, and thereby the energy per unit cell, is minimized. Fitting equation (3.4) to the energy of the strained skyrmion lattice obtained by our simulations, we can calculate μ and λ as a function of the external parameters — the applied magnetic field \mathbf{B} in particular.

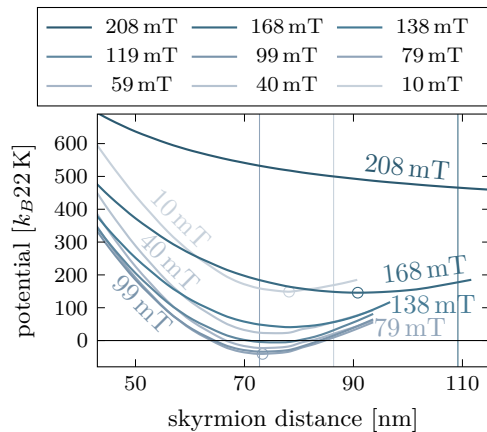
Results by Kang et al. for a strictly two-dimensional skyrmion lattice suggest that the relations between different elastic constants derived from continuum elasticity theory hold approximately [82]. By assuming they also hold for a three-dimensional skyrmion lattice, we can calculate Young’s modulus as $Y = 4\mu \frac{\mu+\lambda}{2\mu+\lambda}$. To compare with experimental results and KTHNY theory, we furthermore have to assume that Y at low but non-zero temperatures does not differ to much from its value at $T = 0$. When doing this, and simply inserting $Y|_{T=0}$ for the experimental values of $T = 22$ K and $|\mathbf{B}| \approx 98$ mT [LH5], we find, however, a value almost two orders of magnitude larger than the expected critical value of 16π . This is directly related to the thickness of the sample. For skyrmion lattices, it turns out, Young’s modulus Y scales linearly with the sample thickness. It is also important to note that with this procedure we calculated the bare value of Young’s modulus and only the renormalized value is expected to be 16π . Since the experiments clearly demonstrate the two-step melting process via dissociation of dislocations and disclinations predicted by KTHNY theory [LH5], we conclude that our analysis overestimates the stiffness of the skyrmion lattice significantly. There are multiple possible sources for this discrepancy. First, there is the already mentioned renormalization by thermal fluctuations, i.e. using $Y|_{T=0}$ at finite temperature, and dislocations. Second, there is considerable numerical inaccuracy in our results, although it seems unlikely, that this would consistently overestimate the stiffness by two orders of magnitude. Lastly and maybe most importantly, this discrepancy might simply be due to weak effects not included in our analysis, if they drive the system close to a structural transition of the skyrmion lattice. For example, surface effects or magnetocrystalline anisotropy could have such an effect, with the latter being a particularly likely candidate, see figures 2.6 and 2.14b and the surrounding text. Note that both sets of experiments were done on Cu_2OSeO_3 .

While we did not manage to quantitatively reproduce the experimentally observed transition, we see qualitative agreement when calculating an effective skyrmion–skyrmion interaction. In the previous section, we calculated an interaction potential between strictly two-dimensional skyrmions in a polarized background. In the more precise three-dimensional setup considered here, however, this is not possible, simply because the polarized background is unstable against the formation of a conical state for the relevant parameters. Additionally, in a conical background the interaction gains a directional dependence due to the surface-magnetization of the conical state, and the magnetic configurations involved differ significantly from those in the skyrmion lattice. Instead, we perform the same sort of simulations of a skyrmion lattice we used to calculate Young’s modulus. However, instead of independently straining in both directions, we strain the lattice uniformly in the plane, such that the in-plane aspect ratio of the unit cell is conserved, and the relative change of l_x and l_y is equal. From the energy of the system under this deformation, we can easily compute an effective interaction potential by comparing it to a lattice of point-like particles on a triangular lattice with pairwise nearest neighbor interaction. Its energy per unit cell can be written as

$$E_{\text{uc}}(l_x) = 3V(l_x) + E_{\text{bg}}(l_x), \quad (3.5)$$

with a pair potential $V(|\mathbf{r}|)$ on three bonds per unit cell. Each particle has six neighbors with each bond contributing to two unit cells, giving the factor 3 for one unit cell. We included a

Figure 3.12: Effective skyrmion–skyrmion potential for different magnetic fields. The potential was calculated by deforming a 3D skyrmion lattice, as described in the main text. For 10 mT, 79 mT and 168 mT the minimum of the potential is highlighted by a small circle. A vertical line marks the corresponding equilibrium distance, which includes the energy of the skyrmions relative to the background. Potentials are given in units of $k_B T$ with the experimental temperature $T = 22$ K, to allow estimating the impact of thermal fluctuations. The skyrmion lattice is the ground state for all fields where the minimum of the potential is negative. For large magnetic fields, the potential becomes increasingly flat, softening the lattice. Each plot stops approximately where the skyrmion lattice becomes structurally unstable. Redrawn from a similar figure in [LH5].



background energy $E_{\text{bg}}(l_x) \propto l_x l_y$ proportional to the unit cell area to account for the fact that in the magnetic system it is the energy *density*, that is minimized. Consequently, the equilibrium particle distance $l_{x,\text{eq}}$ might not be at the minimum of the potential. In the particle picture, this corresponds to the application of external pressure. For the skyrmion lattice, there is simply no reason to assume otherwise.

Using equation (3.5) as the definition of an effective potential, and remembering that we use an enlarged unit cell including two skyrmions, we first subtract the energy of the state with lowest energy that does not contain any skyrmions, which is a conical state for the relevant parameters. That way we obtain the results shown in figure 3.12, where the potential is given in units of $k_B 22$ K. That way we obtain the results shown in figure 3.12, where we plot the effective skyrmion–skyrmion potential as a function of their distance for different magnetic fields. To allow estimating the impact of thermal fluctuations at the experimental temperature of $T = 22$ K, the potential is given in units of $k_B 22$ K. By construction, parameters for which the potential is negative correspond to the skyrmion lattice being the ground state. More importantly, the potential becomes increasingly flat with increasing magnetic field, until it becomes fully repulsive when the background state becomes polarized. With the flattening potential, we expect the lattice to become softer and the elastic moduli to fall, which is required for the transition into the hexatic phase. In that sense, our results qualitatively agree with the experiments, even though we could not quantitatively demonstrate the transition to the hexatic phase.

Comparing figures 3.12 and 3.6, it is interesting to note that the effective potential derived here from a three-dimensional skyrmion lattice differs significantly from the potential calculated for two-dimensional skyrmions in a polarized background. The former has a pronounced minimum for all but the strongest magnetic fields, while the latter is fully repulsive. We can conclude, that the approach used in the previous section is likely oversimplified. It would be interesting to compute the elastic moduli resulting from both potentials, and compare them

to more direct calculations as those we describe above. A natural next step to improve our calculations would be to include anisotropy. In [chapter 2](#) we have seen that cubic crystal anisotropy drives the skyrmion lattice towards a structural transition which will likely be accompanied by a softening of the lattice, i. e. a reduction of Y and other elastic moduli. Since the experiments were done on thin slabs, uniaxial anisotropy might additionally also play a role.

4

DRIVING THE CONICAL STATE BEYOND THE LINEAR REGIME

In this chapter, we will discuss the driving of the conical state of chiral magnets by microwave fields. We start with a brief overview of the existing literature, the theoretical part of which is based on linear response theory. Following that, we will discuss micromagnetic simulations of a conical state driven by an oscillating magnetic field, where we will focus on effects beyond the linear response.

4.1 LINEAR RESPONSE

In recent years, there has been increasing interest in new kinds of devices, called spintronic devices for their use of spins instead of electrons for carrying and processing information. Chiral magnets are a class of good candidate materials for such devices. They are particularly interesting for their non-reciprocal properties, and their very efficient generation of spin transfer torques [24]. To be able to design spintronic devices from them, however, we need to understand their magnetic properties in greatest-possible detail—especially their spin wave spectra.

Possibly the most important contribution towards this end on the theoretical side has been made by Waizner et al. in a series of articles with different collaborators [52, 83–86]. Schwarze et al. [52] present a comprehensive theory for spin waves in a variety of chiral magnets that agrees very well with experiments on a variety of metallic, semiconducting and insulating chiral magnets. It is based on linear response theory and depends only on few parameters, all directly or indirectly accessible experimentally. Using the same basic Ginzburg-Landau theory discussed in section 1.2, and used in equation (1.13) and chapter 2, it additionally takes dipolar interaction and one kind of cubic anisotropy into account.

The principle of a (linear) spin wave calculation, such as those by Schwarze et al., is generally as follows. For a set of parameters, the ground state is first identified by minimizing the energy. Then, the equation of motion for the spins (the LLG equation (1.8) with or without damping) is expanded to linear order in the deviation from this state. Finally, the resulting equation of

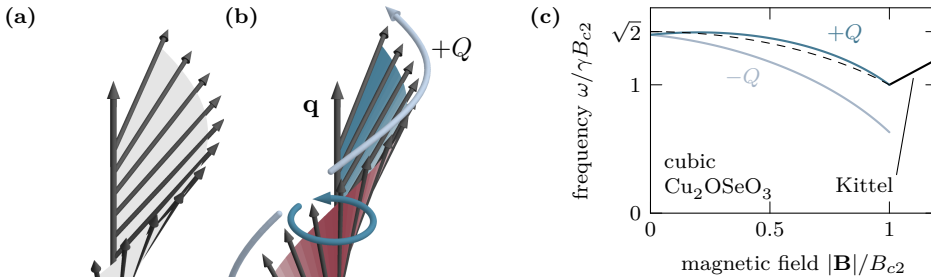


Figure 4.1: Spin wave excitation modes of the conical state at $\mathbf{k} = 0$. (a) Conical state in equilibrium. (b) In the excited conical state each spin precesses (dark blue arrow). The collective motion corresponds to spin compression waves with neighboring spins more (blue) or less (red) aligned than in the equilibrium state. These waves travel (light blue arrows) parallel ($+Q$) or antiparallel ($-Q$) to \mathbf{q} . (c) Magnetic field dependence of the $\pm Q$ modes (dark/light blue) and the ferromagnetic Kittel mode (black), calculated for a cube of Cu_2OSeO_3 . Without dipolar interaction the $\pm Q$ modes become degenerate and universal (dashed line).

motion is solved by Fourier transforming. Using a numerical implementation of this scheme, the authors are able to reliably predict the homogeneous ($\mathbf{k} \ll 1/\text{system size}$) excitation modes of the helimagnetic and ferromagnetic phases. Kugler et al. [83] and Stasinopoulos et al. [84] even successfully calculated and measured the full $\mathbf{k} \gg 1/\text{system size}$ magnon spectrum of the helical phase, the ellipticity and other details, using the same method. For a detailed review see the article by Garst et al. [85].

For the polarized, helical and conical phases specifically, the spectrum is even mostly understood analytically [52, 85, 86]. For $\mathbf{k} = 0$, the result is a generalization of the so-called Kittel mode in the ferromagnetic case [87, 88], and two modes in the conical case, dubbed $\pm Q$ mode. Figure 4.1c shows the magnetic field dependence of the three modes, and it is the latter two that we will focus on in the rest of this chapter. The motion of a single spin in any of these modes is usually a simple precession, the direction of which is determined by the sign of the gyromagnetic ratio γ of the material. Collectively, however, the mode can be much more complicated, as described by the LLG equation (1.8). In the case of the $+Q$ and $-Q$ modes, the collective motion can be described as spin compression waves that travel parallel ($+Q$) or antiparallel ($-Q$) to the propagation vector \mathbf{q} of the conical state, which is the origin of their name. This motion is illustrated in figures 4.1a and 4.1b. Note that with this naming convention, the relationship between the names and frequencies of these two modes is not fixed and can be reversed, depending on the signs of γ and D , the DMI strength, even though the spectrum is unaffected. The change of direction of the precession is, of course, also present in the Kittel mode of the polarized phase. At the phase boundary, the higher-frequency mode ($+Q$ in figure 4.1c) connects continuously to the Kittel mode. This is not only in terms of frequency, but also in the collective sense, as the conical angle

becomes smaller and smaller upon increasing the magnetic field, continuously transitioning to the polarized state.

4.2 BEYOND LINEAR RESPONSE

As Schwarze et al. have shown, results from linear spin wave theory agree nicely with experiments on chiral magnets. The non-linear character of the **LLG equation (1.8)** should, however, not be dismissed completely, since it might have effects relevant for applications—either as corrections to the results of the linearized theory, or by opening up completely new applications. The straight-forward way to improve upon the existing results would be to expand the LLG equation to higher order, and solve the resulting equations. This is tedious, at the very least, to do analytical.

Here we will use a complementary approach instead. We will solve the full LLG equation, including damping, numerically in micromagnetic simulations with an explicit oscillating magnetic field driving the system [39, 80]. The obvious benefit is that we get the full dynamics, up to numerical precision. On the flip side, we might have to perform many simulations to explore the full parameter space, and need to mind the restrictions of the method, such as finite size effects. These can easily skew the results, if the simulations are not executed carefully. To calculate the spectrum, for example, we should run separate simulations for each driving frequency. Each of these simulations needs to be long enough for the transients to sufficiently decay. Note that while it is possible to extract the full spectrum from a single simulation by applying a delta- or step-like excitation and decomposing the resulting response, this method again relies on a linear approximation.

In order to keep things as simple as possible, we will not consider complications like cubic anisotropy. We do have to consider dipolar interaction, however, as this significantly changes the character of the conical excitations. Without it, the two modes are degenerate, and their magnetic field dependence is universal, while with dipolar interaction, the modes are split and depend on the shape and material of the sample, see [figure 4.1c](#) and [52, 86]. For concreteness, we will set up our simulations to match a cube of Cu_2OSeO_3 . Since we expect the system to keep its effectively one-dimensional nature, we use a 1D simulation cell with macrogeometry PBCs for that purpose. The length, of course, has to be commensurate with the conical period. The number of wavelengths that fit into the simulation will be of interest later on. For now, a single winding with PBCs is sufficient.

In a first step, we will do as described above, and calculate the spectrum from a series of simulations with varying driving frequency. We set up a conical state in a background magnetic field of $\mathbf{B}_0 = 84 \text{ mT } \hat{\mathbf{e}}_z \parallel \mathbf{q}$, minimizing the energy to reach the equilibrium state. We then drive the system with an oscillating magnetic field $\mathbf{B}_{\omega_0}(t) = B_{\omega_0} \sin(\omega_0 t) \hat{\mathbf{e}}_x \perp \mathbf{q}$, $B_{\omega_0} = 0.25 \text{ mT}$, which couples strongly to the $\pm Q$ modes [86]. Among other things, we record the mean normalized magnetic moment $\mathbf{m}_{\text{mean}} = \sum_i \hat{\mathbf{m}}_i / |L_{\text{dc}}| = \langle \hat{\mathbf{M}} \rangle$ during the simulation. Here, $|L_{\text{dc}}|$ is the cardinality of the discretization lattice, i. e. the number of discretization cells. Since, in equilibrium, we have $\mathbf{m}_{\text{mean}} \parallel \mathbf{q} \parallel \hat{\mathbf{e}}_z$, the amplitude of the oscillating perpendicular component $m_{\text{mean},x}$ is a good measure of the response of the system to the excitation. Plotting this as a function of the driving frequency ω_0 , as done in [figure 4.2](#), we get the conical spectrum at $\mathbf{k} = 0$, including non-linear effects. The result nicely shows

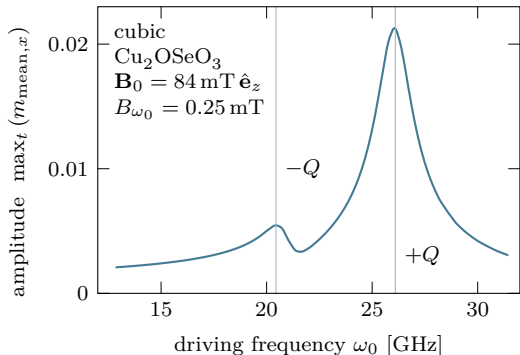


Figure 4.2: Conical spectrum from micromagnetic simulations. The amplitude of the mean normalized magnetic moment is a good measure of the response of the conical state to the oscillating magnetic field. As a function of driving frequency, it shows a clear two-peak structure. The peak positions are in excellent agreement with linear spin wave theory (vertical lines).

two peaks, broadened by damping, corresponding to the $\pm Q$ modes. The peak positions are in excellent agreement with the results from linear response theory, shown as vertical lines.

When taking a closer look at the magnetization dynamics, however, we notice a marked difference to the dynamics described above and illustrated in figure 4.1. Each individual spin no longer moves in a simple precession. Instead, their motion is reminiscent of a classical spinning top, with a combination of precession and nutation. This is because, due to the non-linearity, spins do not return to their original position after one oscillation. These shifts accumulate, resulting in a rotation around \mathbf{q} . Note that in linear response theory, it would be impossible to obtain such a result from a simple oscillatory excitation. An excitation with a single frequency would result in a response with the same single frequency. Using micromagnetic simulations with the same single-frequency excitation, we obtain a response characterized by two frequencies, one for the precession and one for the nutation. Figure 4.3 shows the path of one of the spins for the full motion in panel (c). Panels (a) and (b) show the path decomposed into pure precession and pure rotation around \mathbf{q} . The path of the combined motion is also akin to a so-called prolate spherical trochoid — a generalized cycloid on the surface of a sphere. This is, however, not an exact classification, because the ellipticity of the precession of each spin changes over the course of the larger rotation, as a consequence of the changing alignment with the oscillating magnetic field. Regarding the collective motion, the spin compression waves are still in evidence. Additionally, however, the whole state rotates continuously around \mathbf{q} , reminiscent of an Archimedean screw. Due to the screw symmetry of the underlying conical state, this rotation can also be understood as a translation of the spin structure. This in turn can be understood in the context of a perturbative theory based on linear spin wave theory. The linear motion of the conical state can be seen as an activation of its translational Goldstone mode, due to interactions with the $\pm Q$ modes of linear spin wave theory.

To quantify this new screw motion of the conical excitation modes, we need to determine the corresponding angular frequency ω_{screw} from our simulations. While conceptually this is rather trivial, doing so algorithmically is more difficult than one might expect. This is due to a combination of the near periodicity of the state and its overlain oscillations. Together, these properties make both directly reading off the frequency and determining it with a direct simple fit difficult. We obtain the best results with the following procedure. We record the direction of a single spin as a function of time. To the values of its azimuthal angle ϕ we add multiples of 2π , such that the difference of successive values is minimal. To a good

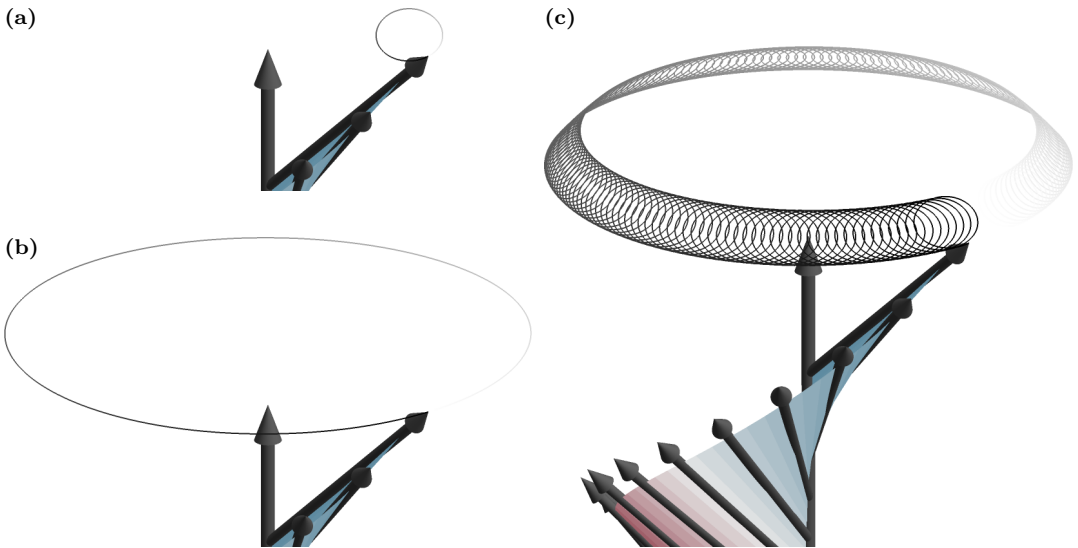


Figure 4.3: Non-linear spin waves in the conical state. In agreement with linear spin wave theory, each individual spin precesses (a) and spin compression waves travel through the system (not shown). Due to the non-linearity, spins don't return to exactly the same direction after one period. Instead, each oscillation rotates all spins by a small angle around \mathbf{q} , which compounds over time (b). Together, the full motion is reminiscent of a classical top with precession and nutation (c). The collective motion combines spin compression waves with an Archimedean screw-like rotation. Shown here is the $+Q$ mode. A figure similar to (c) can be found in [LH7].

approximation, the resulting data consists of a sine wave and a linear slope superimposed, while the raw ϕ might contain jumps of 2π . As long as the oscillations are smaller than the opening angle of the conical state, the linear slope is just ω_{screw} . Thus we can easily determine ω_{screw} by a simple linear fit that averages over many periods of the fast oscillations.

Using this technique, we can determine the dependence of ω_{screw} on the simulation parameters. Figure 4.4 shows ω_{screw} as a function of the driving frequency ω_0 . The first obvious feature is its two-peak structure, corresponding to the resonances of the $\pm Q$ modes, where the two modes feature rotation in opposite directions. It is noteworthy, that the peaks in ω_{screw} do not line up perfectly with the $\pm Q$ modes from linear response theory. This stands in contrast to the peaks in the oscillation amplitude shown in figure 4.2 that do align, even though both figures are drawn from the same data set. So the fastest screw motion is not necessarily achieved with the strongest oscillations in the magnetization. Interestingly, when interpreting the screw motion as a translation, the corresponding velocity is antiparallel to \mathbf{q} for the $+Q$ mode and parallel for the $-Q$ mode — against the direction of the spin compression waves.

For comparison, figure 4.4 also shows analytical results, obtained by solving the LLG equation (1.8) including contributions up to second order in the driving field [LH7]. The two curves show very good but not perfect agreement. There are two obvious possible reasons for this discrepancy. First, it might simply be corrections due to contributions of even higher order in the driving field, that were not considered in the analytical calculation. Second, it might be numerical inaccuracy. In particular, almost perfect agreement can be reached by

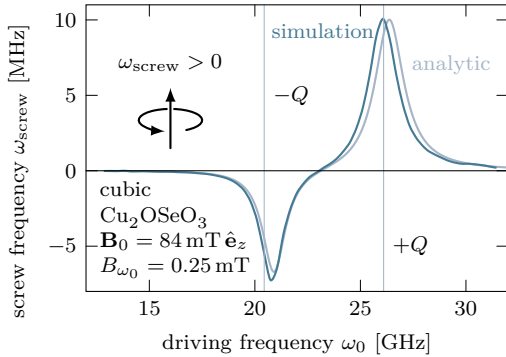


Figure 4.4: Driving frequency dependence of the screw frequency ω_{screw} . Determined from micromagnetic simulations as described in the main text (dark blue). Results fit well with analytical results from solving the LLG to second order in B_{ω_0} [LH7] (light blue). The $\pm Q$ modes (locations marked by vertical lines) have opposite sense of rotation, as defined by the inset. A similar figure can be found in [LH7].

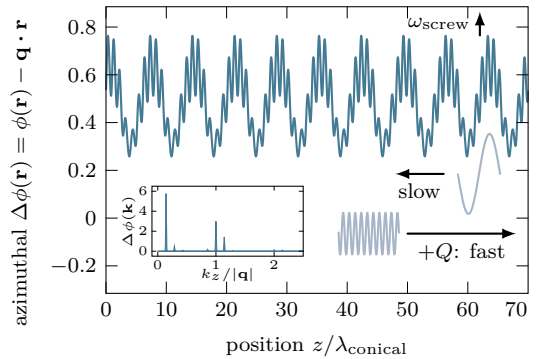
assuming that the simulations were done for a not quite cubic sample with demagnetization factors differing by up to about $\sim 7\%$ from the analytical value for a cube of $\frac{1}{3}$. Although 7% is a rather large deviation to be explained by numerical inaccuracy, we observe that there is at least *some* inaccuracy in this part of the simulations.

Concerning other parameters, we find that ω_{screw} is approximately proportional to the square of the amplitude of the driving magnetic field. This is in agreement with the analytical results, where the first contribution also appears at second order [LH7]. It implicitly shows that this effect is impossible to be obtained from a linear spin wave calculation, which only accounts for terms linear in the oscillating field. We also find that without dipolar interaction, the screw frequency is somewhat reduced, which makes sense considering that the $\pm Q$ modes show opposite signs of ω_{screw} , and that without dipolar interaction they become degenerate.

It is also possible to go one step further, and perform a linear spin wave calculation by expanding around this rotating steady state. Using Floquet theory, it is possible to show that at some critical value of the oscillating magnetic field, one of the resulting excitation modes becomes unstable [LH7]. This is in agreement with our simulations. When the amplitude of the driving field becomes of the order of 1 mT ,¹ and the chosen simulation volume is large enough, we see a marked change in the dynamics of the system. To visualize the effect, we plot the difference in the azimuthal angle between the driven and undriven state $\Delta\phi(\mathbf{r}) = \phi(\mathbf{r}) - \mathbf{q} \cdot \mathbf{r}$. For weak driving, this is a simple sine-wave, due to the spin compression waves traveling through the system. Above the critical driving, its structure is much more complicated, as shown in figure 4.5. There, $\Delta\phi$ shows evidence for the population of two interacting spin waves. Beyond the spin compression waves of the $+Q$ mode with wavelength equal to $\lambda_{\text{conical}} = \frac{2\pi}{|\mathbf{q}|}$, and traveling to the right of the figure, it clearly shows modulation on a longer scale, which propagates in the opposite direction. Apparently, these two spin waves interact, which is visible in the modulation of the amplitude of the $+Q$ mode, and in the Fourier transform, shown in the bottom left inset. Note that, due to quasi PBCs, in order for the new mode to be able to proliferate, without the system becoming chaotic, it is important that its wavelength is commensurate with the system size. Correspondingly, we see modes with different wavelength appearing, when changing the system size, with typical values between $\lambda_{\text{conical}}/8$ and $\lambda_{\text{conical}}/7$. It is interesting to note that neither this wavelength, nor the corresponding frequency of $\omega \approx 0.8 \text{ GHz}$ for the parameters of figure 4.5, appear to be directly connected to any previously present length respectively time scale. This highlights the spontaneous emergence of these new length and time scales.

58 ¹Note that the actual critical value depends on many factors, including damping and sample shape, and may vary significantly.

Figure 4.5: Azimuthal angle difference showing the population of a second spin wave mode. The modulation of $\Delta\phi(\mathbf{r})$, as well as its Fourier transform (bottom left inset), show a second spin wave mode appearing with $\lambda = \lambda_{\text{conical}}/7$. It propagates much more slowly ($\omega \approx 0.8$ GHz) than the resonantly driven $+Q$ mode ($\lambda = \lambda_{\text{conical}}$, $\omega \approx 26$ GHz), and in the opposite direction. The whole graph rises with speed ω_{screw} . Parameters as in figure 4.4, except $B_{\omega_0} = 0.75$ mT and $\omega_0 \approx 26$ GHz.



We have shown that the physics of helimagnons is even richer than previously known. A nominally weak effect, appearing to second order in the weak external drive, fundamentally changes the character of the excitation modes of the conical state for any strength of driving. This highlights that while linear spin wave theory gives approximately correct results, it only strictly does so for short times, as even small deviations may easily compound, when the system has a Goldstone mode.

The analogy with an Archimedean screw raises the question whether the translational motion of the conical state might drive other processes. Natural candidates would be driving a charge, spin, or heat current. Indeed, early calculations suggest that in a metallic system, these modes should drive an electric current [LH7]. It is also interesting to speculate whether it might be possible to construct an efficient magnon laser based on the spin wave mode becoming unstable for strong driving. This might make the conical phase very interesting for applications in spintronic devices.

We have examined various aspects of the equilibrium and non-equilibrium properties of chiral magnets. In [chapter 2](#), we have explored the influence of cubic crystal anisotropy on their phase diagram. We extended the well-known Ginzburg–Landau model of chiral magnets to take various anisotropic energy contributions into account. Using extensive numerical minimization, we found that any of these contributions can stabilize a helical phase and a skyrmion lattice phase, beyond the conical and polarized phases that also exist without anisotropy. For most types of cubic anisotropy, it remains to be explored whether the skyrmion lattice phases we found are connected to the fluctuation-stabilized skyrmion phase pocket close to T_c . However, for one type of anisotropy in particular, namely the $(M_x^4 + \dots)$ term, we have argued that this is not the case. Using this term, we also found interesting metastable helical and tilted conical states. These last results fit very nicely with experiments on Cu_2OSeO_3 , where both a skyrmion lattice in a second disconnected area and a tilted phase with an unexpected \mathbf{q} -direction were found. The former most likely poses the ground state, while the latter probably only exists metastably. While the experiments did not find a metastable helical state, we have argued that its existence might be crucial for the appearance of the skyrmion lattice. We have also characterized the occurring phases. In the case of the helical phase with $\mathbf{q} \parallel \langle 111 \rangle$, we found that the reorientation towards the magnetic field $\mathbf{B} \parallel \langle 001 \rangle$ starts very slowly, but becomes much quicker when approaching the transition to the conical phase. For the skyrmion lattice, we found that there are multiple competing lattice structures. In wide areas of the phase diagram the energies of these are within the range of numerical accuracy of each other. In the case of the metastable tilted conical states, we found an intriguing real-space structure for some parameters, involving single conical windings separated by polarized areas. These last two aspects would be very interesting to explore in more detail, particularly with a focus on the spin wave spectrum of these phases. The skyrmion lattice has been shown to be strongly disordered, which is likely a consequence of the small energy difference between the different lattice structures. Such a disordered state will no doubt have a rather different excitation spectrum than the perfectly ordered lattice. In the tilted state, on the other hand, the almost isolated windings can move much more freely. Consequently, the corresponding spin wave mode should become much softer. Finally, it might also be worthwhile to extend our survey of phase diagrams of anisotropic chiral magnets by using magnetic fields with different orientations. While, at first glance, it might appear there is not much difference to a setup with, say $\mathbf{B} \parallel \langle 111 \rangle$, the two situations actually have different symmetries, which should have consequences for the phase diagram.

In [chapter 3](#), we discussed two studies involving defects in skyrmion lattices. For the first of these, we explored the mechanism with which skyrmion lattices rotate when subjected to a radial heat current. We found that this rotation is realized by plastic deformations constantly occurring throughout the skyrmion lattice. As in atomic lattices, this is best described by the movement of lattice defects. These defects were found to arrange into grain boundaries separating skyrmion lattice grains with different orientation. We observed the rich dynamics resulting from the constant formation and destruction of these boundaries. To deepen our understanding of the dynamics, and to better put it into context, a natural next step would be to obtain an equation of motion for the defects. A particularly important aspect would be the question whether or not it differs from that of defects in atomic lattices.

In [section 3.3](#), we set out to develop a theoretical description of the experimentally observed two-step melting process of a skyrmion lattice. We approached this based on the KTHNY

theory of two-dimensional melting. Using micromagnetic simulations at $T = 0$ to determine Young's modulus Y yielded, unfortunately, a result almost two orders of magnitude larger than the critical value expected from KTHNY theory. We also calculated an effective skyrmion–skyrmion interaction potential from the same type of simulation. In increasing magnetic fields, the resulting potential becomes very flat, which qualitatively agrees with the experiment. A possible refinement of our approach would be to include cubic anisotropy into the simulations. Since we have shown that these drive the skyrmion lattice close to a structural transition, they will most likely have a strong impact on the elastic properties of the lattice, including Young's modulus.

Finally, in [chapter 4](#), we discussed excitations of the conical phase of chiral magnets. Previous theoretical descriptions of such spin waves were based on linear response theory. Using micromagnetic simulations we have discovered a very interesting non-linear effect. The collective motion of the known magnon modes involves a previously unknown Archimedean screw-like rotation. Furthermore, we have seen the macroscopic activation of a second mode, hinting at possible new applications. The question whether the Archimedean screw-like rotation may drive an electric current is already being investigated.

- [LH1] S. Pöllath, J. Wild, L. Heinen, T. N. G. Meier, M. Kronseder, L. Tutsch, A. Bauer, H. Berger, C. Pfleiderer, J. Zweck, A. Rosch, and C. H. Back, “Dynamical Defects in Rotating Magnetic Skyrmion Lattices”, *Phys. Rev. Lett.* **118**, 207205 (2017).  
- [LH2] A. Chacon, L. Heinen, M. Halder, A. Bauer, W. Simeth, S. Mühlbauer, H. Berger, M. Garst, A. Rosch, and C. Pfleiderer, “Observation of two independent skyrmion phases in a chiral magnetic material”, *Nat. Phys.* **14**, 936 (2018). 
- [LH3] M. Halder, A. Chacon, A. Bauer, W. Simeth, S. Mühlbauer, H. Berger, L. Heinen, M. Garst, A. Rosch, and C. Pfleiderer, “Thermodynamic evidence of a second skyrmion lattice phase and tilted conical phase in Cu_2OSeO_3 ”, *Phys. Rev. B* **98**, 144429 (2018). 
- [LH4] S. Zhang, G. van der Laan, J. Müller, L. Heinen, M. Garst, A. Bauer, H. Berger, C. Pfleiderer, and T. Hesjedal, “Reciprocal space tomography of 3D skyrmion lattice order in a chiral magnet”, *PNAS* **115**, 6386 (2018). 
- [LH5] P. Huang, T. Schönenberger, M. Cantoni, L. Heinen, A. Magrez, A. Rosch, F. Carbone, and H. M. Rønnow, “Melting of a skyrmion lattice to a skyrmion liquid via a hexatic phase”, *Nat. Nanotechnol.* **15**, 761 (2020). 
- [LH6] T. Bömerich, L. Heinen, and A. Rosch, “Skyrmion and tetarton lattices in twisted bilayer graphene”, *Phys. Rev. B* **102**, 100408 (2020).  
- [LH7] N. del Ser, L. Heinen, and A. Rosch, “Archimedean screw in driven chiral magnets”, *SciPost Phys.* **11**, 9 (2021).  
- [1] I. E. Dzyaloshinskii, “Theory of Helicoidal Structures in Antiferromagnets. I. Non-metals”, *J. Exp. Theor. Phys.* **19**, 960 (1964). 
- [2] P. Bak and M. H. Jensen, “Theory of helical magnetic structures and phase transitions in MnSi and FeGe”, *J. Phys. C: Solid State* **13**, L881 (1980). 
- [3] O. Nakanishi, A. Yanase, A. Hasegawa, and M. Kataoka, “The origin of the helical spin density wave in MnSi”, *Solid State Commun.* **35**, 995 (1980). 
- [4] H. Effenberger and F. Pertlik, “Die Kristallstrukturen der Kupfer(II)-oxo-selenite $\text{Cu}_2\text{O}(\text{SeO}_3)$ (kubisch und monoklin) und $\text{Cu}_4\text{O}(\text{SeO}_3)_3$ (monoklin und triklin)”, *Monatsh. Chem.* **117**, 887 (1986). 
- [5] A. Yoshimori, “A New Type of Antiferromagnetic Structure in the Rutile Type Crystal”, *J. Phys. Soc. Jpn.* **14**, 807 (1959). 
- [6] P. Schoenherr, J. Müller, L. Köhler, A. Rosch, N. Kanazawa, Y. Tokura, M. Garst, and D. Meier, “Topological domain walls in helimagnets”, *Nat. Phys.* **14**, 465 (2018).  
- [7] S. Mühlbauer, B. Binz, F. Jonietz, C. Pfleiderer, A. Rosch, A. Neubauer, R. Georgii, and P. Boni, “Skyrmion Lattice in a Chiral Magnet”, *Science* **323**, 915 (2009).  

- [8] Y. Tokunaga, X. Z. Yu, J. S. White, H. M. Rønnow, D. Morikawa, Y. Taguchi, and Y. Tokura, “A new class of chiral materials hosting magnetic skyrmions beyond room temperature”, *Nat. Commun.* **6**, 7638 (2015).  
- [9] I. Kézsmárki, S. Bordács, P. Milde, E. Neuber, L. M. Eng, J. S. White, H. M. Rønnow, C. D. Dewhurst, M. Mochizuki, K. Yanai, H. Nakamura, D. Ehlers, V. Tsurkan, and A. Loidl, “Néel-type skyrmion lattice with confined orientation in the polar magnetic semiconductor GaV4S8”, *Nat. Mat.* **14**, 1116 (2015).  
- [10] S. Bordács, A. Butykai, B. G. Szigeti, J. S. White, R. Cubitt, A. O. Leonov, S. Widmann, D. Ehlers, H.-A. K. von Nidda, V. Tsurkan, A. Loidl, and I. Kézsmárki, “Equilibrium Skyrmion Lattice Ground State in a Polar Easy-plane Magnet”, *Sci. Rep.* **7**, 7584 (2017). 
- [11] S. Heinze, K. von Bergmann, M. Menzel, J. Brede, A. Kubetzka, R. Wiesendanger, G. Bihlmayer, and S. Blügel, “Spontaneous atomic-scale magnetic skyrmion lattice in two dimensions”, *Nat. Phys.* **7**, 713 (2011). 
- [12] C. Moreau-Luchaire, C. Moutafis, N. Reyren, J. Sampaio, C. A. F. Vaz, N. Van Horne, K. Bouzehouane, K. Garcia, C. Deranlot, P. Warnicke, P. Wohlhüter, J.-M. George, M. Weigand, J. Raabe, V. Cros, and A. Fert, “Additive interfacial chiral interaction in multilayers for stabilization of small individual skyrmions at room temperature”, *Nat. Nanotechnol.* **11**, 444 (2016).  
- [13] K. Everschor-Sitte, J. Masell, R. M. Reeve, and M. Kläui, “Perspective: Magnetic skyrmions — Overview of recent progress in an active research field”, *J. Appl. Phys.* **124**, 240901 (2018). 
- [14] T. H. R. Skyrme and B. F. J. Schonland, “A non-linear field theory”, *Proc. R. Soc. Lon. Ser. A* **260**, 127 (1961). 
- [15] C. Schütte, “Skyrmions and Monopoles in Chiral Magnets & Correlated Heterostructures”, Ph.D. thesis, University of Cologne, Cologne, 2014. 
- [16] J. Müller, “Magnetic Skyrmions and Topological Domain Walls”, Ph.D. thesis, University of Cologne, Cologne, 2018. 
- [17] F. N. Rybakov, A. B. Borisov, S. Blügel, and N. S. Kiselev, “New Type of Stable Particlelike States in Chiral Magnets”, *Phys. Rev. Lett.* **115**, 117201 (2015).  
- [18] F. N. Rybakov, A. B. Borisov, S. Blügel, and N. S. Kiselev, “New spiral state and skyrmion lattice in 3D model of chiral magnets”, *New J. Phys.* **18**, 045002 (2016). 
- [19] P. Milde, D. Köhler, J. Seidel, L. M. Eng, A. Bauer, A. Chacon, J. Kindervater, S. Mühlbauer, C. Pfleiderer, S. Buhrandt, C. Schütte, and A. Rosch, “Unwinding of a Skyrmion Lattice by Magnetic Monopoles”, *Science* **340**, 1076 (2013). 
- [20] H. Oike, A. Kikkawa, N. Kanazawa, Y. Taguchi, M. Kawasaki, Y. Tokura, and F. Kagawa, “Interplay between topological and thermodynamic stability in a metastable magnetic skyrmion lattice”, *Nat. Phys.* **12**, 62 (2016).  

- [21] J. Wild, T. N. G. Meier, S. Pöllath, M. Kronseder, A. Bauer, A. Chacon, M. Halder, M. Schowalter, A. Rosenauer, J. Zweck, J. Müller, A. Rosch, C. Pfeiderer, and C. H. Back, “Entropy-limited topological protection of skyrmions”, *Sci. Adv.* **3**, e1701704 (2017).  
- [22] W. Wang, M. Beg, B. Zhang, W. Kuch, and H. Fangohr, “Driving magnetic skyrmions with microwave fields”, *Phys. Rev. B* **92**, 020403 (2015).  
- [23] M. Mochizuki, X. Z. Yu, S. Seki, N. Kanazawa, W. Koshibae, J. Zang, M. Mostovoy, Y. Tokura, and N. Nagaosa, “Thermally driven ratchet motion of a skyrmion microcrystal and topological magnon Hall effect”, *Nat. Mat.* **13**, 241 (2014).  
- [24] F. Jonietz, S. Mühlbauer, C. Pfeiderer, A. Neubauer, W. Münzer, A. Bauer, T. Adams, R. Georgii, P. Böni, R. A. Duine, K. Everschor, M. Garst, and A. Rosch, “Spin Transfer Torques in MnSi at Ultralow Current Densities”, *Science* **330**, 1648 (2010).  
- [25] T. Schulz, R. Ritz, A. Bauer, M. Halder, M. Wagner, C. Franz, C. Pfeiderer, K. Everschor, M. Garst, and A. Rosch, “Emergent electrodynamics of skyrmions in a chiral magnet”, *Nat. Phys.* **8**, 301 (2012).  
- [26] A. Fert, V. Cros, and J. Sampaio, “Skyrmions on the track”, *Nat. Nanotechnol.* **8**, 152 (2013). 
- [27] R. Tomasello, E. Martinez, R. Zivieri, L. Torres, M. Carpentieri, and G. Finocchio, “A strategy for the design of skyrmion racetrack memories”, *Sci. Rep.* **4**, 6784 (2014).  
- [28] X. Zhang, M. Ezawa, and Y. Zhou, “Magnetic skyrmion logic gates: conversion, duplication and merging of skyrmions”, *Sci. Rep.* **5**, 9400 (2015).  
- [29] J. Müller, “Magnetic skyrmions on a two-lane racetrack”, *New J. Phys.* **19**, 025002 (2017).  
- [30] D. Pinna, G. Bourianoff, and K. Everschor-Sitte, “Reservoir Computing with Random Skyrmion Textures”, *Phys. Rev. Appl.* **14**, 054020 (2020).  
- [31] G. Finocchio, M. Di Ventra, K. Y. Camsari, K. Everschor-Sitte, P. Khalili Amiri, and Z. Zeng, “The promise of spintronics for unconventional computing”, *Journal of Magnetism and Magnetic Materials* **521**, 167506 (2021).  
- [32] N. Nagaosa and Y. Tokura, “Topological properties and dynamics of magnetic skyrmions”, *Nat. Nanotechnol.* **8**, 899 (2013). 
- [33] A. Fert, N. Reyren, and V. Cros, “Magnetic skyrmions: advances in physics and potential applications”, *Nat. Rev. Mat.* **2**, 17031 (2017).  
- [34] *Topological Structures in Ferromagnetic Materials: Domain Walls, Vortices and Skyrmions*, Vol. 228 of *Springer Series in Materials Science*, edited by J. Seidel (Springer, Cham, 2016). 
- [35] F. Bloch, “Nuclear Induction”, *Phys. Rev.* **70**, 460 (1946). 

- [36] T. L. Gilbert, “A Lagrangian formulation of gyromagnetic equation of the magnetization field”, *Phys. Rev.* **100**, 1243 (1955), [Abstract only; full report: “Armor Research Foundation Project No. A059, Supplementary Report, May 1, 1956” (unpublished)—summarized by Gilbert in 2004 [37]].
- [37] T. L. Gilbert, “A phenomenological theory of damping in ferromagnetic materials”, *IEEE Trans. Mag.* **40**, 3443 (2004). 
- [38] L. Landau and E. Lifshitz, “On the Theory of the Dispersion of Magnetic Permeability in Ferromagnetic Bodies”, *Phys. Z. Sowjet.* **8**, 153 (1935).  
- [39] A. Vansteenkiste, J. Leliaert, M. Dvornik, M. Helsen, F. Garcia-Sanchez, and B. Van Waeyenberge, “The design and verification of Mumax3”, *AIP Adv.* **4**, 107133 (2014).  
- [40] M. J. Donahue and D. G. Porter, “OOMMF User’s Guide, Version 1.0”, *Interagency Report NISTIR 6376*, National Institute of Standards and Technology, Gaithersburg, MD (1999).  
- [41] R. Takashima, H. Ishizuka, and L. Balents, “Quantum skyrmions in two-dimensional chiral magnets”, *Phys. Rev. B* **94**, 134415 (2016).  
- [42] C. Psaroudaki, S. Hoffman, J. Klinovaja, and D. Loss, “Quantum Dynamics of Skyrmions in Chiral Magnets”, *Phys. Rev. X* **7**, 041045 (2017).  
- [43] W. F. Brown, Jr., *Magnetostatic Principles in Ferromagnetism, Selected topics in solid state physics* (North-Holland Pub. Co., Amsterdam, 1962).
- [44] A. J. Newell, W. Williams, and D. J. Dunlop, “A generalization of the demagnetizing tensor for nonuniform magnetization”, *J. Geophys. Res. Sol. Ea.* **98**, 9551 (1993). 
- [45] K. Ramstöck, T. Leibl, and A. Hubert, “Optimizing stray field computations in finite-element micromagnetics”, *J. Magn. Magn. Mater.* **135**, 97 (1994). 
- [46] M. Schabes and A. Aharoni, “Magnetostatic interaction fields for a three-dimensional array of ferromagnetic cubes”, *IEEE Trans. Mag.* **23**, 3882 (1987). 
- [47] A. Aharoni, “Demagnetizing factors for rectangular ferromagnetic prisms”, *J. Appl. Phys.* **83**, 3432 (1998). 
- [48] E. C. Stoner, “The demagnetizing factors for ellipsoids”, *Lond. Edinb. Dubl. Phil. Mag.* **36**, 803 (1945). 
- [49] D. Chernyshenko and H. Fangohr, “Computing the demagnetizing tensor for finite difference micromagnetic simulations via numerical integration”, *J. Magn. Magn. Mater.* **381**, 440 (2015).  
- [50] K. M. Lebecki, M. J. Donahue, and M. W. Gutowski, “Periodic boundary conditions for demagnetization interactions in micromagnetic simulations”, *J. Phys. D: Appl. Phys.* **41**, 175005 (2008). 

- [51] H. Fangohr, G. Bordignon, M. Franchin, A. Knittel, P. A. J. de Groot, and T. Fischbacher, “A new approach to (quasi) periodic boundary conditions in micromagnetics: The macrogeometry”, *J. Appl. Phys.* **105**, 07D529 (2009). 
- [52] T. Schwarze, J. Waizner, M. Garst, A. Bauer, I. Stasinopoulos, H. Berger, C. Pfeleiderer, and D. Grundler, “Universal helimagnon and skyrmion excitations in metallic, semiconducting and insulating chiral magnets”, *Nat. Mat.* **14**, 478 (2015). 
- [53] M. N. Wilson, A. B. Butenko, A. N. Bogdanov, and T. L. Monchesky, “Chiral skyrmions in cubic helimagnet films: The role of uniaxial anisotropy”, *Phys. Rev. B* **89**, 094411 (2014).  
- [54] T. Adams, A. Chacon, M. Wagner, A. Bauer, G. Brandl, B. Pedersen, H. Berger, P. Lemmens, and C. Pfeleiderer, “Long-Wavelength Helimagnetic Order and Skyrmion Lattice Phase in Cu_2OSeO_3 ”, *Phys. Rev. Lett.* **108**, 237204 (2012).  
- [55] A. Neubauer, C. Pfeleiderer, B. Binz, A. Rosch, R. Ritz, P. G. Niklowitz, and P. Böni, “Topological Hall Effect in the *A* Phase of MnSi”, *Phys. Rev. Lett.* **102**, 186602 (2009).  
- [56] I. I. Lobanova, V. V. Glushkov, N. E. Sluchanko, and S. V. Demishev, “Macroscopic evidence for Abrikosov-type magnetic vortexes in MnSi *A*-phase”, *Sci. Rep.* **6**, 22101 (2016).  
- [57] F. Qian, H. Wilhelm, A. Aqeel, T. T. M. Palstra, A. J. E. Lefering, E. H. Brück, and C. Pappas, “Phase diagram and magnetic relaxation phenomena in Cu_2OSeO_3 ”, *Phys. Rev. B* **94**, 064418 (2016).  
- [58] F. Qian, L. J. Bannenberg, H. Wilhelm, G. Chaboussant, L. M. Debeer-Schmitt, M. P. Schmidt, A. Aqeel, T. T. M. Palstra, E. Brück, A. J. E. Lefering, C. Pappas, M. Mostovoy, and A. O. Leonov, “New magnetic phase of the chiral skyrmion material Cu_2OSeO_3 ”, *Sci. Adv.* **4**, eaat7323 (2018).  
- [59] A. Bauer, A. Chacon, M. Wagner, M. Halder, R. Georgii, A. Rosch, C. Pfeleiderer, and M. Garst, “Symmetry breaking, slow relaxation dynamics, and topological defects at the field-induced helix reorientation in MnSi”, *Phys. Rev. B* **95**, 024429 (2017). 
- [60] W. Bollmann, *Crystal Defects and Crystalline Interfaces* (Springer, Berlin [u.a.], 1970).
- [61] C. Schütte and M. Garst, “Magnon-skyrmion scattering in chiral magnets”, *Phys. Rev. B* **90**, 094423 (2014).  
- [62] S.-Z. Lin, C. Reichhardt, C. D. Batista, and A. Saxena, “Particle model for skyrmions in metallic chiral magnets: Dynamics, pinning, and creep”, *Phys. Rev. B* **87**, 214419 (2013).  
- [63] C. Reichhardt and C. J. O. Reichhardt, “Noise fluctuations and drive dependence of the skyrmion Hall effect in disordered systems”, *New J. Phys.* **18**, 095005 (2016).  

- [64] J. Müller and A. Rosch, “Capturing of a magnetic skyrmion with a hole”, *Phys. Rev. B* **91**, 054410 (2015).  
- [65] A. A. Thiele, “Steady-State Motion of Magnetic Domains”, *Phys. Rev. Lett.* **30**, 230 (1973). 
- [66] S. Schroeter and M. Garst, “Scattering of high-energy magnons off a magnetic skyrmion”, *Low Temperature Physics* **41**, 817 (2015).  
- [67] L. Kong and J. Zang, “Dynamics of an Insulating Skyrmion under a Temperature Gradient”, *Phys. Rev. Lett.* **111**, 067203 (2013).  
- [68] X. Z. Yu, N. Kanazawa, Y. Onose, K. Kimoto, W. Z. Zhang, S. Ishiwata, Y. Matsui, and Y. Tokura, “Near room-temperature formation of a skyrmion crystal in thin-films of the helimagnet FeGe”, *Nat. Mat.* **10**, 106 (2011). 
- [69] Y. Nishikawa, K. Hukushima, and W. Krauth, “Solid-liquid transition of skyrmions in a two-dimensional chiral magnet”, *Phys. Rev. B* **99**, 064435 (2019).  
- [70] R. E. Peierls, “Bemerkungen über Umwandlungstemperaturen”, *Helv. Phys. Acta* **7**, 81 (1934). 
- [71] L. Landau, “On the theory of phase transitions”, *Phys. Z. Sowjet.* **11**, 26 (1937).  
- [72] N. D. Mermin and H. Wagner, “Absence of Ferromagnetism or Antiferromagnetism in One- or Two-Dimensional Isotropic Heisenberg Models”, *Phys. Rev. Lett.* **17**, 1133 (1966). 
- [73] J. M. Kosterlitz and D. J. Thouless, “Ordering, metastability and phase transitions in two-dimensional systems”, *J. Phys. C: Solid State* **6**, 1181 (1973). 
- [74] A. P. Young, “Melting and the vector Coulomb gas in two dimensions”, *Phys. Rev. B* **19**, 1855 (1979). 
- [75] D. R. Nelson and B. I. Halperin, “Dislocation-mediated melting in two dimensions”, *Phys. Rev. B* **19**, 2457 (1979). 
- [76] H. Kleinert, “Lattice defect model with two successive melting transitions”, *Phys. Lett. A* **130**, 443 (1988). 
- [77] U. Gasser, C. Eisenmann, G. Maret, and P. Keim, “Melting of Crystals in Two Dimensions”, *ChemPhysChem* **11**, 963 (2010). 
- [78] L. Landau, E. Lifshitz, A. Kosevich, J. Sykes, L. Pitaevskii, and W. Reid, *Theory of Elasticity*, Vol. 7 of *Course of theoretical physics* (Butterworth-Heinemann, Oxford, 1986). 
- [79] J. Zanghellini, P. Keim, and H. H. von Grünberg, “The softening of two-dimensional colloidal crystals”, *J. Phys. Condens. Matter* **17**, S3579 (2005). 

-
- [80] L. Exl, S. Bance, F. Reichel, T. Schrefl, H. P. Stimming, and N. J. Mauser, “LaBonte’s method revisited: An effective steepest descent method for micromagnetic energy minimization”, *J. Appl. Phys.* **115**, 17D118 (2014).  
- [81] G. Castellano, “Thermodynamic potentials for simple magnetic systems”, *J. Magn. Mater.* **260**, 146 (2003). 
- [82] S. P. Kang, H. Y. Kwon, and C. Won, “Elastic moduli and Poisson’s ratio of 2-dimensional magnetic skyrmion lattice”, *J. Appl. Phys.* **121**, 203902 (2017). 
- [83] M. Kugler, G. Brandl, J. Waizner, M. Janoschek, R. Georgii, A. Bauer, K. Seemann, A. Rosch, C. Pfleiderer, P. Böni, and M. Garst, “Band Structure of Helimagnons in MnSi Resolved by Inelastic Neutron Scattering”, *Phys. Rev. Lett.* **115**, 097203 (2015).  
- [84] I. Stasinopoulos, S. Weichselbaumer, A. Bauer, J. Waizner, H. Berger, M. Garst, C. Pfleiderer, and D. Grundler, “Linearly polarized GHz magnetization dynamics of spin helix modes in the ferrimagnetic insulator Cu₂OSeO₃”, *Sci. Rep.* **7**, 7037 (2017). 
- [85] M. Garst, J. Waizner, and D. Grundler, “Collective spin excitations of helices and magnetic skyrmions: review and perspectives of magnonics in non-centrosymmetric magnets”, *J. Phys. D: Appl. Phys.* **50**, 293002 (2017).  
- [86] J. Waizner, “Spin wave excitations in magnetic helices and skyrmion lattices”, Ph.D. thesis, University of Cologne, Cologne, 2016. 
- [87] C. Kittel, “Interpretation of Anomalous Larmor Frequencies in Ferromagnetic Resonance Experiment”, *Phys. Rev.* **71**, 270 (1947). 
- [88] C. Kittel, “On the Theory of Ferromagnetic Resonance Absorption”, *Phys. Rev.* **73**, 155 (1948). 

B20 crystal structure	1
Burgers vector	40, 41, 44
chiral magnet	xi, 1–2, 4, 5, 8, 15, 17, 18, 22, 30–32, 36, 39, 41, 53, 54, 61, 62
copper(II)-oxo-selenite (Cu_2OSeO_3)	xi, 1–3, 15, 17, 18, 20, 24–31, 37, 39, 41, 43, 46–48, 50, 54, 55, 61
demagnetization factor	10, 11, 29, 30
demagnetization kernel (demagnetization tensor field)	10, 11
demagnetization tensor	10–12, 17, 31
dipolar interaction (demagnetization, magnetostatic interaction)	xi, 1, 6, 9–12, 24, 28–31, 53–55, 57
Dzyaloshinskii–Moriya interaction (DMI)	xi, 1, 4, 5, 54
exchange interaction (Heisenberg interaction)	1, 5, 7, 24
helimagnet	2, see also chiral magnet
Kosterlitz–Thouless–Halperin–Nelson–Young (KTHNY) theory	48, 49, 61, 62
Landau–Lifshitz–Gilbert (LLG) equation	6, 7–9, 41, 42, 53–55, 57, 58
Lorentz transmission electron microscopy (LTEM)	41, 46, 47
manganese silicide (MnSi)	2
$P2_13$ space group	1, 16, 18
periodic boundary condition (PBC)	10, 11, 49, 55, 58
renormalization group (RG)	48
small-angle neutron scattering (SANS)	25, 26
skyrmion	xi, 2–5, 20, 25–27, 37, 39, 41, 48–50
Thiele equation	41, 43, 47
winding number	3

DANKSAGUNG

An dieser Stelle möchte ich mich herzlich bei all jenen bedanken, ohne die die letzten Jahre nicht dieselben gewesen wären. Bei allen die das Leben erst lebenswert gemacht haben, und bei allen ohne die ich jetzt nicht an diesem Punkt wäre.

Mein größter Dank gilt meinem Doktorvater Prof. Dr. Achim Rosch, für die großartige Betreuung, und die vielen Stunden voll lehrreicher Diskussionen, während der letzten Jahre. Für seine großzügige Unterstützung, und für seine immer wieder beeindruckende physikalische Einsicht, auf der meine Erfolge fußen.

Auch bei Prof. Dr. Simon Trebst möchte ich mich für die Begutachtung dieser Arbeit bedanken, sowie bei Prof. Dr. Joachim Hemberger für die Übernahme des Prüfungsvorsitzes.

Weiterhin möchte ich mich bei meinen Ko-Autoren bedanken, dafür, dass sie ihre spannenden Ergebnisse mit mir geteilt haben, und so unsere Publikationen, aber auch diese Arbeit möglich gemacht haben. Besonders möchte ich mich bei den zwei Christians, Markus, Alfonso, Marco, Simon, Jan und Thomas bedanken.

Für die vielen hilfreichen Korrekturen möchte ich mich bei Jan Attig und besonders bei Johannes Waizner bedanken, ohne dessen Anmerkungen diese Arbeit nur halb so gut wäre.

Mein Dank gilt auch dem SFB1238, der meine Promotion finanziert hat, mit allen die dazu gehören, sowie Andreas Sindermann und den Mitarbeitern des Rechenzentrums, die die Rechner am laufen halten, trotz allem Unsinn den wir anstellen.

Besonders möchte ich mich auch bei allen Kollegen bedanken, für die angenehme Atmosphäre, und dafür dass im Büro nicht immer nur Arbeit herrschen muss. Besonders hervorheben möchte ich dabei Johannes, Jan, Nina, Vivek, Philipp, Thomas, Dennis, Dennis, Christopher und Jonathan.

Und schließlich — natürlich — meine Familie, ohne deren andauernde Unterstützung und Verständnis diese Arbeit nicht existieren würde.

Ich versichere, dass ich die von mir vorgelegte Dissertation selbständig angefertigt, die benutzten Quellen und Hilfsmittel vollständig angegeben und die Stellen der Arbeit — einschließlich Tabellen, Karten und Abbildungen —, die anderen Werken im Wortlaut oder dem Sinn nach entnommen sind, in jedem Einzelfall als Entlehnung kenntlich gemacht habe; dass diese Dissertation noch keiner anderen Fakultät oder Universität zur Prüfung vorgelegen hat; dass sie — abgesehen von unten angegebenen Teilpublikationen — noch nicht veröffentlicht worden ist, sowie, dass ich eine solche Veröffentlichung vor Abschluss des Promotionsverfahrens nicht vornehmen werde. Die Bestimmungen der Promotionsordnung sind mir bekannt. Die von mir vorgelegte Dissertation ist von Prof. Dr. Achim Rosch betreut worden.

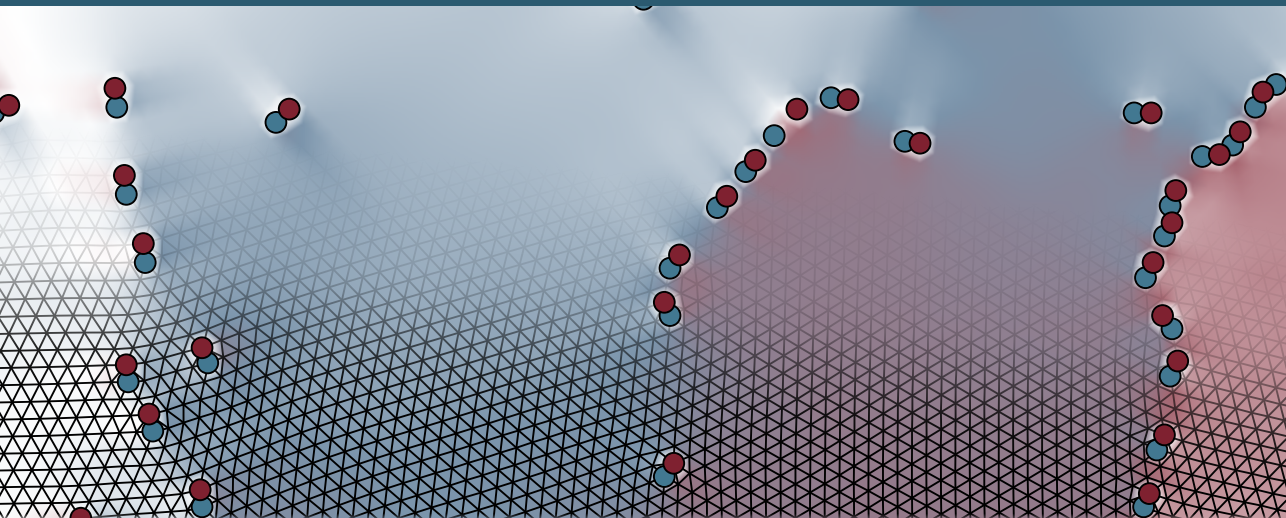
Teilpublikationen:

- S. Pöllath, J. Wild, **L. Heinen**, T. N. G. Meier, M. Kronseder, L. Tutsch, A. Bauer, H. Berger, C. Pfeiderer, J. Zweck, A. Rosch und C. H. Back, „Dynamical Defects in Rotating Magnetic Skyrmion Lattices“, *Physical Review Letters* **118**, 207205 (2017).
- A. Chacon, **L. Heinen**, M. Halder, A. Bauer, W. Simeth, S. Mühlbauer, H. Berger, M. Garst, A. Rosch und C. Pfeiderer, „Observation of two independent skyrmion phases in a chiral magnetic material“, *Nature Physics* **14**, 936–941 (2018).
- M. Halder, A. Chacon, A. Bauer, W. Simeth, S. Mühlbauer, H. Berger, **L. Heinen**, M. Garst, A. Rosch und C. Pfeiderer, „Thermodynamic evidence of a second skyrmion lattice phase and tilted conical phase in Cu_2OSeO_3 “, *Physical Review B* **98**, 144429 (2018).
- S. Zhang, G. van der Laan, J. Müller, **L. Heinen**, M. Garst, A. Bauer, H. Berger, C. Pfeiderer und T. Hesjedal, „Reciprocal space tomography of 3D skyrmion lattice order in a chiral magnet“, *Proceedings of the National Academy of Sciences* **115**, 6386–6391 (2018).
- P. Huang, T. Schönenberger, M. Cantoni, **L. Heinen**, A. Magrez, A. Rosch, F. Carbone und H. M. Rønnow, „Melting of a skyrmion lattice to a skyrmion liquid via a hexatic phase“, *Nature Nanotechnology* **15**, 761 (2020).
- T. Bömerich, **L. Heinen** und A. Rosch, „Skyrmion and tetarton lattices in twisted bilayer graphene“, *Physical Review B* **102**, 100408 (2020).
- N. del Ser, **L. Heinen** und A. Rosch, „Archimedean screw in driven chiral magnets“, *SciPost Physics* **11**, 9 (2021).

21. September 2021

In ordinary ferromagnets, individual magnetic moments tend to align with their neighbors, as long as temperatures are below the critical Curie temperature of the material. Cubic chiral magnets are a class of dominantly ferromagnetic, or rarer ferrimagnetic, materials with a literal twist. Due to broken inversion symmetry, weak spin-orbit coupling can induce a competing Dzyaloshinskii-Moriya interaction, which twists the magnetic texture into helical structures. One of these textures is of special interest to us. In it, the magnetization twist into whirl-like topological structures, called skyrmions.

This thesis explores various aspects of the equilibrium and non-equilibrium properties of chiral magnets, including the impact of cubic anisotropy on the phase diagram, the role of lattice defects in skyrmion lattices, and the dynamics of a strongly driven conical state.



Institute for Theoretical Physics
Faculty of Mathematics and Natural Sciences
University of Cologne

Köln 2021